UNIVERSITY OF TWENTE.
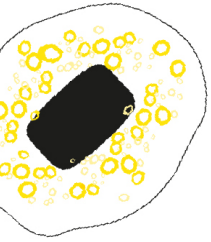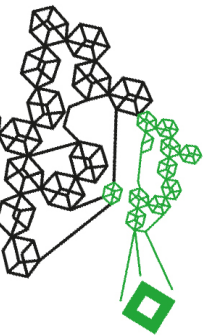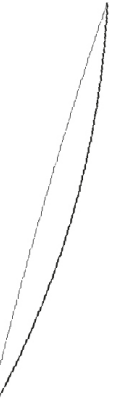
Master thesis

Modelling of laser beam absorption in powder-based sintering processes

Albert Hendrik Nijkamp

20 November 2022

Supervisors:
Dr. T. Weinhart
PhD Candidate J. E. Alvarez Naranjo

Committee:
Prof. Dr. S. Luding
Dr. T. Weinhart
PhD Candidate J. E. Alvarez Naranjo
Prof. Dr. I. Gibson

Modelling of laser beam absorption in powder-based sintering processes

MASTER THESIS

Faculty: Engineering Technology
Programme: Mechanical Engineering
Department: Thermal and Fluid Engineering
Research chair: Multi Scale Mechanics

DATE:

20 November 2022

GRADUATION COMMITTEE:

Chairman: Prof. Dr. S. Luding
Supervisor: Dr. T. Weinhart
Supervisor: PhD Candidate J.E. Alvarez Naranjo
External member: Prof. Dr. I. Gibson

Abstract

In this work, a ray tracing model has been introduced which simulates the light absorption in 2D and 3D particle beds. A finite number of rays, representing a laser beam, propagate into a particle bed, causing the particles to absorb the light and increase in temperature. A simplification has been proposed which replaces these ray tracing simulations, making it a computationally friendly method of computing the absorption while being able to change several variables. These simplifications have been done for a particle doublet and a particle bed in the form of a set of equations, and the use of a semi-random walk was investigated. The equations can subsequently be used in simulations of powder bed sintering.

Contents

List of symbols

Symbol	Description	Unit	Symbol	Description	Unit
$\bar{c}$	Coordinates of any point on the laser centre	m	N_{ray}	Number of rays	-
c_p	Particle specific heat capacity	J/kgK	ov	Particle overlap	m
d	Distance from a particle to the laser centre	m	$\bar{p}$	Coordinates where the ray enters the particle	m
d_s	Distance from a slice to the laser centre	m	P_{in}	Laser power	W
D	Particle diameter	m	$\overline{p_p}$	Coordinates of the centre of the particle	m
E	Absorbed energy out of total incoming energy (relative)	-	r	Incoming ray distance to the particle centre	m
E_{abs}	Absorbed energy out of total incoming energy for the top layer particles (relative)	-	R	Reflected energy portion	-
E_{in}	Incoming energy out of total incoming energy (relative)	-	r_{laser}	Laser spot radius	m
E_p	Absorbed energy out of energy on particle (relative)	-	SF	Scaling factor	-
E_{peak}	Absorbed energy at laser centre (relative)	-	Δt	Time step	s
I	Light energy (relative)	-	ΔT	Temperature change	°C
I_0	Initial light energy (relative)	-	V	Volume	m^3
I_{min}	Energy dissipation threshold (relative)	-	V_m	Square root convention, $V_m = \sqrt{1 - x^m r^2}$	m
I_R	Reflected light energy (relative)	-	x	Refraction index ratio	-
I_T	Transmitted light energy (relative)	-	x_i	Neck radius	m
$\vec{k}$	Incoming ray direction	-	x_i/a_0	Dimensionless neck radius	-
K_{cor}	Correction factor	-	z	Propagation distance	m
$\vec{k}_0$	Initial laser direction	-	Z	Bed height	m
$\vec{k}_R$	Reflected ray direction	-	α	Angle of incidence	°
$\vec{k}_T$	Transmitted ray direction	-	a_0	Particle starting radius	m
Δl	Spatial step size	m	β	Angle of reflection	°
l_{air}	Ray distance between two particles	m	γ	Azimuth angle	°
l_p	Ray distance inside a particle	m	δ_n	Relative overlap	-
l_{start}	Ray distance after hitting first particle	m	θ	Laser angle	°
m	Particle mass	kg	μ	Attenuation coefficient	-
n	Number of trapezoids	-	μ_w	Average of the natural logarithm of l_{air}/D	-
$\vec{n}$	Surface normal direction	-	ρ	Particle density	kg/m^3
n_A	Refraction index medium A (air)	-	σ	Gaussian laser standard deviation, $2\sigma = r_{laser}$	m
n_B	Refraction index medium B (particle)	-	σ_w	Standard deviation of the natural logarithm of l_{air}/D	-
N_{laser}	Number of layers	-	φ	Volume fraction	-

1 Introduction

Selective laser sintering

In additive manufacturing (AM), several methods can be used to solidify multiple layers of a material in a specific shape, to create a 3D structure. One of these methods is selective laser sintering (SLS), where a laser propagates into a powder bed, causing the powder particles to sinter together. As the temperature of the chamber is close to the glass transitional temperature of the material, a relatively small amount of energy is required to reach this temperature and sinter the particles. After one layer is finished, a new, fresh layer of particles is deposited on top of the previous layer. Each new layer will sinter to the previous layer and a consolidated part is created.

However, SLS some known issues such as the existence of residual stresses inside the material and shrinkage or warping of the printed parts. These phenomena can be a result of a too-low chamber temperature, a too-high cooling rate after printing, or a non-uniform bed temperature (Sagar & Elangovan, 2017). A better understanding of the underlying phenomena causing these problems during SLS or other AM processes is necessary to improve these 3D printing processes. Performing experiments and computational simulations of sintering particles can help with this understanding. A proper model of the absorption of the laser energy by the particles is necessary to produce models which are capable of realistically simulating the sintering of powder beds.

Simulation of sintering particles

This work is part of a bigger project, which simulates the sintering of polymer particles. Here, two different materials are being simulated: PA12 and polystyrene (PS). While PA12 is a suitable crystalline material for SLS 3D printing, PS is an amorphous polymer which does not have a clear melting temperature. In general, amorphous polymers have a low degree of consolidation as the material only softens slowly when reaching temperatures higher than the glass transition temperature (Sagar & Elangovan, 2017). However, amorphous polymers such as PS in general come with a lower price compared to PA12 and are therefore often still used in AM (Brighenti et al., 2021). Therefore, both materials have been used for the simulations.

In previous studies, Hejmady has analysed the light absorption and sintering of PS particles (Hejmady et al., 2019) and PA12 particles (Hejmady et al., 2022). Here, two particles were sintered using a laser while measuring the neck radius and temperature evolution. Several variables were changed and their effect was measured. The results of these experiments will be used in this project to calibrate several variables necessary for the simulation of sintering particles in MercuryDPM. This research focuses on the light propagation and absorption by the particles, which will be used for these sintering simulations.

Goals and research questions

The goal of this research is to propose a model which can simulate the light propagation and absorption by a particle bed. For this, the following research question will be formulated:

How can the laser beam absorption in powder-based sintering processes be modelled?

Additionally, the following sub-questions will be used to answer this question:

Which variables affect the laser beam absorption in powder-based sintering processes?

How can the absorption model be simplified for computational friendly calculations?

In the conclusion of this paper, the found results of this research will be summarised and the research questions will be answered. Furthermore, some recommendations will be given for future research on this topic.

Outline of the paper

This research will introduce a laser absorption model which focuses on the particle scale. A ray tracing model will be used to discretise the laser beam into a finite number of rays which propagate in the particle bed. Several simulation variables and their effect on the laser absorption will be analysed. For each variable, a suitable set of values will be presented for the simulations in both 2D and 3D. Furthermore, a simulation simplification will be proposed which will replace the ray tracing simulations. These simplifications are a set of equations which are computationally friendly to execute. This way, the light absorption and therefore temperature increment of the particles can be calculated quickly, and subsequently be used in the sintering simulations in MercuryDPM. For this set of equations, several variables will be changed and tested, which will result in a light absorption model in which different bed and material properties can be used. The implementation of a semi-random walk, which replaces the ray tracing simulation, will also be investigated.

Assumptions and limitations

A common difference between amorphous and crystalline polymers is the structure of the polymer chains, which determine the opacity of the material. An opaque material causes light to scatter and not follow an expected single direction inside the material. Furthermore, the path and absorption of the light are affected by the light's wavelength and the shape of the particles (Liu, 2017). Even though in this research both an amorphous and a crystalline polymer are used, an assumption is made that there is no scattering inside the material and that the light follows an expected path for both materials. Furthermore, the particles are assumed to be perfectly spherical, which makes it easy to calculate the expected path for each light ray interacting with a particle. Lastly, the decision has been made to focus on a monodisperse particle bed. That is, all particles per bed used in the simulations have an equal diameter.

2 Ray tracing absorption model

In order to describe the energy absorption of a laser in powder beds, the incoming light beam is discretised and modelled as a finite number of rays, each following its own path while propagating into the powder bed. This model is presented by Osmanlic (Osmanlic et al., 2018), and is used in this research. In his model, each ray is traced which path it follows and by which particles it is absorbed, until it is completely absorbed or has left the bed. During this tracing, the rays undergo reflection and refraction when interacting with the particles.

2.1 Ray reflection and refraction

Fig. 1 shows a single ray with a direction $\vec{k}$ propagating in a straight line, until it encounters a change in medium after which it splits up into two new rays: a reflected ray directed away from the new medium ($\vec{k}_R$) and a transmitted ray directed into the new medium ($\vec{k}_T$). The incoming ray has an angle of incidence α relative to the surface normal $\vec{n}$. The reflected ray will have the same angle of reflection, while the transmitted ray has a different angle of refraction β due to a difference in refraction indices of the two media, n_A and n_B.
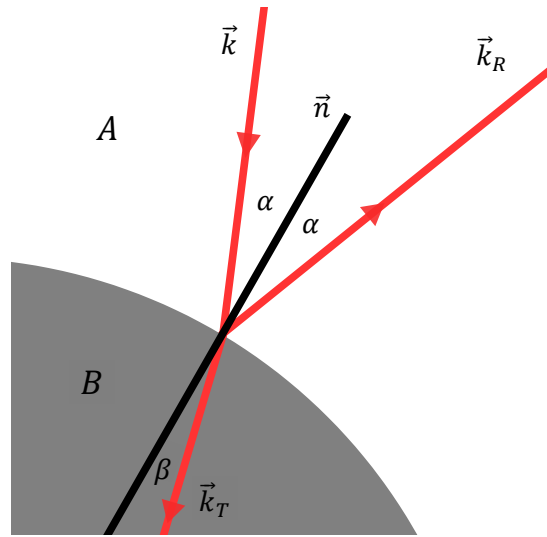

Fig. 1. Incoming light ray with direction $\vec{k}$ interacting with a particle, resulting in a reflected ray with direction $\vec{k}_R$ and a refracted ray with direction $\vec{k}_T$ due to a difference in refraction indices.

Geometrically, the angle of incidence can be calculated using the incoming ray with direction $\vec{k}$ and surface normal $\vec{n}$:

$$\alpha = \cos^{-1}\left(-\vec{k} \cdot \vec{n}\right) \tag{1}$$

The angle of refraction depends on the refraction indices of the two media, n_A and n_B, and the angle of incidence α:

$$\beta = \sin^{-1}\left(\frac{n_A}{n_B} \cdot \sin \alpha\right) \tag{2}$$

With both α and β in degree, n_A and n_B are dimensionless.

2.2 Energy absorption

Each ray has a certain amount of light energy I. Its units will be discussed later. Once the incoming ray splits into a reflected and a refracted ray, its initial light energy I_I is divided among the two new rays. The energy portion for each ray depends on the reflected energy portion factor R:

$$R = \frac{1}{2}\left(\left(\frac{n_A \cos\alpha - n_B \cos\beta}{n_A \cos\alpha + n_B \cos\beta}\right)^2 + \left(\frac{n_B \cos\alpha - n_A \cos\beta}{n_B \cos\alpha + n_A \cos\beta}\right)^2\right) \tag{3}$$

This causes the new reflected and transmitted ray to have a light energy of $I_R = R \cdot I_I$ and $I_T = (1 - R) \cdot I_I$ respectively.

While being in the surrounding air, the ray keeps its light energy as there is no interaction between atmospheric air and visible light, especially if the light contains high-energy photons (Kokhanovsky, 2015). The particle will absorb the laser energy, causing the energy of the raya to decrease. This decrease in energy can be described according to the Beer-Lambert law: the light energy I decreases exponentially while propagating in the material.

$$I(z) = I_0 e^{-\mu z} \tag{4}$$

With I_0 the initial light energy, μ the attenuation coefficient of the material in m^{-1} and z the propagated distance in m. If there is a high amount of interaction between the light and the medium, the energy absorption is also high. This indicates that the material has a high attenuation coefficient.

Relative energy

In this paper, the beam has a cross-section with a certain area and is discretised into N_{ray} rays, which also each have an area. The laser has an energy in J for a certain time period, and each light ray will have a portion of this energy. The area of each ray is assumed to be the average area it is occupying in the laser beam, thus $\pi r_{laser}^2 / N_{ray}$ with r_{laser} the radius of the laser beam. The laser has an energy profile which is not homogeneous, therefore the amount of energy of each ray will vary. Since the rays are thin, the energy profile inside each ray is assumed to be homogeneous and their shape is irrelevant. In the simulations, each ray is modelled as a line without a thickness for simplicity.

In Eq. (4), the used light energy for the rays is dimensionless since the Beer-Lambert law simply describes the reduction of energy with a certain factor, depending on the distance the light has travelled and the attenuation coefficient of the material: $e^{-\mu z}$. Conventionally for lasers, the optical intensity is used, which has the unit W/m^2. In this research, not the intensity but the energy will be used: the energy for a certain area in 1 second. Furthermore, every amount of energy will be divided by the energy of the laser before propagating into polymer particles. This will create a dimensionless relative energy, which will simply be referred to as "the energy". Therefore, the average energy of each ray is $1/N_{ray}$ [−] and their sum is 1 [−].

The advantage of using a relative energy is the fact that all energy portions, for example the portion of absorbed energy by a particle out of the total laser energy, will be a dimensionless number between 0 and 1. When the actual energy absorption of each particle in J needs to be known, this dimensionless number can simply be multiplied by the starting energy of the laser.

In this paper, two symbols will be used: I and E and are both dimensionless. I will refer to the energy each ray has and how it decreases during absorption, and splits during refraction. E will refer to the amount of energy that is absorbed by a particle or the amount of energy a particle receives.

3 Improved ray tracing model

Here, an improved version of the ray tracing absorption model for powder beds is introduced. Firstly, the model is analysed on 2D cases to establish a correct set of variables, after which 3D cases are analysed. In a separate stage of this project, experiments conducted by Hejmady will be used to calibrate several variables used in the modelling of particle collision during sintering (Hejmady et al., 2019). In Hejmady's work, the absorption of visible light (532 nm) in polystyrene (PS) with 2 wt% black dye was measured. This resulted in 6.45% of the energy being left after propagating in a sample sheet with a thickness of 100 μm. Inserting these numbers in Eq. (4), an attenuation coefficient can be found of $\mu = 27400$ m^{-1}, which is assumed to be independent of the temperature. For comparison, Hejmady also showed the absorption for PA12, which resulted in $\mu = 33500$ m^{-1}. This means that PA12 absorbs energy more quickly than PS. Furthermore, PS has a refraction index of $n_B = 1.5997$ (Sultanova et al., 2009) and $n_B = 1.525$ for PA12 (Polymerdatabase, n.d.).

3.1 2D simulations

Several simulations have been conducted which simulate several light rays, representing a laser beam, propagating through a bed of powder particles, represented by 2D circles. The light rays propagate in the bed with spatial steps of size Δl and at every step, the new light energy is calculated using Eq. (1). After every step, the simulation tests whether a change in medium has occurred and updates the ray direction $\vec{k}$ based on this. The objective of these simulations is to determine numerical three variables:

- The maximum *energy dissipation threshold* I_{min}. Eq. (4) is an exponentially decreasing function, therefore the light energy theoretically never reaches zero. This would cause the light rays to continue propagating indefinitely in the simulations, thus a threshold is necessary to define a point where a ray stops propagating. The energy at which the rays stop propagating is defined as the energy dissipation threshold and is expressed as a percentage of the average starting energy of a light ray. Since the total energy of the light beam is defined to be a dimensionless value of 1, the average energy of a light ray is $1/N_{ray}$, with N_{ray} the number of rays.

- The maximum spatial step size Δl. The step size refers to the distance to a new point in a single light ray where new calculations are made, along the direction of that ray. Fig. 2 shows 5 rays propagating into a 2D particle, showing the refraction and reflection, with Δl indicated. Note that this does not represent the distance the light has travelled in a certain time period.

- The minimum number of rays necessary to have accurate simulation results, with the rays representing a laser beam with infinite rays.
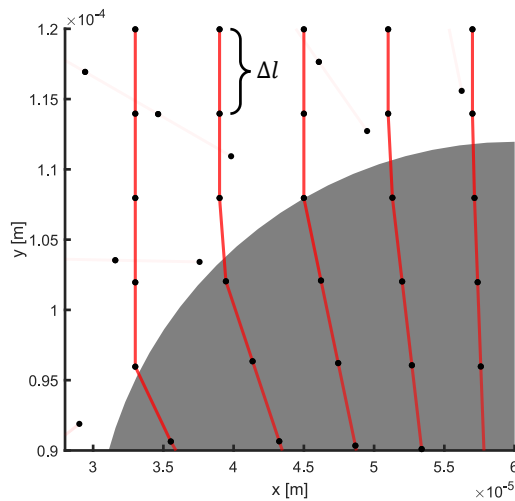

Fig. 2. A laser beam represented by several light rays interacts with a 2D particle, causing the rays to be split into reflected and refracted rays, with $\Delta l = 10\%$ of the particle diameter.

For the ray tracing simulations, MATLAB® was used to calculate the paths of all the rays. To have a clear idea of how these calculations are performed, Fig. 3 shows a schematic overview of the main steps during the calculation. The resulting ray positions are for a single time step and can be used to calculate how much laser energy every particle has absorbed. Additionally, the temperature increment caused by the laser can be determined based on this energy absorption.

Thereby, the following elements are checked for each new position calculation:

- Whether the energy of the ray has reached a value below the dissipation threshold
- If the new laser position is still within the borders of the bed
- Whether the new position has entered a different medium compared to its previous step

The starting rays are the rays coming from the top of the bed. The calculation is finished once all rays are either dissipated or have left the bed. All of the MATLAB® code used to calculate the ray paths and visualise the absorption is made publicly available and can be accessed via the link given below[1].
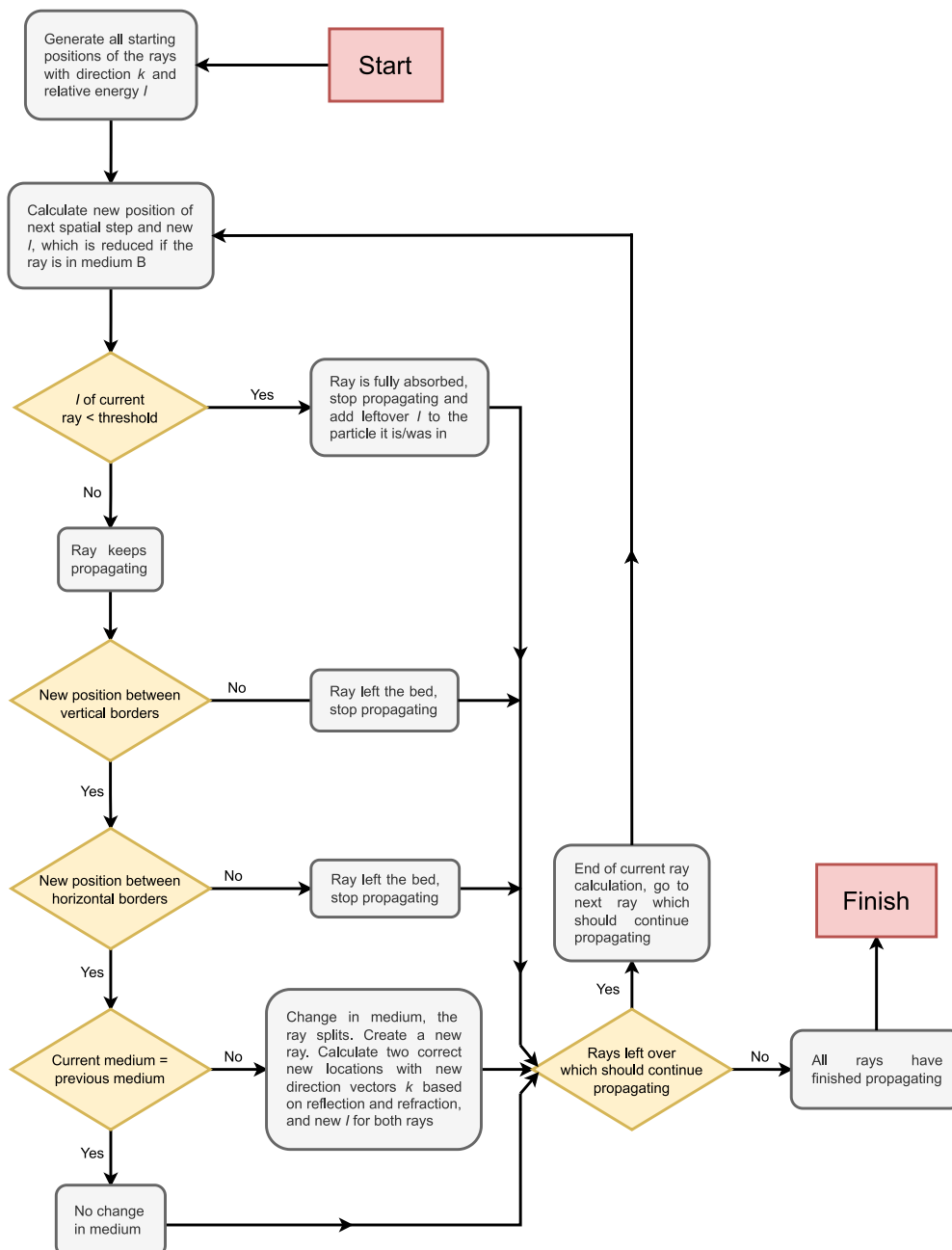

Fig. 3. Schematic overview of the main calculation steps performed in MATLAB® during the ray tracing simulations.

1. https://github.com/BertNijkamp/Laser-Beam-Absorption.git

11

3.1.1 Energy dissipation threshold

Fig. 4 (a) shows 2D simulation results of propagating light rays with equal energies on three particles, numbered 1 to 3 as indicated, using an energy dissipation threshold of 1%, thus $I_{min} = 0.01/N_{ray}$. In Fig. 4 (b), the absorbed energy is plotted for several values for the dissipation threshold. As can be seen, below a threshold of 1% of the starting energy, the resulting amount of absorbed energy does not change significantly anymore. Appendix A and B show that similar results were observed with more particles and for 3D simulations. Therefore, 1% will be used as the energy dissipation threshold. If a different attenuation coefficient would be used, the height of the two lines Fig. 4 (b) change, however, the ideal threshold will remain at 1%.
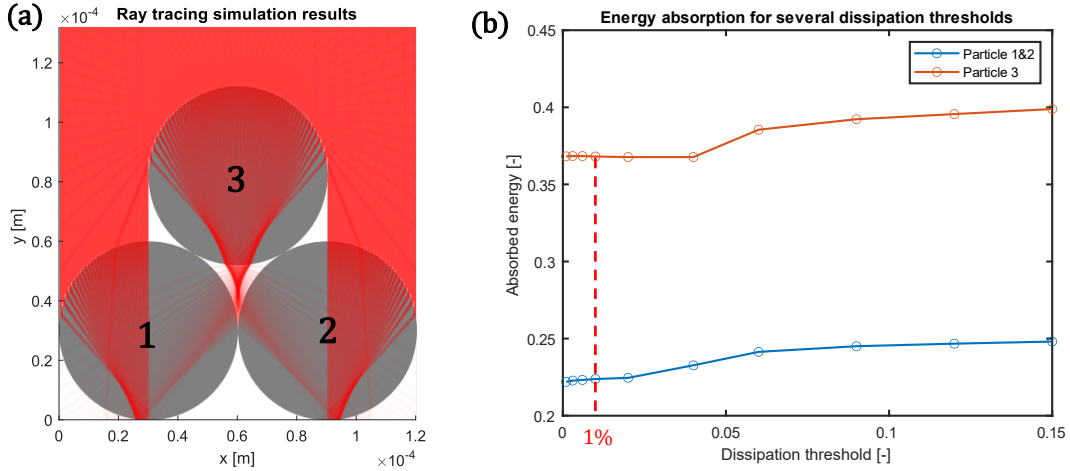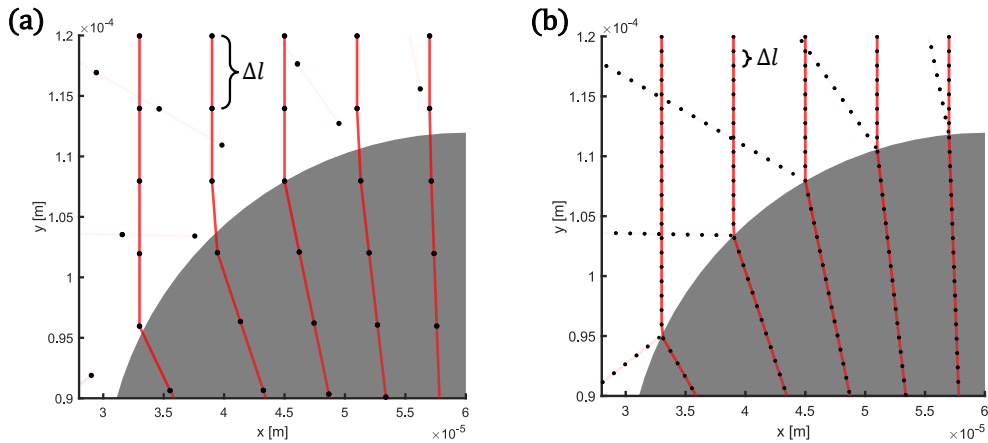

Fig. 4. (a) 2D simulation results of light rays propagating into three particles numbered 1, 2 and 3. (b) Resulting absorbed energy per particle out of total incoming energy, plotted for several different dissipation thresholds.

3.1.2 Spatial step size

Subsequently, the energy absorption for different spatial step sizes Δl was studied. Fig. 5 (c) shows the absorbed energy for several different spatial step sizes expressed as a percentage of the particle diameter. The simulations have been coded in such a way that the incoming rays always result in the exact same reflected and refracted rays, independent of the step size. This can be seen in Fig. 5 (a) and (b) where a spatial step size of 10% and 2% of the particle diameter is used. Here, the reflected ray is visually not connected to the intersection point. Once the spatial step size is set to a too high value, rays might happen to completely miss a particle and therefore not reflect and refract. This can be seen in Fig. 5 (c) as the amount of absorption per particle is fluctuating randomly for high values of Δl. As can be seen, below a spatial step size of 10%, the resulting absorbed energy does not change significantly. Appendix C and D show that similar results are observed with more particles and for 3D simulations. Therefore, a spatial step size of 10% of the particle diameter will be used.
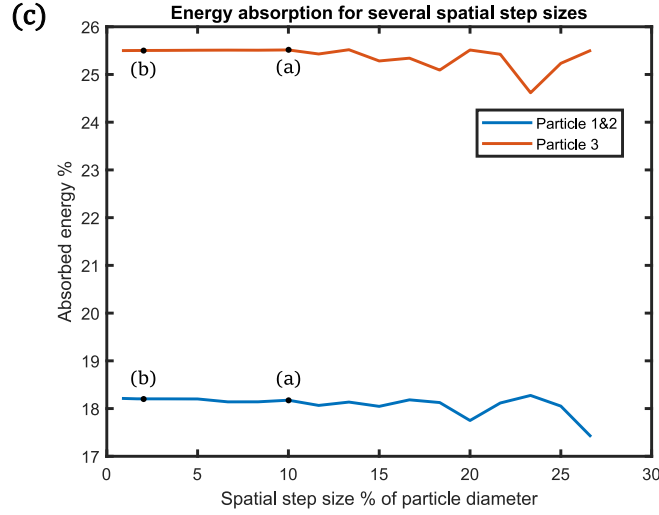
Fig. 5. (a) Two light ray simulation results showing identical ray positions while using different spatial step sizes of 10% and (b) 2% of the particle diameter. (c) Resulting absorbed energy per particle out of total incoming energy, plotted for several different spatial step sizes and indicating the positions of the simulations shown in (a) and (b).

3.1.3 Number of light rays

The number of light rays, N_{ray}, was found to be a variable which is case specific. It will depend on the configuration of the particles and the required level of preciseness. Fig. 6 (a) - (c) show the 2D simulation results of two overlapping particles, where the amount of *relative overlap* δ_n is altered. ($\delta_n = 0 \rightarrow$ no overlap, $\delta_n = 1 \rightarrow$ complete coalescence) The total amount of absorbed energy for each specific relative overlap is shown on the y-axis. Here, three different number of light rays N_{ray} are used: 100, 1000 and 10000 rays respectively.
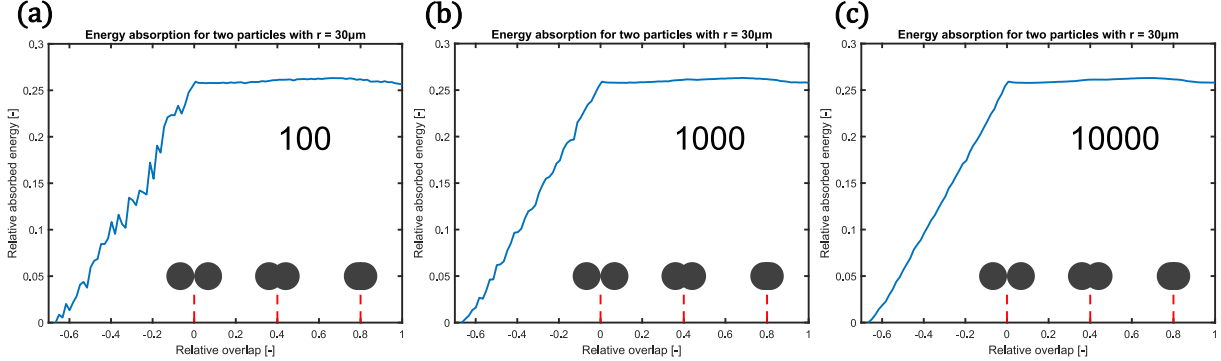

Fig. 6. Relative absorbed energy of two overlapping 2D particles for several different amounts of overlap using (a) 100, (b) 1000 and (c) 10000 rays. These rays are randomly divided over a laser width of 40 μm with its centre located between the particles, which both have a diameter of 60 μm.

As can be seen, a low number of rays results in a higher randomness of the amount of absorption. The conclusion which can be drawn is that a higher number of rays result in a more consistent result, but at the cost of a higher simulation time. For any specific simulation case, 2D or 3D, several numbers of rays need to be considered and a compromise needs to be made between accuracy and simulation time.

3.1.4 Curvature approximation

During the 2D particle simulations (also occurring during the 3D simulations), some phenomena occurred which caused problems with the light propagation. To have a good comparison between the simulations and the experiments conducted by Hejmady (Hejmady et al., 2019), the following phenomenon needs to be taken into account: at the intersection between two sintering and therefore "overlapping" particles, a curvature can be observed between the two spheres. As an example, this is visualised in Fig. 7 (a) from two sintering PA12 particles. This coalescence process

13

is reported by Alvarez et al. (Alvarez et al., 2021). Fig. 7 (b) shows a 2D light ray simulation of two spheres with this curvature taken into account, which is generated using the tool Ray Optics Simulation (Yi-Ting & Johnson, 2016). This shows that the light bends evenly in all directions at the intersection. It was found that the radius of this curvature does not significantly affect the light propagation (see Appendix E), but the phenomenon itself does need to be considered. If no curvature would be used, as shown in Fig. 7 (c), the light rays close to the intersection would refract into only one of the particles, creating a distinct separation of the light beam.
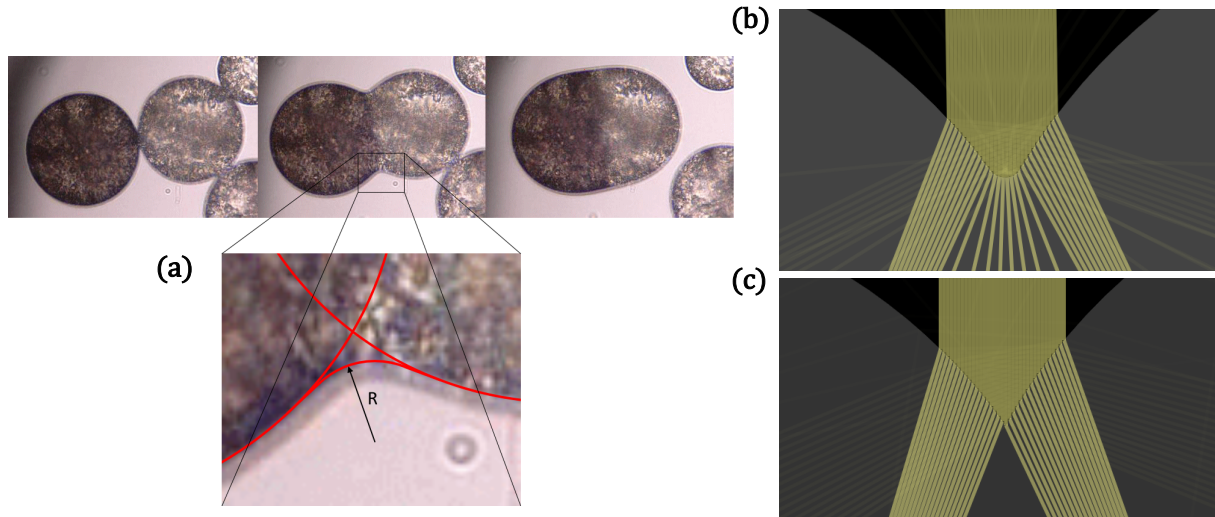

Fig. 7. (a) Two sintering PA12 particles showing a curvature at the intersection, these images were taken using hot-stage microscopy at the University of Twente (Alvarez et al., 2021). (b) Light rays evenly bending in all directions due to a curvature at the particle intersection, versus (c) no curvature, showing a clear separation of the incoming beam.

In the simulations, perfect circles or spheres are used and it is therefore not possible to create a curvature at each intersection using this method. Therefore, the phenomenon is approximated by choosing a surface normal direction somewhere between the surface normals of the two particles at the point of intersection, when calculating the refraction and reflection directions. If a light ray has a point in space outside of any particle and one spatial step (Δl) further in two or more particles, as shown in Fig. 8 (a), the normal vector $\vec{n}$ used for the reflection and refraction calculation will have a weighted value based on the normal vectors of these particles at the point of intersection, depending on how close the ray is to each particle. This mimics a curvature between the particles, as indicated by the green curved line and its surface normal, shown in Fig. 8 (b). This results in Fig. 8 (c), showing that the light rays coming from the intersection of the two particles are evenly divided between the refracted rays just outside of the intersection zone.
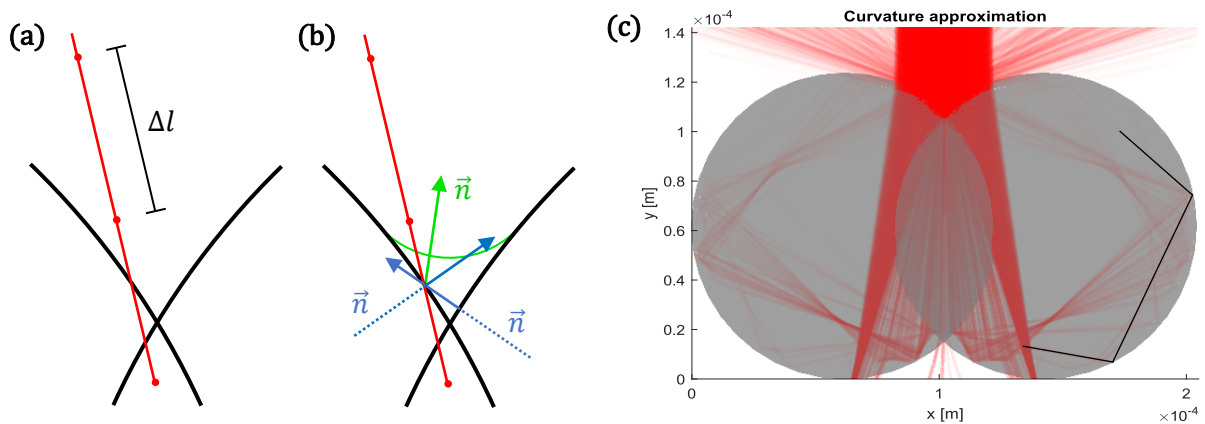

Fig. 8. (a) A light ray having a point outside of any particle, and one Δl further in two overlapping particles. (b) The weighted value for the normal vector used in calculations (green), based on the normal vectors of the particles at the intersection point (blue), which mimic a curvature. (c) Resulting 2D simulations showing rays refracting evenly.

3.1.5 Total internal reflection

The introduction of this curvature approximation introduces another problem. As can be seen in Fig. 7 (c), some light rays reflect internally with a large angle of incidence α, for example the ray indicated by the black lines. If $\alpha > \sin^{-1}\left(\frac{n_B}{n_A}\right)$, which is the case for the black line, the light ray will experience total internal reflection (TIR). This means that the light ray will be completely reflected and no rays are refracted into the external medium, the air. Since the particle is assumed to be a perfect sphere, the next intersection point of this reflected ray and the boundary of the particle will have the same angle of incidence. Therefore, the light ray keeps experiencing TIR and all of the light will eventually be absorbed by the particle. In the simulations, this situation can be simplified by stopping the propagation of any light ray experiencing TIR and adding all of the energy that's left in that ray to the particle it is inside, even though the energy dissipation threshold has not yet been reached.

3.2 3D simulations

The next step is to execute the steps of the model described in section 3.1 to light rays propagating in a particle bed in three dimensions. This particle bed is generated using MercuryDPM, a code library for discrete particle simulations (Weinhart et al., 2019). The laser beam is modelled as a finite number of light rays starting in a circle. The energy of each ray depends on the distance to the centre of the beam. Yaagoubi et al. (Yaagoubi et al., 2021) show that the light energy distribution in a CO_2 laser (which is a common laser type in SLS) can be approximated by a Gaussian curve. The laser energy modelled as a Gaussian curve can be expressed as:

$$I_0(d,\sigma) = \frac{1}{\sigma\sqrt{2\pi}}e^{\frac{-d^2}{2\sigma^2}} \tag{5}$$

With d the distance from a ray to the laser centre perpendicular to the propagation direction in m and σ the standard deviation in m, which Yaagoubi et al. show is half the laser radius in this situation.

However, Eq. (5) only applies to two dimensions: it has a surface area of 1 when integrating from $-\infty$ to ∞. In 3D, the equation needs to be rotated around the axis parallel to the propagation direction and integrated from 0 to 2σ, then the volume V needs to be 1. Here, it is assumed that the edge of the laser ends at 2σ and the energy outside the laser area is 0.

$$V = \int_0^{2\sigma} 2\pi d \cdot I(d,\sigma)\,\mathrm{d}d = \int_0^{2\sigma} \frac{2\pi d}{\sigma\sqrt{2\pi}}e^{\frac{-d^2}{2\sigma^2}}\,\mathrm{d}d = \int_0^{2\sigma} \frac{d\sqrt{2\pi}}{\sigma}e^{\frac{-d^2}{2\sigma^2}}\,\mathrm{d}d \tag{6}$$

$$u = \frac{-d^2}{2\sigma^2}, \quad \mathrm{d}u = \frac{-d}{\sigma^2}\,\mathrm{d}d \tag{7}$$

$$V = \int_0^{2\sigma} -\sigma\sqrt{2\pi}e^u\,\mathrm{d}u = \left[-\sigma\sqrt{2\pi}e^{\frac{-d^2}{2\sigma^2}}\right]_0^{2\sigma} = -\sigma\sqrt{2\pi}e^{\frac{-4\sigma^2}{2\sigma^2}} + \sigma\sqrt{2\pi}e^0 = \sigma\sqrt{2\pi}(1-e^{-2}) \tag{8}$$

Which is a function of σ and therefore not equal to the constant value 1. Therefore, Eq. (5) needs to be divided by $\sigma\sqrt{2\pi}(1-e^{-2})$:

$$I_0(d,\sigma) = \frac{1}{2\pi\sigma^2(1-e^{-2})}e^{\frac{-d^2}{2\sigma^2}} \tag{9}$$

In here, 2σ can be replaced by the laser radius r_{laser}:

$$I_0(d,r_{laser}) = \frac{2}{\pi r_{laser}^2(1-e^{-2})}e^{\frac{-2d^2}{r_{laser}^2}} \tag{10}$$

When rotating around the axis parallel to the propagation direction and integrating from 0 to r_{laser}, this equation does give a volume of 1. However, in the simulations, the laser beam is discretised by using many light rays. Therefore, when the light rays are created and are given a starting energy based on their location within the laser beam, the energy needs to be multiplied by the average area it is occupying to create a volume. This way, the total sum of the energies of all rays, or the sum of all volumes, will be 1. The average area a ray will occupy is the total laser beam area divided by the number of rays, $\pi r_{laser}^2/N_{ray}$. The equation used in the simulations to determine the starting energy of each ray is therefore as follows:

$$I_0\big(d, r_{laser}, N_{ray}\big) = \frac{2}{N_{ray}(1 - e^{-2})} e^{\frac{-2d^2}{r_{laser}^2}} \tag{11}$$

With d the distance of a ray to the laser centre in m. When creating the starting coordinates of the light rays, each ray is given the following information:

- A coordinate, which is randomly chosen in a circle with a radius r_{laser}, just above the bed
- A direction $\vec{k}$, for example pointing downwards, parallel to the z-axis: $[k_1\ k_2\ k_3] = [0\ 0\ -1]$
- A starting energy I_0 according to Eq. (11)

When using a direction other than with a laser angle of $\theta = 0°$, the model is written such that it takes into account the elliptical shape the laser beam has instead of a circular shape, as shown in Fig. 9 (a) and (b).
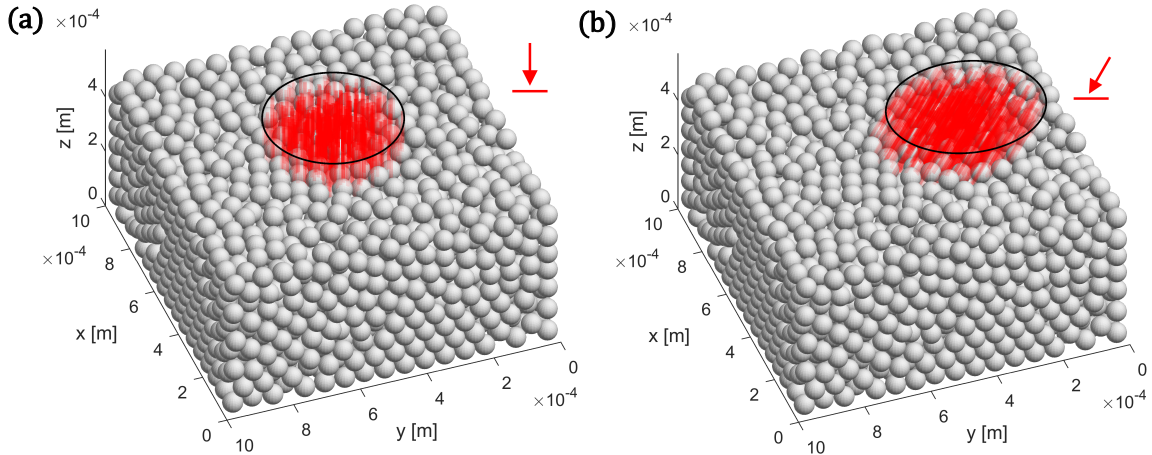

Fig. 9. (a) A circular laser beam at the top of the bed due to perpendicular laser direction. (b) An elliptical laser beam at the top of the bed due to non-perpendicular laser direction of $\theta = 30°$.

Next, the position of the light ray one spatial step further will be calculated according to the steps used in Fig. 3, for every light ray. As mentioned above, the particle bed will be generated using an insertion and compression code in MercuryDPM. Here, the volume fraction φ can be set to a desired value, ranging from $\varphi = 0.575$ to $\varphi = 0.7$. The volume fraction can physically not be lower since gravity causes the particles to sink and therefore the total bed volume will also be lower. The volume fraction can physically not be higher since the particles cannot overlap. The densest possible sphere stacking of monodisperse particles without overlap is for a hexagonal close sphere packing (HCP), which has a volume fraction of $\varphi \approx 0.74$. Therefore, φ will always be lower than this.

Once the generated particle bed is loaded in MATLAB® and the simulation is started, the light rays keep propagating in the bed until all rays are fully absorbed or have left the bed. Since per particle the amount of absorption is saved, the bed can be shown with a given colour, indicating the amount of absorption. Fig. 10 shows a particle bed with this absorption after executing the ray tracing simulation. A more red colour indicates a higher absorption.
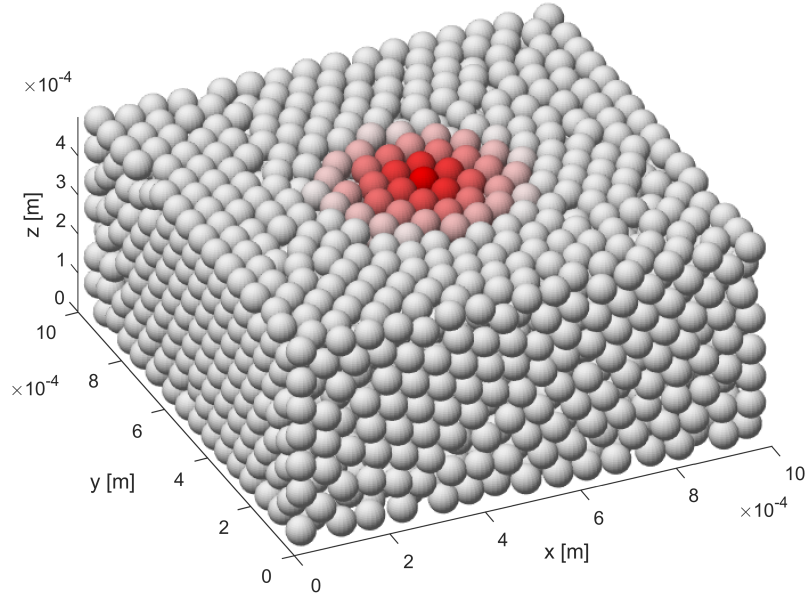
Fig. 10. 3D simulation results of the light absorption by the particles in a bed of 1 x 1 x 0.5 mm, using a monodisperse bed of 2653 particles with a diameter of 60 μm and a laser spot radius of 200 μm using 10000 rays and $\theta = 30°$.

Fig. 10 shows a visible region in which the particles absorb part of the incoming light, as well as a certain region within the bed. The next step is to calculate the change in temperature caused by the light absorption per particle.

3.3 Temperature evolution

Based on the amount of absorption and particle size, each particle will raise in temperature for a certain time step Δt. Hejmady showed that due to the small Biot number (Bi≪0.1), a homogeneous particle temperature can be assumed (Hejmady et al., 2019). Since the simulation is for a single time step, the simulation gives the increment in temperature compared to the previous time step, thus not the temperature itself. This change in temperature ΔT in °C can be calculated using the following equation:

$$\Delta T = \frac{P_{in} \cdot E \cdot \Delta t}{m \cdot c_p} \tag{12}$$

With P_{in} the laser power in W, E the portion of absorbed energy out of the total incoming energy [−], Δt the time step in seconds, m the particle mass with $m = V \cdot \rho = \frac{4\pi}{3} r^3 \cdot \rho$ in kg and c_p the specific heat capacity in J/kgK. This temperature change due to the laser can be used in the sintering model implemented by Alvarez et al. (Alvarez et al., 2021) in MercuryDPM to describe the temperature evolution of the bed. Here, aside from the effects of the laser, the temperature evolution is also affected by the convection, conduction and radiation inside the bed. Eq. (12) can be used to calculate the part of the energy balance that describes the effect of the laser.

The sintering simulations have several stages with different time scales (Bierwisch et al., 2020):

- The propagation of the laser beam in the powder bed, practically instantaneous
- The heating of the particles due to laser exposure, in the order of microseconds
- The thermal diffusion of the heat through the bed, in the order of milliseconds
- The viscous flow and thereby sintering of the particles, in the order of seconds

The laser absorption model presented in this research will be able to simulate the first two stages, and outputs the energy absorption of the particles and thereby the temperature increment caused by the laser ΔT for each particle. The results in this work will be used for the sintering simulations in MercuryDPM, where the thermal diffusion and viscous flow kinetics are modelled.

17

4 Simulation simplification

The MATLAB® ray tracing simulations will be used to determine the temperature increment for each particle during the sintering simulation in MercuryDPM. However, it was found that during the ray tracing simulations, many time-consuming calculations had to be performed. For every ray, the code checks whether the new spatial step was inside or outside any particle, and if so, which particle. For many rays and many particles, this resulted in long calculation times. For example, the simulation shown in Fig. 10 which used 10000 rays with 2653 particles, took roughly 85 minutes to complete. Even if the code would be further optimised, for example by checking which next particle would be hit by a light ray instead of checking all the particles for every spatial step, the simulations were found to take a considerable amount of time. Especially considering the fact that the simulation needs to be performed every time step in MercuryDPM during the sintering simulation, since the positions of the particles and/or the laser will be different every time step.

In this work, two types of simplifications will be made. The first method will find replacement equations which can calculate the energy absorption for each particle. These newly found equations will have several variables as an input and can very rapidly give the energy absorption E_{abs}, therefore being much more efficient compared to the ray tracing simulations. This energy absorption E_{abs} can be used to find the change in temperature using Eq. (12). The ray tracing simulations will be used to obtain these replacement equations. This simplification will firstly be done for a particle pair, from now on referred to as a particle doublet, which will be used to calibrate several variables for the simulations in MercuryDPM based on the experiments by Hejmady. Secondly, the simulation will be done for a powder bed.

The second simplification will investigate the implementation of a random walk. Here, the phenomenon of light rays propagating into a powder bed will be replaced by rays performing a random walk in a bed with virtual particles.

4.1 Particle doublet

In MercuryDPM, several variables are required for the simulation of sintering kinetics in a polymer bed, for which experiments conducted by Hejmady will be used to calibrate these variables (Hejmady et al., 2019). In these experiments, the light absorption of two sintering PS particles was analysed. During the sintering, one of the measured variables is the amount of overlap between the two particles, which can be expressed as the relative overlap δ_n. To determine the relative amount of energy absorption E_{abs} in this research, the ray tracing simulations will be performed on two particles where δ_n will be varied. Then, E_{abs} can be plotted against δ_n and a fitting curve can be found.

4.1.1 Simulation setup

For the ray tracing simulations of the particle doublets, the setup will be directly compared to the conducted experiments. Therefore, the following properties are used, which are analogous to the experiments:

- The two particles have the same diameter
- The starting diameters are equal to one of the values mentioned below, ranging from 60 μm to 210 μm
- The diameter of overlapping particles becomes larger due to the conservation of volume, the derivation for this diameter increase is explained in Appendix F.
- The material of the particles is polystyrene (PS) with the following properties:
  - Attenuation coefficient $\mu = 27400$ m^{-1}
  - Refractive index $n_B = 1.5997$
  - Density $\rho = 1040$ kg/m^3
  - Specific heat capacity $c_p = 1320$ J/kgK
- The laser spot radius $r_{laser} = 20$ μm

- The laser pulse energy is 29 μJ with a pulse duration of 800 ms
- The laser has an angle of $\theta = 60°$ with respect to the bed
- The direction of the laser is perpendicular bisector of the line between the centres of the particles, see Fig. 11 (a) – (c)
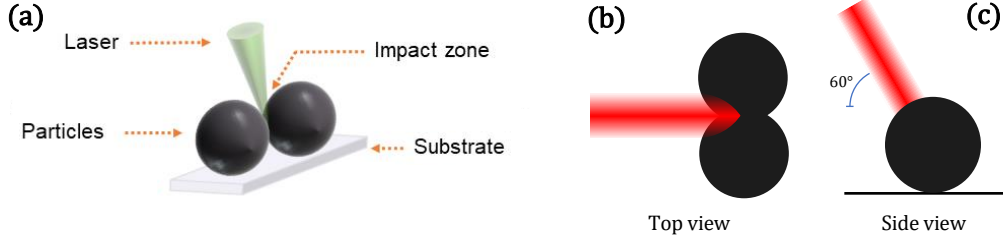- The floor perfectly reflects the light rays

Fig. 11. (a) Figure taken from Hejmady (Hejmady et al., 2019) showing the experiment setup. (b) Top view and (c) side view, showing the laser and the particle doublet position.

The sintering experiments for particle doublets were performed for five different particle diameters: 60, 120, 150, 180 and 210 μm, while the laser spot radius was kept constant at 20 μm. For completeness, a diameter of 90 μm is also added for the simulations. Here, δ_n is varied between $-\frac{2r_{laser}}{D} < \delta_n < 1$ with steps of $\delta_n/60$. Namely, at $\delta_n = -\frac{2r_{laser}}{D}$, the laser beam fits perfectly in the gap between the particles, thus any higher δ_n will result in an absorption by the particles. Since the setup is symmetric, the amount of absorption between the two particles is assumed to be equal. In the simulations, this is not always true since the rays are randomly placed in a circle and it is therefore possible that the number of rays hitting each particle is unequal. Therefore, the average of the absorption of the two particles is used as the final result. Furthermore, $N_{ray} = 10000$ was found to give a consistent result, Fig. 13 shows the absorption with minimal variance.

4.1.2 Simulation results

In Fig. 12, several simulation results are shown for $D = 120$ μm and δ_n ranging from $-1/3$ to 1. These simulations clearly show differences in light reflection when the relative overlap is varied. At $\delta_n = 1/4$, a relatively big portion of the energy is reflected away from the top, and when δ_n is approaching 1, the light rays are more converging. Furthermore, the increase of the particle diameter can also be seen as the figures use the same dimensional scale.
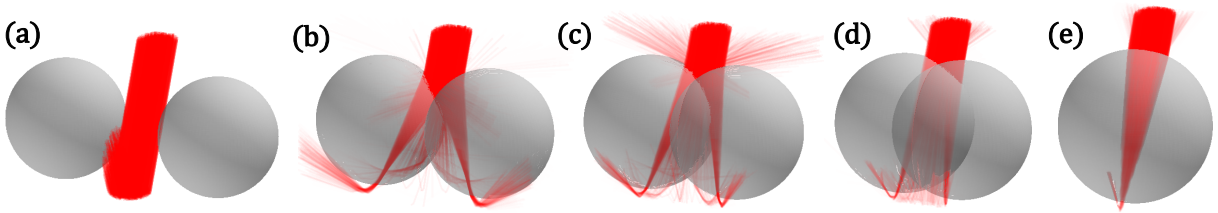

Fig. 12. Particle doublet simulations with varying δ_n: (a) $\delta_n = -\frac{1}{3}$, (b) $\delta_n = \frac{1}{20}$, (c) $\delta_n = \frac{1}{4}$, (d) $\delta_n = \frac{1}{2}$ and (e) $\delta_n = 1$.

Fig. 13 shows the other simulation results, where the amount of absorbed energy per particle E_{abs} is plotted against the relative overlap δ_n. As expected, the amount of absorbed energy is higher when the particles are closer together but don't overlap yet, as there is more overlap between the laser and the particles. Furthermore, a bigger particle will absorb more energy. This is because the light path inside the particle is longer, therefore more energy is absorbed. Furthermore, a smaller particle has a higher curvature, causing more rays to reflect sideways. For a bigger particle, the rays have a smaller angle of incidence and less light is reflected away. For the six lines in this graph, each for a different particle diameter, a fitting curve can be found. Each line is divided into three segments, based on the best fitting curves. The fitting curves are a polynomial equation with seven coefficients, and are thus in the following form:

$$E(\delta_n) = a_1 \delta_n{}^6 + a_2 \delta_n{}^5 + a_3 \delta_n{}^4 + a_4 \delta_n{}^3 + a_5 \delta_n{}^2 + a_6 \delta_n + a_7 \tag{13}$$

The coefficients a_1 till a_7 are listed in Table 1. They are specific for each particle diameter and for a certain range of δ_n.

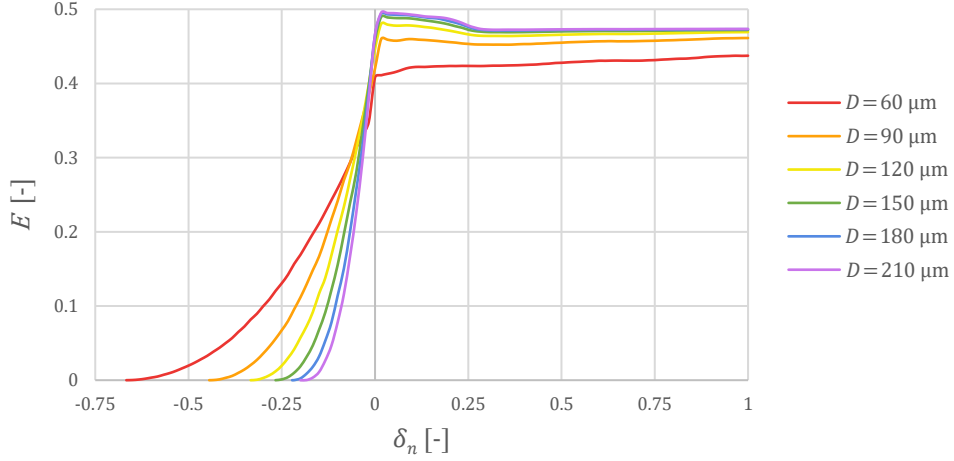Energy absorption for two particles with laser radius of 20 µm

Fig. 13. Energy absorption per particle for a particle doublet with varying radii and relative overlap.

D	range δ_n min	max	coefficients a_1	a_2	a_3	a_4	a_5	a_6	a_7
	-1/3	0	0	0	0	0.28554	1.2250	1.2453	0.37105
60	0	0.35	314.59	-367.22	162.90	-32.804	2.4532	0.078785	0.40859
	0.35	1	0	-2.8938	9.6552	-12.463	7.7529	-2.2978	0.68349
	-4/9	1/60	0	0	0	0.94519	3.0664	2.1237	0.42204
90	1/60	0.35	323.00	-430.25	222.94	-55.369	6.5125	0.32849	0.46399
	0.35	1	0	-1.5684	5.2133	-6.6918	4.1275	-1.2049	0.58532
	-1/3	0	0	0	-27.450	-16.770	1.5455	2.6874	0.44047
120	0	0.35	-75.265	18.048	31.339	16.302	2.5810	0.17915	0.48278
	0.35	1	2.0182	-9.0506	16.390	-15.298	7.7370	-1.9959	0.66857
	-4/15	0	0	0	0	5.9195	10.077	3.9851	0.45961
150	0	0.35	-370.78	366.04	-124.90	17.334	-1.0477	0.006738	0.49001
	0.35	1	1.6030	-6.9856	12.355	-11.316	5.6406	-1.4401	0.61567
	-2/9	0	0	0	0	14.001	16.294	5.0271	0.46722
180	0	0.35	-662.88	674.13	-265.75	47.086	-3.9828	0.11470	0.49274
	0.35	1	1.1714	-5.0683	8.9151	-8.1354	4.0467	-1.0332	0.57678
	-0.2	0	0	0	0	23.338	22.625	5.9277	0.46915
210	0	0.35	-975.88	1115.3	-474.90	93.664	-8.8715	0.32789	0.49169
	0.35	1	1.0049	-4.2949	7.4792	-6.7734	3.3525	-0.85452	0.55980

Table 1. Polynomial coefficients for fitting curve used to calculate E for a specific D and any δ_n in a certain range.

The fitting curves result in a good overlap with the lines shown in Fig. 13. Due to the usage of these fitting curves, the sintering simulation in MercuryDPM does not need to perform a ray tracing simulation, simply the polynomial equation can be used to calculate the relative amount of absorbed energy per time step using Eq. (13). Next, the sintering simulations will be compared to the data from Hejmady's experiments. Fig. 14 (a) shows a graph with the dimensionless neck radius x_i/a_0 on one axis, which is the radius of the interface between the two particles x_i, divided by the starting radius a_0. For full coalescence ($\delta_n = 1$), the dimensionless neck radius is $x_i/a_0 = \sqrt[3]{2} \approx 1.26$.

Fig. 14 (b) shows the location of x_i. Fig. 14 (a) shows an increase of x_i/a_0 over time during sintering, until it reaches the final neck radius after about 0.8 seconds. In a previous research,

Alvarez simulates the neck growth kinetics in MercuryDPM (Alvarez et al., 2021). The results from Eq. (13) and Table 1, together with Hejmady's experiments, can now be used for the calibration of several variables used in these simulations. These results are shown in Appendix G.
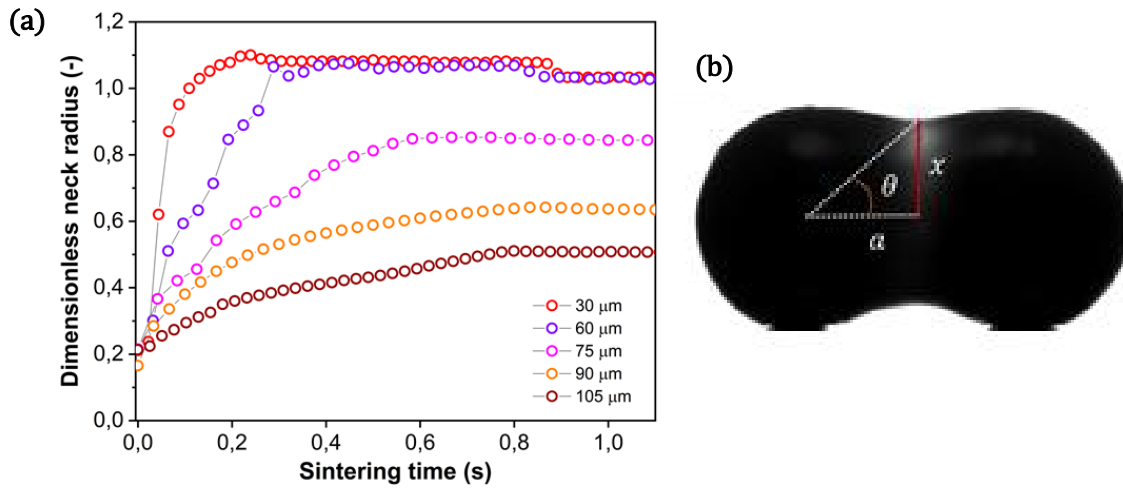

Fig. 14. (a) Experiment results of sintering PS doublets by Hejmady for several particle sizes. (b) Sintering particle doublet showing the neck radius x_i.

4.1.3 Dimensionless neck radius approximation

From Fig. 14 (b) it can be seen that there is a curvature between the interface of the two sintering particles. This curvature causes the neck radius to be larger compared to when no curvature would be present. This can be seen in Fig. 15 (a) and (b), where both figures have particles with the same diameter but show a different neck radius.
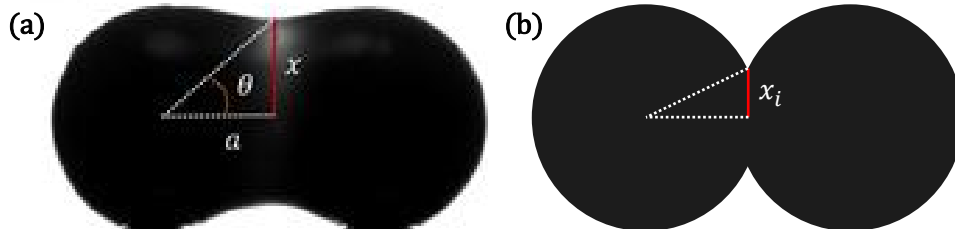

Fig. 15. (a) Sintering particle doublet with a curvature and (b) an illustration of two particles with an equal diameter and distance, but without a curvature, showing a smaller neck radius.

The size of this neck radius could be calculated based on having the total volume of the new shape equal to two separate particles, but this would require integrating and rotating the equation of three circle sections. This equation might not even be solvable and would be calculation intensive when applied to a large number of particles. Therefore, an approximation is used.

To show how the neck radius relates to the amount of overlap, two spheres were modelled in 3D software and the neck radius was measured. A starting radius of 1 was used and therefore the dimensionless neck radius is equal to the neck radius itself. Here, three different cases were used:

- Two particles with a constant radius and no curvature
- Two particles with an increasing radius to maintain a constant volume and no curvature
- Two particles with an increasing radius with a curvature, with a radius equal to 50% of the overlap

Fig. 16 shows these three different situations where x_i/a_0 is plotted against δ_n.
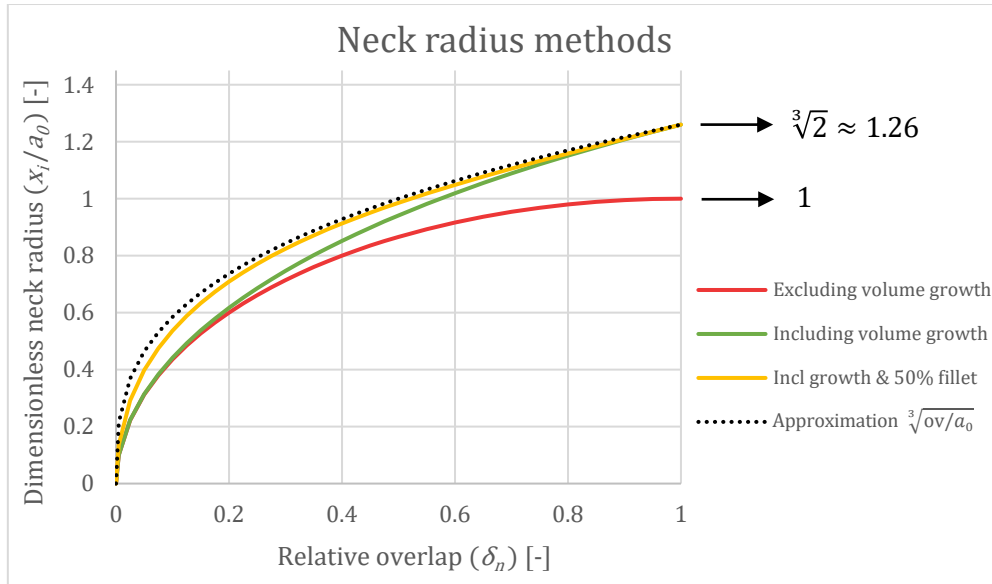
21

Fig. 16. Dimensionless neck radius plotted against the relative overlap for several different types of overlapping spheres.

The red line shows the dimensionless neck radius when the particles maintain a constant radius. When the particles are fully overlapping ($\delta_n = 1$) the dimensionless neck radius is 1 as it is equal to the particle's radius. When the radii do change according to the conservation of volume, this value ends up at $\sqrt[3]{2} \approx 1.26$ at full overlap (green line). This is similar to the case which includes a curvature (yellow line), however, it can be seen that x_i/a_0 is much higher for a low δ_n compared to the case without a curvature.

The graph also shows an approximation (dotted line), which is simply the cubic root of the overlap divided by the starting radius, $\sqrt[3]{ov/a_0}$ with ov the physical particle overlap in m. Here, the overlap takes into account no volume growth. Thus, it is always equal to two times the original radius, minus the distance between the centres. Therefore at $\delta_n = 1$, the overlap is twice the original radius and the approximation also results in $\sqrt[3]{2}$. The dotted line shows a good approximation compared to the particles which includes a fillet, and requires significantly less time to be calculated compared to the actual value, if an equation could be found. The approximation $x_i/a_0 = \sqrt[3]{ov/a_0}$ is therefore used in MercuryDPM to calculate the dimensionless neck radius.

4.2 Powder bed

The next simplification is done for a powder bed. In this section, the replacement equations will be formulated. The following variables are proposed to influence the energy absorption in a powder bed and will therefore be inputs of the replacement equations:

- Position of a particle relative to the laser
  - Perpendicular distance to the laser centre d [m]
  - Depth within the bed parallel to the laser z [m]
- Radius of the laser r_{laser} [m]
- Power of the laser P_{in} [W]
- Diameter of the particle D [m]
- Density of the particle ρ [kg/m³]
- Specific heat capacity of the particle c_p [J/kgK]
- Refraction index ratio $x = n_A/n_B$ [-]
- Attenuation coefficient of the particle μ [m^{-1}]
- Volume fraction of the bed φ [-]

The volume fraction of the bed is calculated by dividing the total volume of the particles by the volume of the bed, where the top of the highest particle is used for the height of the bed. For clarity, some variables are shown in Fig. 17:
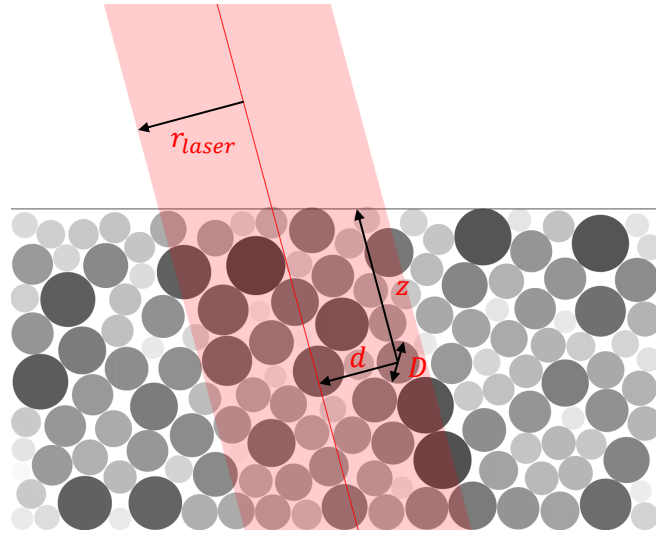

Fig. 17. Particle bed with laser beam showing several variables used as an input for the replacement equations.

This section will first focus on the energy absorption in the top layer, which will be calculated analytically. Then, the absorption in the rest of the particle bed will be calculated. Lastly, several variables of the bed and the material will be changed to check whether the replacement equations still comply with these changes.

4.2.1 Energy absorption for the top layer

Here, the top layer of a monodisperse particle bed is considered, as this layer absorbs the most amount of energy. The following section uses the same simulation shown in Fig. 10. Fig. 18 shows the amount of absorbed energy E_{abs} (with a total incoming energy of 1) as a function of the distance to the centre of the laser for each particle. Here, the laser is perpendicular to the bed.
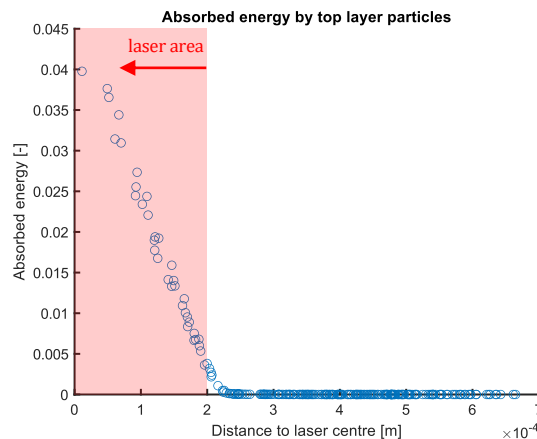

Fig. 18. Absorbed energy per particle E_{abs} vs the distance to the laser centre, for particles in the top layer of a particle bed with 2653 particles with a diameter of $D = 60$ μm and with a laser spot radius of $r_{laser} = 200$ μm.

As seen in Fig. 18, the particles in the top layer outside of the laser area absorb no energy. The particles inside the laser area absorb energy, with more absorption in the centre as the laser energy is higher here. This energy is according to a Gaussian curve, which can be observed in the amount of absorption of the particles within the laser area. Fig. 19 shows these particles with the relative distance to the laser centre on the horizontal axis, together with a fitting Gaussian curve. A relative distance of 1 is at the outer edge of the laser, 0 is at the centre of the laser.
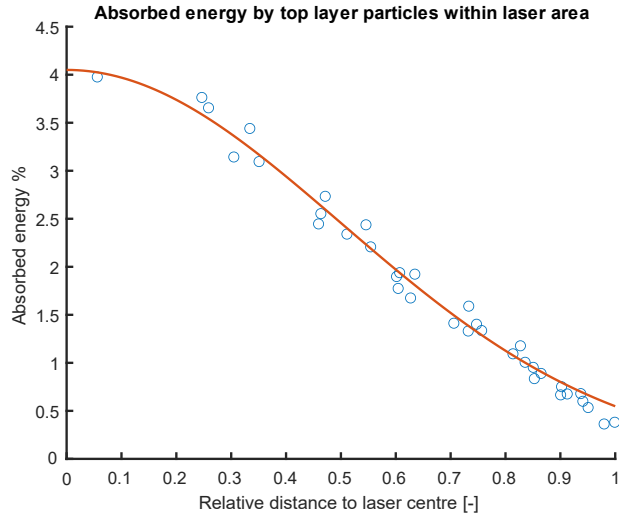
Fig. 19. Absorbed energy per particle vs relative distance to the laser centre, for the top layer particles within the laser area, together with a fitting Gaussian curve.

As seen in Fig. 19, the energy absorption by the particles follows a Gaussian curve quite well. As a base for finding the replacement equations, a fitting Gaussian equation will be found analytically, which uses the inputs mentioned in paragraph 4.2.

The particles in the top layer are fully exposed to the laser, as there are no particles above blocking the path of the laser. Therefore, the amount of absorption by a particle with the top half exposed to the light rays can be calculated. In this section, the amount of energy a particle absorbs will be calculated for these fully-exposed particles. First of all, it will depend on the particle size. The bigger a particle is, the more energy it absorbs. This is because a light ray is absorbed more as it has a longer path in a particle. However, for an infinitely big particle, not everything is absorbed since there will always be some light rays reflected away. This value depends on R according to Eq. (3).

Furthermore, the amount of absorption also depends on how the light rays reflect inside a particle. Fig. 20 shows a circle, representing a particle, with an incoming light ray which has an energy of 1.
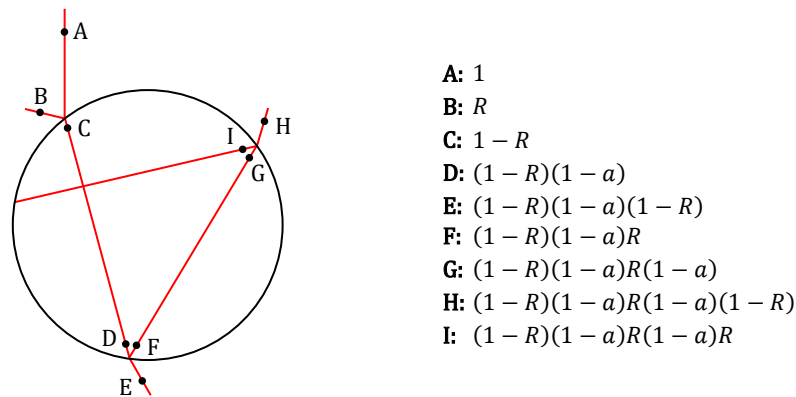

A: 1
B: R
C: $1 - R$
D: $(1 - R)(1 - a)$
E: $(1 - R)(1 - a)(1 - R)$
F: $(1 - R)(1 - a)R$
G: $(1 - R)(1 - a)R(1 - a)$
H: $(1 - R)(1 - a)R(1 - a)(1 - R)$
I: $(1 - R)(1 - a)R(1 - a)R$

Fig. 20. A circle with an incoming light ray which reflects and refracts inside the particle. The energy of the ray is shown at several points with their corresponding values on the right.

The reflected ray (point B) has an energy of R times the incoming light ray, thus $R \cdot 1 = R$. The refracted ray has therefore an energy of $1 - R$. Once inside the particle, the light ray will decrease in energy by a certain factor, depending on the distance travelled and the material's attenuation coefficient μ. For now, this factor, which is the absorbed portion of the energy, will be called a. Therefore, the portion that is left at point D is $1 - a$ times the energy at point C. Thus, $(1 - R)(1 - a)$. Again, the reflected part will be multiplied by R and the refracted part by $1 - R$. This trend can be continued indefinitely, some extra points are shown in Fig. 20.

24

Proof of $R_1 = R_2$

One could notice that the first value R happens on the outside of the particle, and the R for the other reflections on the inside. However, it can be shown that R is equal for both locations. If the incoming ray is considered to be vertical, the incoming angle α_1 can be expressed as a function of the horizontal position with respect to the particle. If r is the position of the incoming ray with $r = 0$ if the line intersects the particle's centre and $r = 1$ if the line is tangent to the particle, as shown in Fig. 21, then α_1 and β_1 can be expressed as:

$$\alpha_1 = \sin^{-1}(r) \qquad \beta_1 = \sin^{-1}(x \sin(\alpha_1)) = \sin^{-1}(xr) \tag{14}$$
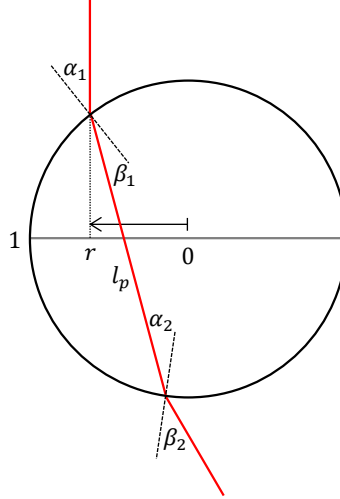
With $x = \frac{n_A}{n_B}$.

Fig. 21. Incoming ray with a horizontal distance r, refracting from outside to inside the particle with angles α_1 and β_1 and from inside to outside the particle with angles α_2 and β_2.

A triangle can be constructed from the incoming intersection point, the outgoing intersection point and the particle centre. This triangle is isosceles since it has two equal sides, the radius of the circle. Following the properties of an isosceles, $\beta_1 = \alpha_2$. Therefore β_2 can be written as:

$$\beta_2 = \sin^{-1}\left(\frac{1}{x}\sin(\alpha_2)\right) = \sin^{-1}\left(\frac{1}{x} \cdot xr\right) = \sin^{-1}(r) \tag{15}$$

The terms in Eq. (3) use the cosines of the angles α and β. Since these angles are expressed above using the inverse sine, the following rule can be used:

$$\cos(\sin^{-1}(A)) = \sqrt{1 - A^2} \tag{16}$$

Which gives the following values:

$$\cos(\alpha_1) = \sqrt{1 - r^2} \quad \cos(\beta_1) = \sqrt{1 - x^2 r^2} \quad \cos(\alpha_2) = \sqrt{1 - x^2 r^2} \quad \cos(\beta_2) = \sqrt{1 - r^2} \tag{17}$$

These square roots will be shortened using the following convention:

$$V_m = \sqrt{1 - x^m r^2} \tag{18}$$

Redefining the values in Eq. (17):

$$\cos(\alpha_1) = V_0 \quad \cos(\beta_1) = V_2 \quad \cos(\alpha_2) = V_2 \quad \cos(\beta_2) = V_0 \tag{19}$$

Now, using Eq. (3), the reflected energy portion factor R for the incoming ray can be written as:

$$R_1 = \frac{1}{2}\left(\left(\frac{n_A \cos\alpha_1 - n_B \cos\beta_1}{n_A \cos\alpha_1 + n_B \cos\beta_1}\right)^2 + \left(\frac{n_B \cos\alpha_1 - n_A \cos\beta_1}{n_B \cos\alpha_1 + n_A \cos\beta_1}\right)^2\right) = \frac{1}{2}\left(\left(\frac{xV_0 - V_2}{xV_0 + V_2}\right)^2 + \left(\frac{V_0 - xV_2}{V_0 + xV_2}\right)^2\right) \tag{20}$$

And R for the ray refracting at the second intersection point:

$$R_2 = \frac{1}{2}\left(\left(\frac{n_B \cos\alpha_2 - n_A \cos\beta_2}{n_B \cos\alpha_2 + n_A \cos\beta_2}\right)^2 + \left(\frac{n_A \cos\alpha_2 - n_B \cos\beta_2}{n_A \cos\alpha_2 + n_B \cos\beta_2}\right)^2\right) = \frac{1}{2}\left(\left(\frac{V_2 - xV_0}{V_2 + xV_0}\right)^2 + \left(\frac{xV_2 - V_0}{xV_2 + V_0}\right)^2\right) \quad (21)$$

The terms inside the square are allowed to be multiplied by -1, therefore the terms in the nominator can be swapped. Also, the terms in the denominator are swapped:

$$R_2 = \frac{1}{2}\left(\left(\frac{xV_0 - V_2}{xV_0 + V_2}\right)^2 + \left(\frac{V_0 - xV_2}{V_0 + xV_2}\right)^2\right) \quad (22)$$

Eq. (22) shows an equation equal to the equation given in Eq. (20). Therefore, $R_1 = R_2$.

Portion of absorbed energy by a particle

Fig. 20 can be used to determine the portion of absorbed energy out of the incoming energy on that particle, E_p. If $E_p = 0.5$, it means that 50% of the energy hitting the particle is being absorbed, the rest is either reflected away at the top or transmitted through the particle. First, the amount of energy of the ray hitting the particle will be set to the dimensionless number 1. The amount of energy that is absorbed between points C and D is a times the value at C, thus $(1-R)a$. Similarly, the amount of energy absorbed between points F and G is a times the value at F, so $(1-R)(1-a)Ra$. Continuing this trend, the total amount of absorbed energy is:

$$\begin{aligned}
E_p &= (1-R)a + (1-R)(1-a)Ra + (1-R)(1-a)R(1-a)Ra + \dots \\
&= (1-R)a \cdot \left(1 + (1-a)R + (1-a)R(1-a)R + \dots\right) \\
&= (1-R)a \cdot \sum_{n=0}^{\infty}\left((1-a)R\right)^n
\end{aligned} \quad (23)$$

This value converges since $(1-a)R < 0$. The summation part can be rewritten in the following way. Here, a general version is considered:

$$\sum_{n=0}^{\infty}(a+b)^n = 1 + (a+b) + (a+b)^2 + (a+b)^3 + \dots \quad (24)$$

Multiplying both sides by $(a+b)$ gives:

$$\begin{aligned}
(a+b) \cdot \sum_{n=0}^{\infty}(a+b)^n &= (a+b) \cdot \left(1 + (a+b) + (a+b)^2 + (a+b)^3 + \dots\right) \\
&= (a+b) + (a+b)^2 + (a+b)^3 + (a+b)^4 + \dots
\end{aligned} \quad (25)$$

Then, subtracting Eq. (25) from Eq. (24):

$$\begin{aligned}
\left(1 - (a+b)\right) \cdot \sum_{n=0}^{\infty}(a+b)^n &= 1 \\
\sum_{n=0}^{\infty}(a+b)^n &= \frac{1}{1-(a+b)}
\end{aligned} \quad (26)$$

Given this definition for $(a+b) < 0$, the summation part in Eq. (23) can be rewritten as:

$$\sum_{n=0}^{\infty}\left((1-a)R\right)^n = \frac{1}{1-(1-a)R} = \frac{1}{1+R(a-1)} \quad (27)$$

Making the total portion of absorbed energy:

$$E_p = (1-R)a \cdot \frac{1}{1+R(a-1)} = \frac{a(1-R)}{1+R(a-1)} \quad (28)$$

26

Here, a is the absorption factor, determining what part of the energy will be absorbed. Eq. (4) shows that the energy will decrease with a factor of $e^{-\mu z}$, therefore the absorption factor is $a = 1 - e^{-\mu z}$. In this situation, the travelled distance z is the length of the light ray inside the particle, l_p. A triangle with all points on the circle can be constructed with sides line l_p, the diameter of the circle D passing through the incoming intersection point, and the line connecting these lines. According to Thales' theorem, this triangle is a right triangle. Therefore, line l can be expressed as:

$$l_p = D \cos(\beta_1) = DV_2 \tag{29}$$

Therefore E_p becomes:

$$E_p(r, x, \mu, D) = \frac{(1 - e^{-\mu DV_2})(1 - R)}{1 + R(1 - e^{-\mu DV_2} - 1)} = \frac{1 - R - e^{-\mu DV_2} + Re^{-\mu DV_2}}{1 - Re^{-\mu DV_2}} \tag{30}$$

Multiplying both sides of the fraction by $e^{\mu DV_2}$:

$$E_p(r, x, \mu, D) = \frac{e^{\mu DV_2} - Re^{\mu DV_2} - 1 + R}{e^{\mu DV_2} - R} = \frac{(1 - e^{\mu DV_2})(1 - R)}{(1 - e^{\mu DV_2}) - (1 - R)} = \frac{1}{\dfrac{1}{1 - R} - \dfrac{1}{1 - e^{\mu DV_2}}} \tag{31}$$

This function depends on four variables: the position where the light ray interacts with the particle (r), the ratio of the refractive indices of the two media (x), the attenuation coefficient of the material (μ) and the diameter of the particle (D). Here, the total amount of absorbed energy for one particle needs to be known. Therefore Eq. (31) needs to be rotated and integrated from 0 to 1 with respect to r. This will create a volume with an average height equal to the absorption factor that needs to be known. However, the average absorption factor for all values of r needs to be known instead of this volume, it therefore needs to be divided by the top surface area, $\pi \cdot 1^2 = \pi$.

$$E_p(x, \mu, D) = \int_0^1 2\pi r \cdot E_p(r, x, \mu, D) \, dr \, / \, \pi = \int_0^1 \frac{2r}{\dfrac{1}{1 - R} - \dfrac{1}{1 - e^{\mu DV_2}}} \, dr \tag{32}$$

Or, fully written out:

$$E_p(x, \mu, D) = \int_0^1 \frac{2r}{1 - \dfrac{1}{2}\left(\left(\dfrac{x\sqrt{1 - r^2} - \sqrt{1 - x^2 r^2}}{x\sqrt{1 - r^2} + \sqrt{1 - x^2 r^2}}\right)^2 + \left(\dfrac{\sqrt{1 - r^2} - x\sqrt{1 - x^2 r^2}}{\sqrt{1 - r^2} + x\sqrt{1 - x^2 r^2}}\right)^2\right) - \dfrac{1}{1 - e^{\mu D\sqrt{1 - x^2 r^2}}}} \, dr \tag{33}$$

This equation describes the portion of absorbed energy out of the incoming energy on that particle.

Trapezoidal integral approximation

To solve this equation, several methods have been tried, such as using the integrate function in MATLAB®, using a fitting sixth-order polynomial, and the trapezoidal method. The trapezoidal method was found to be the most accurate method for its level of preciseness. In this method, a definite integral of a function (or the area below a curve) is approximated by the sum of the areas of many small trapezoids. An example is given in Fig. 22.

Here, the area below a function $y = f(x)$ is divided into n trapezoids. As the total area is from a to b, the width of each trapezoid is $(b - a)/n$ and the heights of the two top points of each trapezoid are equal to the value of the function, so $f(x_{i-1})$ and $f(x_i)$. If $n = \infty$, the sum of the area of the trapezoids is equal to the area below the function from a to b. The integral from a to b can therefore be approximated in the following way:

$$\int_a^b f(x) \, dx \approx \frac{(b - a)}{2n} \sum_{i=1}^{n} \left(f(x_{i-1}) + f(x_i)\right) \tag{34}$$
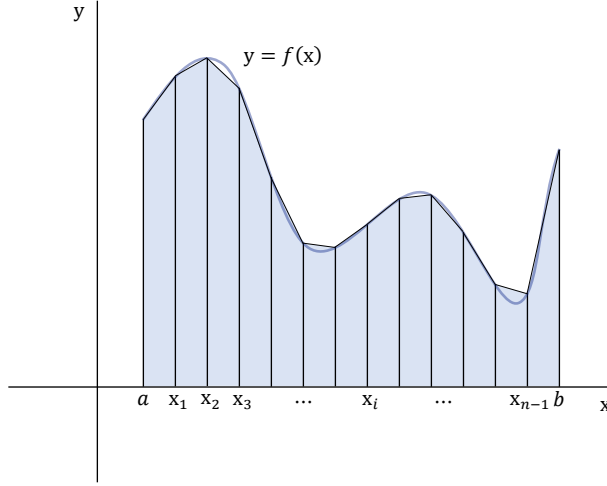
Fig. 22. Approximating the definite integral of a function $y = f(x)$ from a to b by dividing the area below the curve into n trapezoids with a width of $(a - b)/n$ and two heights of $f(x_{i-1})$ and $f(x_i)$.

For the integral in Eq. (33), the lower and upper limits are 0 and 1 respectively. In that situation, $a = 0$ and $b = 1$ in Eq. (34):

$$\int_0^1 f(x)\,dx \approx \frac{1}{2n}\sum_{i=1}^{n}\left(f(x_{i-1}) + f(x_i)\right) =$$

$$\frac{1}{2n}\left(\left(f(0) + f\left(\frac{1}{n}\right)\right) + \left(f\left(\frac{1}{n}\right) + f\left(\frac{2}{n}\right)\right) + \left(f\left(\frac{2}{n}\right) + f\left(\frac{3}{n}\right)\right) + \ldots + \left(f\left(\frac{n-1}{n}\right) + f\left(\frac{n}{n}\right)\right)\right) \quad (35)$$

$$= \frac{1}{2n}\left(f(0) + 2f\left(\frac{1}{n}\right) + 2f\left(\frac{2}{n}\right) + \ldots + 2f\left(\frac{n-1}{n}\right) + f(1)\right) = \frac{1}{n}\sum_{i=1}^{n-1} f\left(\frac{i}{n}\right) + \frac{f(0) + f(1)}{2n}$$

Here, $f(x)$ is the function within the integral in Eq. (33), which can be called $E_p{}'(r)$. For $r = 0$, this results in $E_p{}'(0) = 0$. For $r = 1$, it has the following result:

$$E_p{}'(1) = \cfrac{2 \cdot 1}{\cfrac{1}{1 - \frac{1}{2}\left(\left(\frac{x\sqrt{0} - \sqrt{1-x^2}}{x\sqrt{0} + \sqrt{1-x^2}}\right)^2 + \left(\frac{\sqrt{0} - x\sqrt{1-x^2}}{\sqrt{0} + x\sqrt{1-x^2}}\right)^2\right)} - \cfrac{1}{1 - e^{\mu D\sqrt{1-x^2}}}} =$$

$$\cfrac{2}{\cfrac{1}{1 - \frac{1}{2}\left(\left(\frac{-\sqrt{1-x^2}}{\sqrt{1-x^2}}\right)^2 + \left(\frac{-x\sqrt{1-x^2}}{x\sqrt{1-x^2}}\right)^2\right)} - \cfrac{1}{1 - e^{\mu D\sqrt{1-x^2}}}} = \cfrac{2}{\cfrac{1}{1 - \frac{1}{2}(1 + 1)} - \cfrac{1}{1 - e^{\mu D\sqrt{1-x^2}}}} = \cfrac{2}{\cfrac{1}{0} - \cfrac{1}{1 - e^{\mu D\sqrt{1-x^2}}}} \quad (36)$$

Which has a 1/0 in the denominator, making the whole term equal to 0. Therefore, $E_p{}'(0) = E_p{}'(1) = 0$. This simplifies Eq. (35) in the case for $f(x) = E_p{}'(r)$:

$$E_p(x, \mu, D) = \int_0^1 E_p{}'(r)\,dr = \int_0^1 f(x)\,dx \approx \frac{1}{n}\sum_{i=1}^{n-1} f\left(\frac{i}{n}\right) =$$

$$\sum_{i=1}^{n-1}\cfrac{2i/n}{\cfrac{1}{1 - \frac{1}{2}\left(\left(\frac{x\sqrt{1-(i/n)^2} - \sqrt{1-x^2(i/n)^2}}{x\sqrt{1-(i/n)^2} + \sqrt{1-x^2(i/n)^2}}\right)^2 + \left(\frac{\sqrt{1-(i/n)^2} - x\sqrt{1-x^2(i/n)^2}}{\sqrt{1-(i/n)^2} + x\sqrt{1-x^2(i/n)^2}}\right)^2\right)} - \cfrac{1}{1 - e^{\mu D\sqrt{1-x^2(i/n)^2}}}} \quad (37)$$

Which has a higher accuracy for a larger n. Fig. 23 shows that the higher the n, the closer the amount of absorbed energy is to the values found by the built-in integration function in MATLAB®, indicated by the topmost line. For the rest of the simulation analyses, $n = 500$ was used.
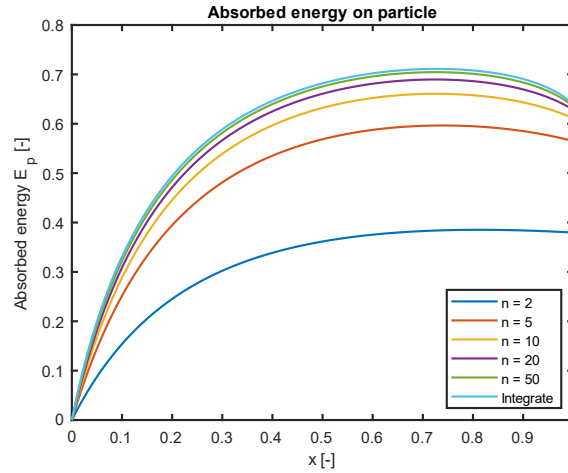
28

Fig. 23. Results of the trapezoidal integral approximation of $E_p(x, \mu, D)$ for several values for n, using $\mu = 27400 \text{ m}^{-1}$ and $D = 60 \text{ μm}$. The light blue line is the result of the built-in integration function in MATLAB®. Here, the refraction index ratio x is plotted against the portion of energy which is absorbed by the particle, out of the total energy hitting that particle.

The result of this trapezoidal integral approximation equation will give E_p, which is the fraction of light being absorbed by the particle, out of the total light hitting that particle, based on the refraction index ratio x, the attenuation coefficient μ and the diameter of the particle D. For the simulation of PS particles with $x = 1/1.5997$, $D = 60 \text{ μm}$ and $\mu = 27400 \text{ m}^{-1}$, Eq. (37) results in $E_p \approx 0.705$. This means that 70.5% of the light that hits a top-layer particle is absorbed.

Total energy received by a particle

The next step is to find an equation for how much energy a particle receives which is fully exposed to the laser on the top side. While this value does depend on the distance from the centre of the laser, it is not simply equal to the value of the Gaussian laser energy at the particle centre times the top surface area of the particle. In 3D, the Gaussian laser energy can be expressed as a revolved Gaussian curve with a volume of 1, as can be seen in Fig. 24. A cylinder, which represents the top view of a particle, is cut out. The volume of this cylindrical cutout is the amount of energy the particle receives, here called E_{in}.
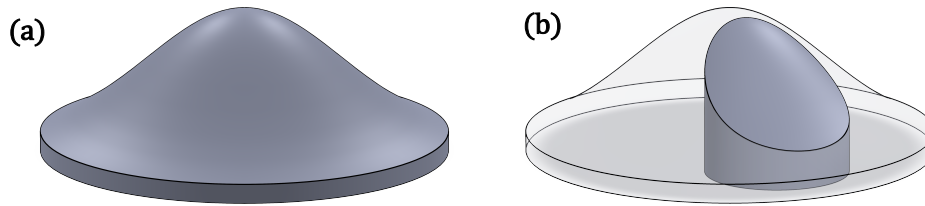

Fig. 24. (a) Revolved Gaussian curve with a volume of 1. (b) Cylindrical cutout with a diameter of D and a volume of E_{in}.

To find an equation for the volume of this cylinder, E_{in}, an integration method can be used. The cylinder can be divided into many thin slices with a thickness of Δd as shown in Fig. 25,
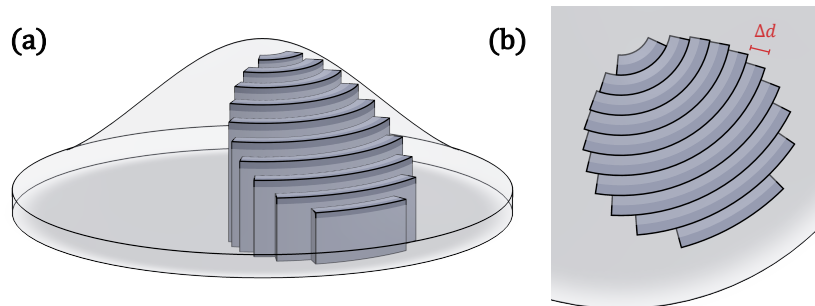

Fig. 25. (a) Discretised cylindrical volume, expressed as many thin slices with a thickness Δd, with (b) the top view.

Each slice is a circular section with its centre at the laser centre. When Δd approaches 0, the sum of the volumes of the slices will be equal to E_{in}. In this case, it can be expressed as the integral of the surface of all slices with respect to the distance from the lase centre to each slice, d_s. The height of each slice is equal to the energy of the laser based on Eq. (11), which depends on the distance from the laser centre, d, and the radius of the laser, r_{laser}. The non-discretised version of this energy can be used since the volume needs to be 1. This equation, Eq. (10), is described in paragraph 3.2 and will be expressed here as $I(d, r_{laser})$. The width of each slice is a circle section with a centre at the laser centre and a radius ranging between $d - D/2$ and $d + D/2$. The length of this circle section, from now on called the width of a slice, can be calculated in the following way:
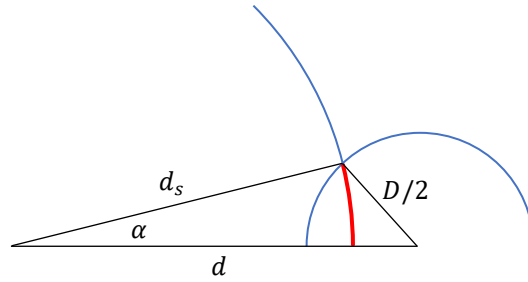

Fig. 26. A triangle constructed by lengths $D/2$, d and the distance from the laser centre to a slice d_s, with angle α at the vertex located at the laser centre. Half the circle section is shown in red.

Fig. 26 shows a top view with a triangle constructed by the particle radius $D/2$, the distance between the laser centre and the particle d, and the distance between the laser centre to a slice d_s. The cosine of the angle α can be calculated using the cosine rule:

$$\cos \alpha = \frac{d_s{}^2 + d^2 - (D/2)^2}{2 \cdot d_s \cdot d} \tag{38}$$

Then, the length of the red line is simply its radius, d_s, times the angle α. Twice this length is equal to the width of a slice:

$$width = 2d_s \cos^{-1}\left(\frac{d_s{}^2 + d^2 - (D/2)^2}{2 \cdot d_s \cdot d}\right) \tag{39}$$

Then finally, the volume of the cylindrical cutout E_{in} is expressed as an integral:

$$E_{in} = \int_{d-D/2}^{d+D/2} (width \cdot height) \, dd_s = \int_{d-D/2}^{d+D/2} I(d, r_{laser}) \cdot 2d_s \cos^{-1}\left(\frac{d_s{}^2 + d^2 - (D/2)^2}{2 \cdot d_s \cdot d}\right) dd_s \tag{40}$$

Or, fully written out:

$$E_{in} = \int_{d-D/2}^{d+D/2} \frac{4d_s}{\pi r_{laser}^2 (1 - e^{-2})} e^{\frac{-2d_s^2}{r_{laser}^2}} \cos^{-1}\left(\frac{d_s{}^2 + d^2 - (D/2)^2}{2 \cdot d_s \cdot d}\right) dd_s \tag{41}$$

In the situation where a particle overlaps with the laser centre, the width of the slice will be a full circle. Eq. (38) takes this situation into account. Namely, applying the numbers for d_s, d and D in this equation will give a number less than -1 in this situation, for which the result of the arccosine will extend in the complex plane. However, its real part will always be equal to π. The width will then become $2 \cdot d_s \cdot \pi$, thus its circumference. In MATLAB®, the function `real()` can be used to acquire the real part of the result of Eq. (41).

The last step is to redefine the range of the integral in this situation and similarly for the situation where the particle is partially or fully outside the laser area. When the particle overlaps the centre of the laser, the range should be $[0 \quad d+D/2]$. If the particle is partially outside the laser area, the range should be $[d-D/2 \quad r_{laser}]$. Therefore, the lower boundary is equal to the maximum of $d - D/2$ and 0, the upper boundary is equal to the minimum of $d + D/2$ and r_{laser}:

$$E_{in} = \int_{\max(d-D/2,\,0)}^{\min(d+D/2,\,r_{laser})} \frac{4d_s}{\pi r_{laser}^2(1-e^{-2})} e^{\frac{-2d_s^2}{r_{laser}^2}} \cdot \texttt{real}\left(\cos^{-1}\left(\frac{d_s^2 + d^2 - (D/2)^2}{2 \cdot d_s \cdot d}\right)\right) dd_s \quad (42)$$

Similar to Eq. (33), this equation cannot be solved where d_s is integrated out of the equation. Therefore, also for this equation, the trapezoidal integral approximation will be used to solve it. Eq. (35) before showed the following simplification, here the version with boundaries a and b is used:

$$\int_a^b f(x)\, dx \approx \frac{b-a}{n} \sum_{i=1}^{n-1} f\left(a \cdot \left(1 - \frac{i}{n}\right) + b \cdot \frac{i}{n}\right) + \frac{f(a) + f(b)}{2n} \quad (43)$$

$$\text{with } a = \max(d - D/2, 0) \quad \text{and} \quad b = \min(d + D/2, r_{laser})$$

Again, when looking at the parts in the nominator of the last fraction, $f(\max(d - D/2, 0))$ and $f(\min(d + D/2, 0))$, it can be concluded that these are both equal to 0. Namely, these locations are at the most inner and outer slices as shown in Fig. 25, which have a width approaching 0 for a high number for n. Eq. (43) can therefore be simplified to:

$$E_{in}(d, D, r_{laser}) = \int_a^b E_{in}'(d_s)\, dd_s \approx \frac{b-a}{n} \sum_{i=1}^{n-1} f\left(a \cdot \left(1 - \frac{i}{n}\right) + b \cdot \frac{i}{n}\right)$$

$$\text{with } E_{in}'(d_s) = \frac{4d_s}{\pi r_{laser}^2(1-e^{-2})} e^{\frac{-2d_s^2}{r_{laser}^2}} \cdot \texttt{real}\left(\cos^{-1}\left(\frac{d_s^2 + d^2 - (D/2)^2}{2 \cdot d_s \cdot d}\right)\right), \quad (44)$$

$$a = \max(d - D/2, 0) \quad \text{and} \quad b = \min(d + D/2, r_{laser})$$

For several distances between the laser centre and the particle, d, the amount of energy on a particle out of the total laser energy E_{in} will have the following curve using Eq. (44) as shown in Fig. 27:
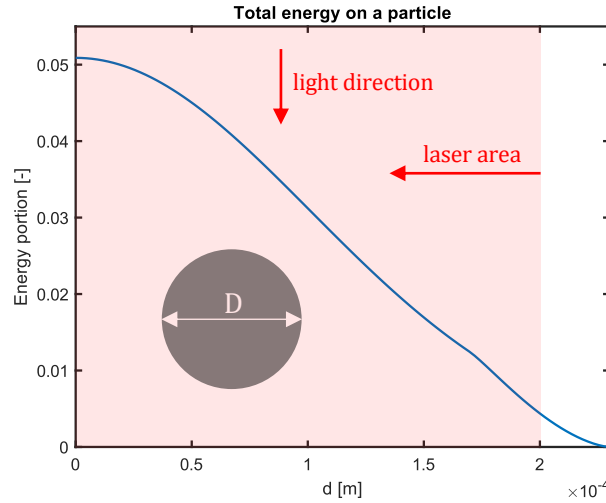

Fig. 27. Total energy on a particle out of total laser energy (E_{in}), depending on the distance from the particle centre to the laser centre (d), with $r_{laser} = 200$ μm and $D = 60$ μm.

This curve is the result for a laser radius of $r_{laser} = 200$ μm and a particle diameter of $D = 60$ μm. From the graph can be seen that for a particle and laser with these dimensions, the particle will receive about 5% of the total laser light if the particle is located at the centre of the laser. If the particle is fully outside the laser area, at $r_{laser} + D/2$, the particle will receive no laser energy.

For this trapezoidal integral approximation, the number of slices n can be relatively low, with an exception for the case of $d = 0$ μm. Fig. 28 shows the values for the energy portion on a particle for $d = 0$ μm, for several values for the number of slices n:
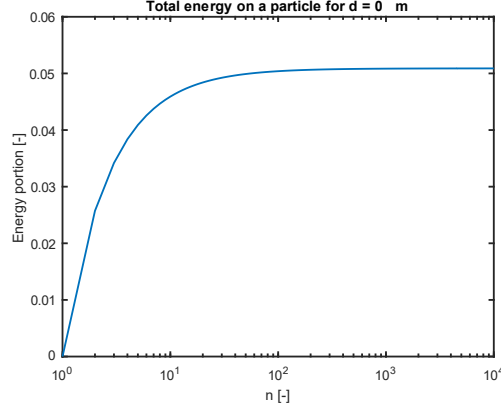
Fig. 28. Total energy on a particle out of total laser energy E_{in} depending on the number of slices n, with $r_{laser} = 200$ μm, $D = 60$ μm and $d = 0$ μm.

At $n = 1000$, the value for the total energy on a particle is already at 99.9% of the actual value of around 5%. This calculation only takes about 1-2 ms and is only executed once per time step for the top-layer particles within the laser area. Therefore, $n = 1000$ will be used.

Resulting energy absorption for the top layer

For any particle in the top layer, the following values are now known:

- E_{in}: the amount of energy the particle receives based on the distance to the laser d, the diameter D and the laser radius r_{laser} according to Eq. (44)
- E_p: the portion of this energy the particle absorbs based on the refraction index ratio x, the attenuation coefficient μ and the diameter D according to Eq. (37)

These numbers can be multiplied to achieve the amount of absorbed energy per particle, out of the total incoming laser energy:

$$E_{abs}(d, D, r_{laser}, x, \mu) = E_{in}(d, D, r_{laser}) \cdot E_p(x, \mu, D) \tag{45}$$

This result is used in Eq. (12) to determine the temperature increment in MercuryDPM. The values for E_{abs} were shown in Fig. 19 based on the ray tracing simulations, and can now be calculated. Fig. 29 shows the results of the ray tracing simulations, together with the analytical equation with the same parameters filled: $D = 60$ μm, $r_{laser} = 200$ μm, $x = 1/1.5997$ and $\mu = 27400$ m^{-1}.
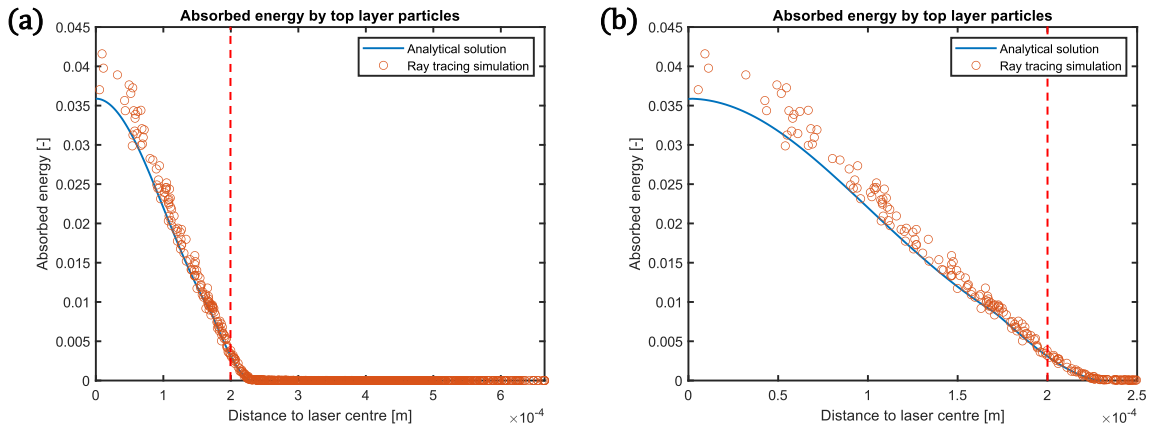

Fig. 29. Analytical solution (Eq. (45)) for the amount of absorbed energy of the top layer particles out of total laser energy E_{abs}, together with the results of four combined ray tracing simulations, (a) for the total bed and (b) within the laser area. The red dashed line indicates the edge of the laser area.

As can be seen in Fig. 29 (a), the analytical value is indeed 0 outside the laser area. In (b), the shape of the line is also in accordance with the extra descending curve around the edge of the

laser, so between $d = 1.7 \cdot 10^{-4}$ m and $d = 2.3 \cdot 10^{-4}$ m. However, a general deviation of about −9% from the ray tracing simulation can be seen for every value for d.

This deviation can be explained due to certain rays being neglected from being absorbed. Eq. (44) assumes that all rays reflecting away from the top layer, are not part of the absorbed energy portion. This is mainly true, however, a part of the reflected rays does end up being absorbed by neighbouring particles. An illustration of this can be seen in Fig. 30.
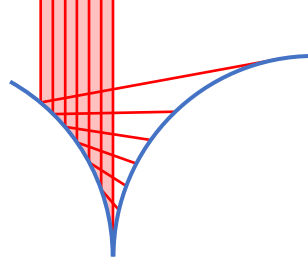

Fig. 30. Section of light rays which reflect to the neighbouring particle.

The incoming light rays splits and partially transmits into the left particle and partially reflects to the particle adjacent to it. The amount of light which is reflected from this area could potentially be calculated, however, the amount which is actually absorbed by the neighbouring particle depends on the position of this particle. Namely, not all neighbouring particles are directly adjacent to the first particle. This problem is case specific for every particle bed, as it depends on the position of all the neighbouring particles of any particle. Therefore, no equation or other approximation is used to solve this problem of rays reflecting to neighbouring particles. This could be improved in further studies.

A general correction factor on the total amount of absorbed energy will be used to compensate for the neglect of some rays being absorbed. Since the neglected rays are always the rays reflecting away from the particles, which energy portions R do not depend on the attenuation coefficient of the material, it is assumed that this correction factor does not depend on μ. It is also assumed that the factor does not on the particle diameter, since a larger particle only scales everything in space but keeps the portion of rays reflecting to the neighbouring particles the same. The correction factor will be referred to as K_{cor}.

Based on the data shown in Fig. 29, the coefficient of determination, or R^2, of the top layer for the whole bed (a) is $R^2 = 0.98725$, and for $d < r_{laser} + D/2$ (b) then $R^2 = 0.97108$. If $K_{cor} = 1.09937$, the value for which the analytical line has the best fit, then the R^2 values for the bed and inside the laser area change to 0.99646 and 0.99199 respectively. This gives the curve in Fig. 31.
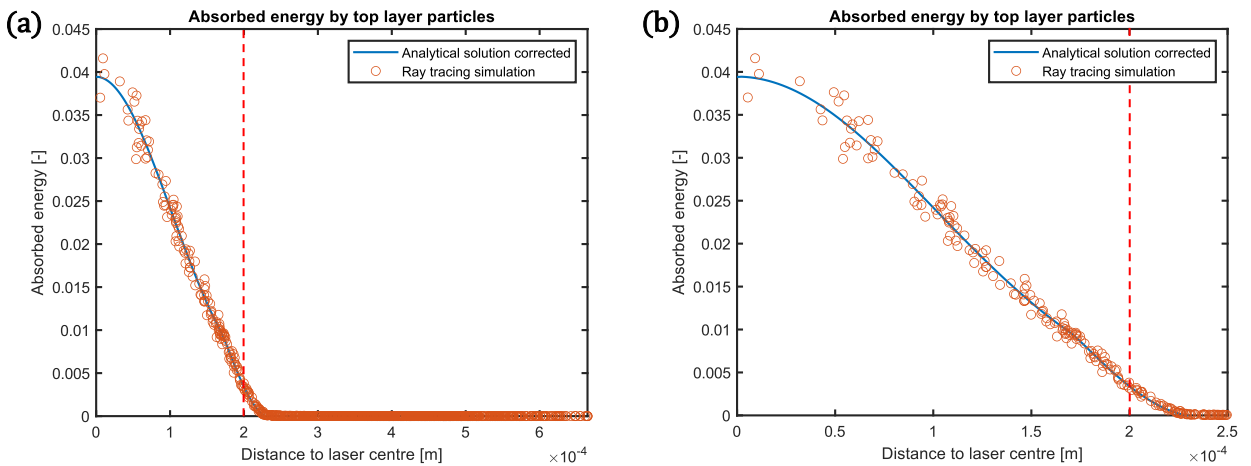

Fig. 31. Amount of absorbed energy E_{abs} for (a) the whole bed and (b) within the laser area, with a corrected analytical solution.

Now that the correction factor K_{cor} is included in the graph, the curve of the analytical solution nicely follows the ray tracing simulation results, again including the kink at $d = r_{laser} - D/2$. The reached coefficient of determination of 0.996 in combination with the good fit shows that the amount of absorbed energy for the top layer particles in a monodisperse bed can now be calculated, which is a significant decrease in calculation time compared to performing the ray tracing simulations.

4.2.2   Energy absorption within the particle bed

The next step is to calculate the amount of absorbed energy for the rest of the particle bed E, below the top layer. Fig. 32 (a) and (b) show the amount of absorbed energy from the ray tracing simulations for four different particle beds combined, which have the same number of particles, particle size and bed dimension. The results are from the same simulation shown in Fig. 10. Here, the vertical axis shows the propagated distance z rather than the height in the bed Z. It is also flipped such that the particles in the top layer are at the top of the graph. Note that the horizontal axis does not represent a dimension of the bed, but the perpendicular distance to the laser centre. Both a linear and a logarithmic colour scale are shown, with a more red colour indicating a higher energy absorption. The value for the amount of absorbed energy is the fraction of the total laser energy. Therefore, all values added together in these graphs will result in 4, since four particle beds are combined here.
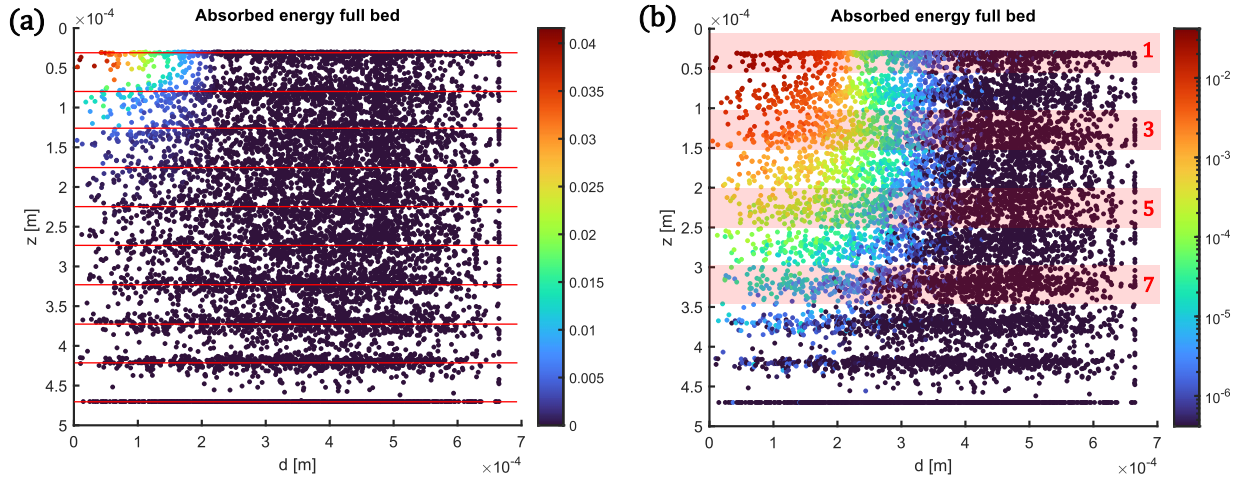

Fig. 32. Particle beds from four ray tracing simulations combined, showing the amount of absorbed energy out of the total laser energy E with (a) a linear colour scale and (b) a logarithmic colour scale. Each dot represents the location of the centre of one particle. Furthermore, (a) shows the centre of ten distinguishable layers, (b) shows the regions of layer 1, 3, 5 and 7.

The colour scales clearly show that the particles closer to the laser centre and closer to the surface of the bed, have a higher amount of absorbed energy. From Fig. 32 (a) the effect of the radius of the laser, r_{laser}, is also visible, which ends around $d = 200$ µm. As shown in Eq. (4), the light energy decreases exponentially in the direction of propagation. Therefore, also the amount of absorbed energy per particle is assumed to decrease exponentially. The results of Eq. (45) can therefore be multiplied by $e^{-\mu z}$ to see the effect of the propagation depth within the bed. The last thing to consider is the fact that the particle bed is not solid, and the regions where there are no particles do not cause the light to decrease in energy. If the volume fraction $\varphi = 0.6$, then only in 60% of the propagated distance the light energy will decrease. Therefore z needs to be multiplied by φ: $e^{-\mu z \varphi}$. This creates the following colour graph in Fig. 33.

Note that in Fig. 33, the propagated distance z starts at $D/2$ and ends at $Z - D/2$ with Z the bed height. However, for the equations, a range of $0 < z < Z - D$ is used. This is done because the particles at the top layer receive light with a propagated distance of 0, but for a good comparison with Fig. 32, the graph is placed $D/2$ lower. This way, each coloured pixel represents the location of the centre of each particle, similar to Fig. 32.
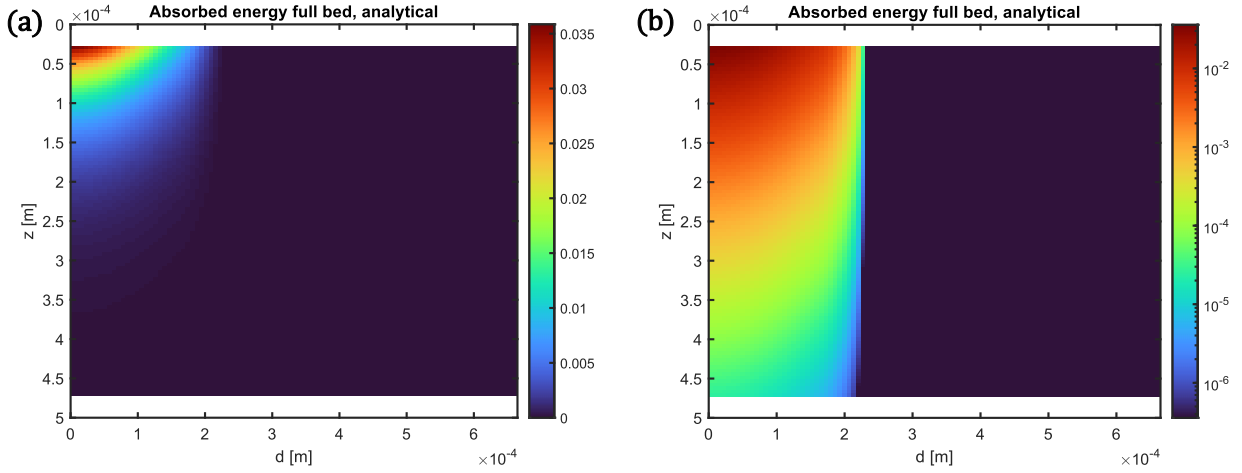
Fig. 33. The result of Eq. (45) multiplied by $e^{-\mu z \varphi}$ showing the absorbed energy based on the perpendicular distance to the laser centre d and the propagated depth z out of the total incoming laser energy with (a) a linear colour scale and (b) a logarithmic colour scale. Here, $\theta = 0°$, $D = 60$ μm, $r_{laser} = 200$ μm, $x = 1/1.5997$, $\mu = 27400\ m^{-1}$ and $\varphi = 0.6$.

A comparison between Fig. 33 and Fig. 32 shows that the amount of absorption does not match perfectly, especially on the logarithmic colour scale. To have a better comparison, the bed height will be divided into several layers such that each layer can be analysed individually. In Fig. 32 (a), ten layers are roughly visible, which are indicated by the red lines, representing the centre of each layer. The height of these layers is $(Z - D)/9 = 48.\overline{8}$ μm which is $\pm81.5\%$ of the particle diameter. This appears to correspond to the layer height of a hexagonal close sphere packing (HCP), which is $\sqrt{6}/3 \approx 0.816$ of the sphere diameter. This is an indication that the particles are closely packed.
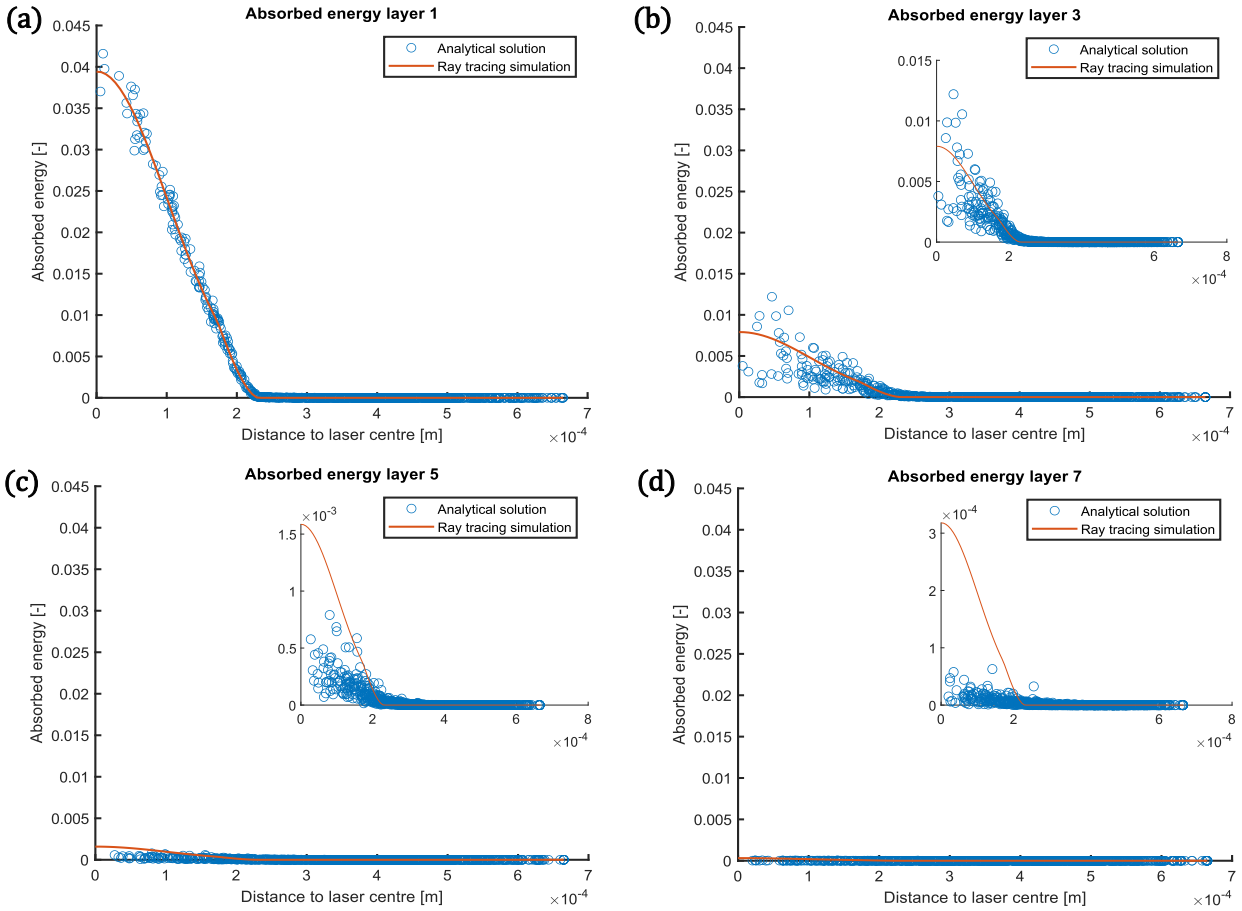

Fig. 34. The result of Eq. (45) multiplied by $e^{-\mu z \varphi}$ and the ray tracing simulation showing the absorbed energy E for (a) layer 1, (b) layer 3, (c) layer 5 and (d) layer 7 with equal axes. For visibility, an extra graph with a different scale is shown.

35

Fig. 34 shows graphs for four different layers, which illustrates the amount of absorption based on the ray tracing simulations compared to the analytical solution. Here, layer number 1, 3, 5 and 7 are shown, with layer 1 being the top layer. Fig. 32 (b) shows these four layers, with the centre of the particles laying in the indicated shaded area of each layer. The axes being equal shows the decrease of the absorbed energy for a higher layer number. Furthermore, here it is better visible that the analytical solution does not perfectly correspond to the results of the ray tracing simulations. The reason for this is that in the ray tracing simulations, the light rays scatter in all directions when interacting with the particles. As the light rays are being absorbed by the surrounding particles, therefore also the particles left and right of each particle, the amount of absorption per layer is more spread out across the layer. This can also be seen by the fact that for the lower layers, the absorption has a higher variance due to this random scattering. It can be seen that this effect is bigger at lower layers, however, the absorption is already low at these layers. The effect of this scattering is therefore minimal on the total amount of absorption. For this reason, a simple method will be used to correct this phenomenon, such that the analytical solution corresponds better to the amount of absorption for the lower layers. Before, the effect of the propagated depth z is calculated by multiplying the absorption of the top layer by $e^{-\mu z \varphi}$. Now, two new factors will be introduced which will affect the dimensionless part μz. Namely, μz will be replaced by $A(\mu z)^B$. These factors A and B were acquired by trying values until the best solution was found.

The combination of $A = 0.85$ and $B = 1.28$ showed results with the best fit, thus the absorption of the top layer will be multiplied by $e^{-A(\mu z)^B \varphi} = e^{-0.85(\mu z)^{1.28} \varphi}$. Fig. 35 shows the corrected analytical solution for layers 3, 5, 7 and 9. This time, a good fit for every layer is obtained.
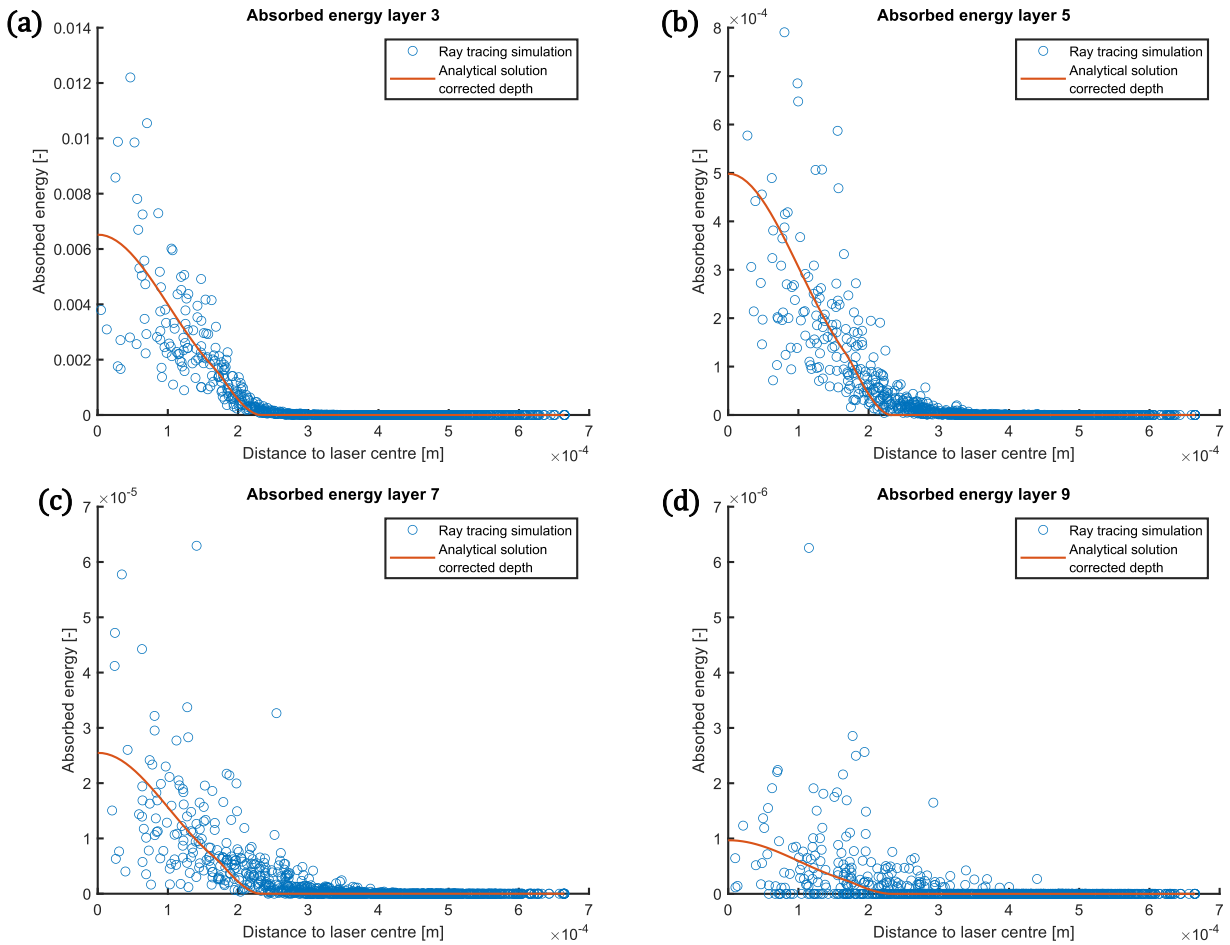

Fig. 35. Analytical solution (Eq. (45)) with corrected depth and ray tracing simulation showing the absorbed energy E for (a) layer 3, (b) layer 5, (c) layer 7 and (d) layer 9. No fixed scale is used to show the new fitting analytical solution.

4.2.3 Changing simulation variables

In this paragraph, several variables in the ray tracing simulations will be changed and their effects will be analysed, to see whether the analytical solution still fits the data from the simulations. These effects are the volume fraction, particle size, laser angle and refraction index ratio.

Effect of volume fraction

The current analytical solution for the amount of absorbed energy for a monodisperse particle bed takes into account the volume fraction. However, the ray tracing simulations used as a base for the analytical solution only have a volume fraction of $\varphi = 0.6$. To see whether the analytical solution has a good fit for other volume fractions, more ray tracing simulations have been conducted. As mentioned in section 3.2, the volume fraction is physically limited to a certain range. On the lower end, the volume fraction is limited by gravity as the particles fall down and reach a certain natural volume fraction. In MercuryDPM, the particles can be flattened and compacted to reach a higher volume fraction. The minimum found volume fraction, which has a flattened top surface but is not further compacted, is around $\varphi = 0.57$. On the higher end, the volume fraction is limited by the maximum possible sphere packing. Namely, HCP has a volume fraction of $\pi/(3\sqrt{2}) \approx 0.7405$. Assuming that the particles do not overlap during compacting, this is the highest reachable value. However, during compacting, it appeared that the particles did start to overlap slightly when this value was approached. The volume fractions used will therefore be kept not higher than 0.7.

Six different volume fractions were chosen: 0.575, 0.6, 0.625, 0.65, 0.675 and 0.7. For each volume fraction, four simulations were performed for monodisperse beds with a particle diameter of 60 µm. Fig. 36 shows the energy absorption for the first layer of these four combined simulations, per volume fraction. The number of particles per volume fraction is chosen such that the volume fraction is as close as possible to the set value, however, the particles appeared to slightly overlap with the bed boundaries. Since the volume of the bed is calculated using the position of the outermost particles, it becomes larger than the original 1 x 1 x 0.5 mm, lowering the volume fraction. The figure titles show the resulting volume fractions, which are used in the equations.
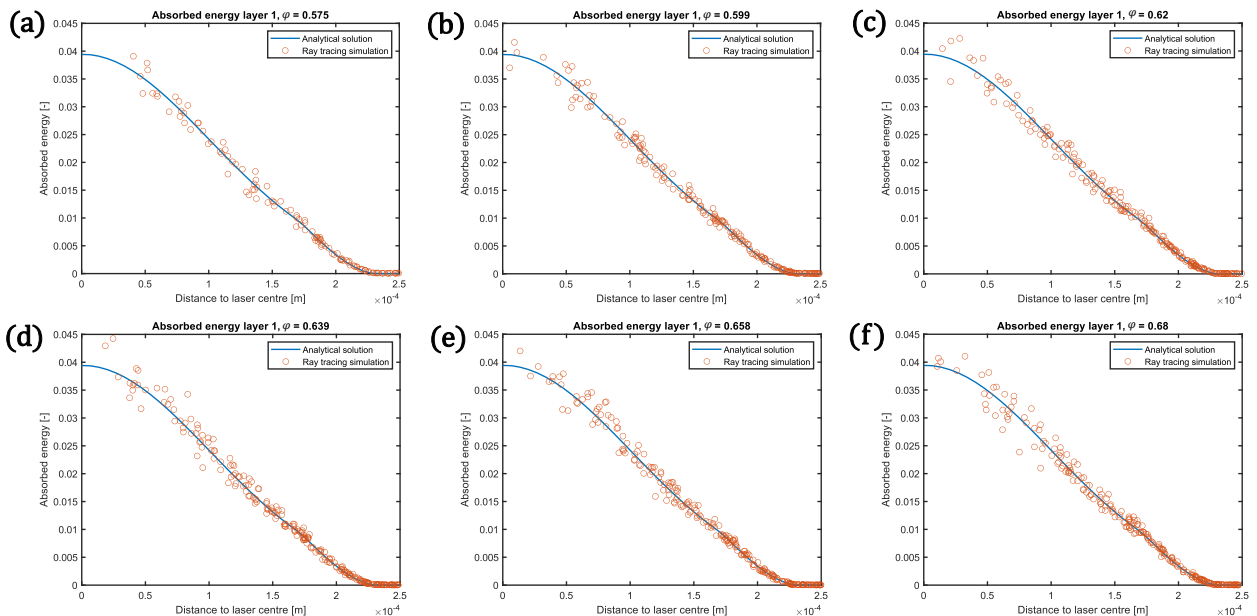

Fig. 36. Analytical solution (Eq. (45)) and ray tracing simulations showing the absorbed energy for layer 1, with intended volume fractions of (a) 0.575, (b) 0.6, (c) 0.625, (d) 0.65, (e) 0.675 and (f) 0.7. Here, $D = 60$ µm and $r_{laser} = 200$ µm.

As visualised in Fig. 36, the amount of absorption does not vary for different volume fractions. More particles blocking the laser light, which is the case for a higher volume fraction, will result in less absorption of particles in a lower layer. Since this does not influence the first layer, the amount of absorption for the first layer is independent of the volume fraction.

To see whether the current use of φ in the analytical equation is correct, a new visualisation method of the absorbed energy will be introduced. Instead of showing the absorption for every particle per layer per volume fraction in a graph, a single value will be given per layer per volume fraction: E_{peak}. This number is an estimation for the peak value of the Gaussian-shaped fitting curve, which is at the centre of the laser. For example, Fig. 36 shows that this value for the first layer, where $z = 0$, is equal to $E_{peak} = 0.039$ for every volume fraction. These values can be plotted against the propagated distance z for every volume fraction. Fig. 37 (a) shows these estimated values E_{peak}, and (b) shows the values using the current analytical result in. The circles show the location of the numbered layers.
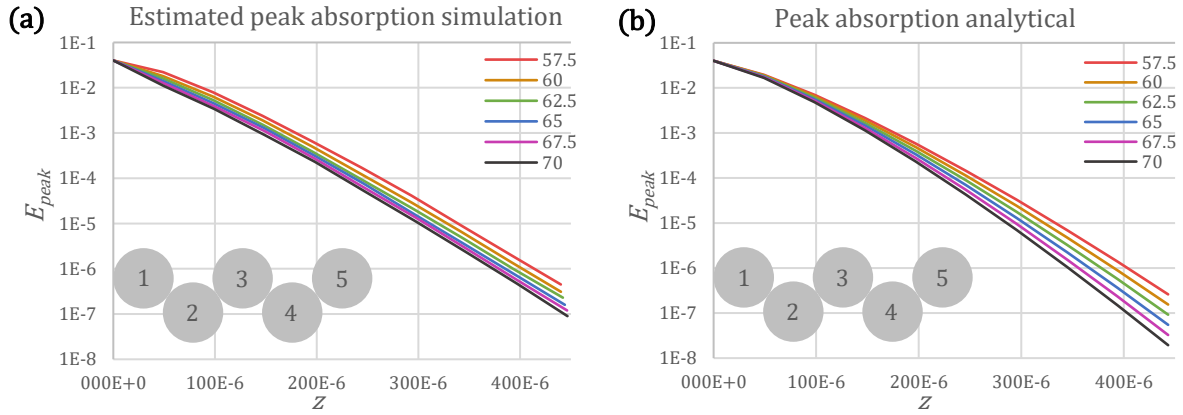
(a)

(b)

Fig. 37. (a) Estimated peak absorption values for several volume fractions as a function of propagated distance from the ray tracing simulations and (b) the peak absorption values using the current analytical solution.

The current analytical result does not correspond perfectly with the ray tracing simulation results. Similarly to the effect of the propagation depth, a new equation will be formulated for the effect of the volume fraction. Currently, the absorption of the top layer is multiplied by an equation in the form of $e^{-A(\mu z)^B \varphi}$. To account for the fact that the lines in Fig. 37 (a) are parallel with each other instead of diverging, a number in the form of $C(\mu z)^E \varphi$ will be subtracted in the power. Then, to make it have an effect starting from the lowest volume fraction, φ will be replaced by $(\varphi - 0.574)$. Lastly, the lines for a higher φ are closer together, meaning this effect should be smaller for a higher φ. Therefore, it will be raised to a power smaller than 1: $(\varphi - 0.574)^F$. Thus, $e^{-A(\mu z)^B \varphi}$ will be replaced by $e^{-A(\mu z)^B - C(\mu z)^E \cdot (\varphi - 0.574)^F}$.

It was found that the combination of $A = 0.39$, $B = 1.4$, $C = 3.8$, $E = 0.3$ and $F = 0.8$ showed a good fit for all volume fractions. Therefore, the absorption of the top layer will be multiplied by $e^{-0.39(\mu z)^{1.4} - 3.8(\mu z)^{0.3} \cdot (\varphi - 0.574)^{0.8}}$. Fig. 38 shows E_{peak} using this new equation.
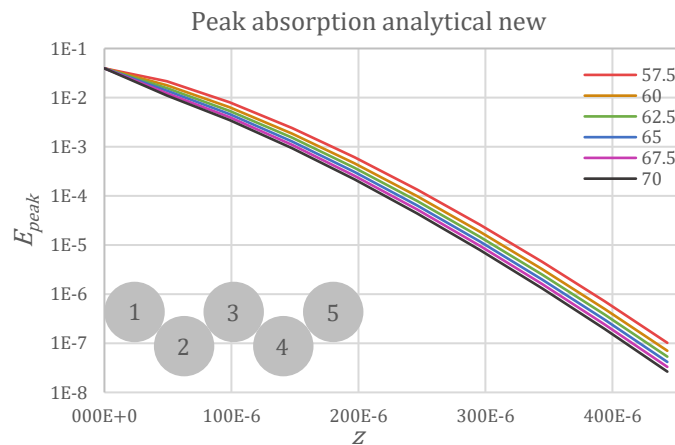

Fig. 38. Peak absorption as a function of propagated distance using the new analytical solution for several volume fractions.

The new equation aligns very well with the estimated peak values of the simulations for the top layers. For the lower layers, the new equation does deviate, however, the amount of absorption in these layers is low and therefore less significant for the total absorption. Table 2 shows a better comparison between the estimated peak values of the simulation and the new equation for the first five layers.

layer	0.575		0.6		0.625		0.65		0.675		0.7		power
	Sim.	Ana.	Sim.	Ana.	Sim.	Ana.	Sim.	Ana.	Sim.	Ana.	Sim.	Ana.	
1	3.9	3.94	3.9	3.94	3.9	3.94	3.9	3.94	3.9	3.94	3.9	3.94	-2
2	2.2	2.16	1.8	1.76	1.6	1.53	1.4	1.36	1.2	1.22	1.1	1.08	-2
3	8	8.23	6.4	6.38	5.3	5.37	4.5	4.61	3.9	4.00	3.4	3.45	-3
4	24	25.1	19	18.8	15	15.4	13	12.9	11	10.9	9	9.22	-4
5	6.5	6.46	5	4.72	3.8	3.76	3.2	3.08	2.7	2.55	2.3	2.12	-4

Table 2. Comparison between the peak values E_{peak} from the simulations and the analytical solution, for several volume fractions for the top five layers. The last column shows the exponent with base 10 the numbers should be multiplied by.

In Fig. 39, the new equation is again plotted with the simulation results for the rest of the bed, which shows that the equation now corresponds well with the simulations.
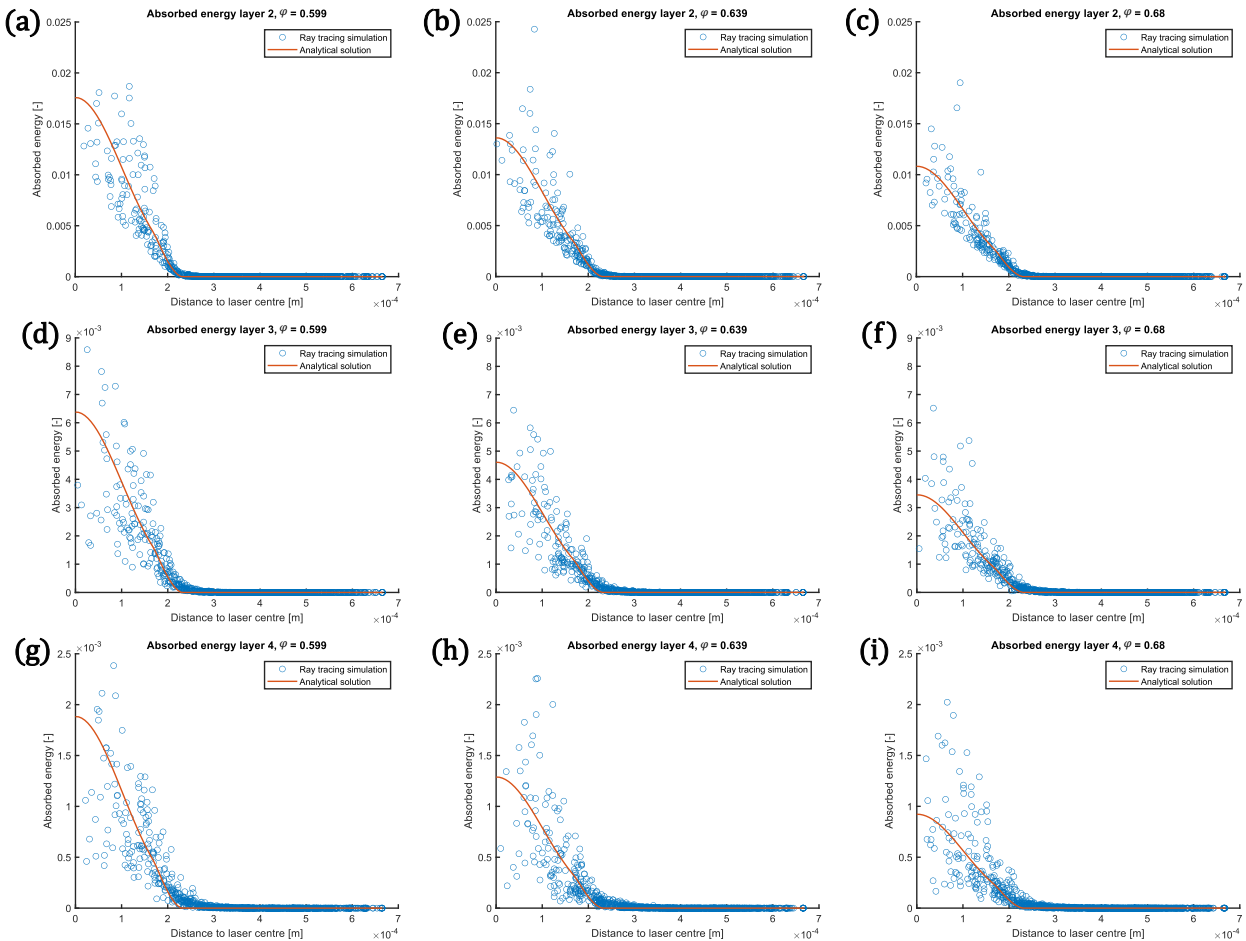

Fig. 39. New analytical solution with ray tracing simulation results showing the absorbed energy E for several layers and intended volume fractions. With (a) layer 2 & $\varphi = 0.6$, (b) layer 2 & $\varphi = 0.65$, (c) layer 2 & $\varphi = 0.7$, (d) layer 3 & $\varphi = 0.6$, (e) layer 3 & $\varphi = 0.65$, (f) layer 3 & $\varphi = 0.7$, (g) layer 4 & $\varphi = 0.6$, (h) layer 4 & $\varphi = 0.65$ and (i) layer 4 & $\varphi = 0.7$.

So far, the height of the bed has been divided into separate layers. Furthermore, the analytical equation was constructed to fit the data from the ray tracing simulations results for every individual layer. This led to the fact that all the particles in the top layer follow an analytical function which uses a propagation depth of $z = 0$ μm. This is a good assumption, as the particles

in the top layer are exposed to the air and therefore should not have a lower absorption due to the exponential decrease of the absorption within the bed. However, Fig. 40 shows that the particles in the top layer do not exactly have an equal Z coordinate. The compression code in MercuryDPM forces the particles downwards using a slowly descending lid. During this, the particles have a small movement which results in deviations in the final height between the top particles when the code stops running.
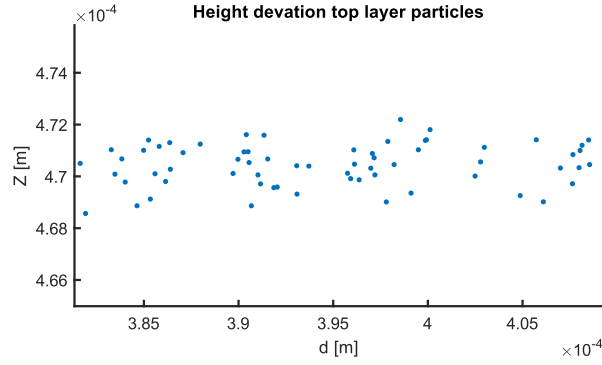

Fig. 40. Dots representing the centre of the particles in the top layer, showing a deviation in the height.

The Z coordinates of the particles in the top layer are around 470 µm, which is the total bed height minus $D/2$, but deviate approximately 4 µm from each other at maximum. According to the equation shown above, which multiplies the absorption of the top layer by $e^{-0.39(\mu z)^{1.4}-3.8(\mu z)^{0.3}\cdot(\varphi-0.574)^{0.8}}$, a vertical distance of 4 µm would already result in an absorption reduction by a factor of 0.709. This is an incorrect conclusion since all the particles in the top layer have no particles above them and should all experience a propagation depth of 0 µm. For this reason, not the propagated depth of a particle within the bed will be used in this equation, but the depth of the layer it is inside. For a monodisperse bed, it was already observed that the particles will naturally form layers which have a layer height of $\sqrt{6}/3$ of the particle diameter. To have a consistent expected number of layers in a particle bed, the bed height should follow the following equation:

$$Z = \left(N_{layer} - 1\right) \cdot D \cdot \sqrt{6}/3 + D \tag{46}$$

With Z the bed height in m and N_{layer} the desired number of layers. For example, a bed with 10 layers and a particle diameter of $D = 60$ µm will have nine spaces between the layers with a height of $60 \cdot \sqrt{6}/3 \approx 49$ µm, and half the diameter below the centre of the bottom layer and above the centre of the top layers. This results in a required bed height of $9 \cdot 49 + 60 \approx 501$ µm.

The propagated distance z of every layer is according to the following equation:

$$z = (i - 1) \cdot D \cdot \sqrt{6}/3 \tag{47}$$

With i the layer number, ranging from 1 to N_{layer}.

For the current simulations, which are for a monodisperse particle bed with a particle diameter of $D = 60$ µm and volume fractions of 0.575, 0.6, 0.625, 0.65, 0.675 and 0.7 with four simulations per volume fraction, a R^2 value can be calculated. In Table 3, these values are given. Each value is the average of the four simulations and uses the depth of the layer a particle is in, instead of the depth of the particle itself, as mentioned above.

φ	57.5	60	62.5	65	67.5	70	average
R^2	0.9034	0.9628	0.9708	0.9757	0.9751	0.9839	**0.9619**

Table 3. Coefficient of determination of the analytical equation compared to the simulations for several volume fractions, together with the average.

Overall, the R^2 value is high, which is to be expected based on the good fitting curve in Fig. 39. The R^2 value for a volume fraction of $\varphi = 0.575$ seems to be deviating from the other volume fractions, this can be explained by the fact that the phenomenon of layers forming due to compression is less distinct for this low volume fraction. This means that the particles in the top layers are less aligned in one plane, causing the absorption to deviate more from the fitting curve. However, in practice, such a low volume fraction can only be acquired if the top layer is not compressed. If this volume fraction is excluded, the average will increase to $R^2 = 0.9736$.

Effect of particle size

To simulate the effect of the particle size, two different methods can be used. The first method is to generate a new bed with particles with a different size. The second method is to scale the attenuation coefficient μ, together with the laser radius r_{laser} inversely. Namely, if the attenuation coefficient is increased, the light is absorbed more inside one particle, which also occurs if the diameter of the particles is increased. These values are linearly proportional. Therefore, if the attenuation coefficient is increased by a factor of 2, it will have the same effect as increasing the particle diameter by a factor of 2. Consequently, the particle radius needs to be decreased by a factor of 2 since a larger particle diameter results in fewer particles fitting within the laser area if r_{laser} is kept constant.

For the second method, no new particle bed needs to be generated. This method will therefore be used. Previously, the particle bed used had 2653 particles with a diameter of $D = 60$ μm in a bed of 1 x 1 x 0.5 mm, and therefore a volume fraction of $\varphi = 0.6$. For this, a laser radius of $r_{laser} = 200$ μm and an attenuation coefficient of $\mu = 27400$ m^{-1} was used. If a dimensional scaling factor (SF) of 2 is used, this bed will be treated as a bed of 0.5 x 0.5 x 0.25 mm with particles with a diameter of $D = 120$ μm. This is achieved by setting the laser radius to $r_{laser} = 100$ μm and the attenuation coefficient to $\mu = 54800$ m^{-1} and keeping the bed dimensions unchanged. To analyse the effect of the particle size, the following scaling factors will be used: 0.5, 2/3, 1.5 and 2. Table 4 shows the variable values for these scaling factors, together with the original scaling factor of 1.

Scaling factor	μ [m^{-1}]	r_{laser} [μm]	Mimicking a D of [μm]
0.5	13700	400	30
2/3	18266.$\overline{6}$	300	40
1	27400	200	60
1.5	41100	133.$\overline{3}$	90
2	54800	100	120

Table 4. Scaling factors that are used to mimic different particle sizes.

Again, for each scaling factor, four particle beds with the same properties were simulated. All simulations were done for a particle bed with a volume fraction of $\varphi = 0.6$. Fig. 41 shows the simulation results, with the absorbed energy for layers 1, 3 and 5 for each of the scaling factors.
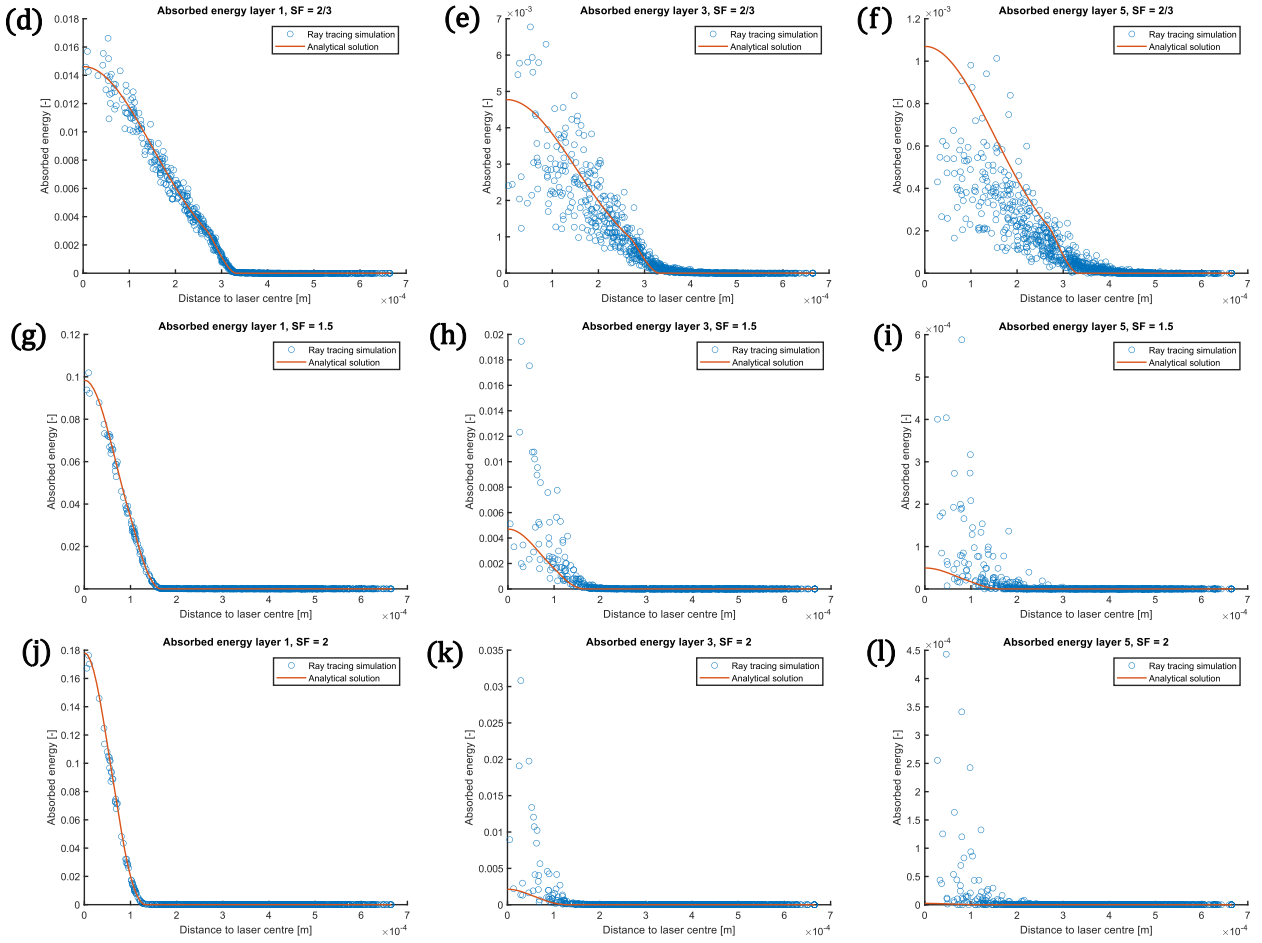
(a)

(b)

(c)
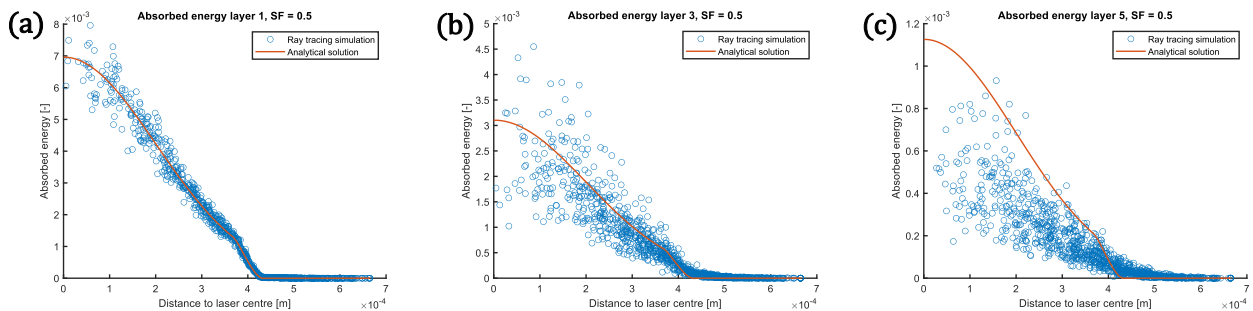
Fig. 41. Analytical solution with ray tracing simulations for layers 1, 3 and 5 using a scaling factor of 0.5, 2/3, 1.5 and 2. With (a) layer 1 & SF = 0.5, (b) layer 3 & SF = 0.5, (c) layer 5 & SF = 0.5, (d) layer 1 & SF = 2/3, (e) layer 3 & SF = 2/3, (f) layer 5 & SF = 2/3, (g) layer 1 & SF = 1.5, (h) layer 3 & SF = 1.5, (i) layer 5 & SF = 1.5, (j) layer 1 & SF = 2, (k) layer 3 & SF = 2 and (l) layer 5 & SF = 2.

One thing which can be observed from these results is that the variance in the amount of absorption is higher for the scale factors lower than 1. This implies that more rays should be used, which is 10000 for all simulations above. The reason that the variance is higher is that fewer rays per particle are used since r_{laser} is larger, making the simulation less precise. However, a general fitting line can still be observed. It can also be seen that for a higher scaling factor, the amount of absorption per particle is higher. This is because, relative to r_{laser}, the particle diameter is larger and it therefore absorbs a bigger portion of the light. For all scale factors, the analytical solution corresponds to the ray tracing simulations for the first layer.

However, for the rest of the particle bed, the analytical solution is incorrect. This deviation can be explained in the following way. Paragraph 4.2.2 showed that within the bed, the light rays scatter, causing the amount of absorption to deviate from the expected $e^{-\mu z\varphi}$. Here, a new equation was introduced in the form of $e^{-A(\mu z)^B \varphi}$. The factors A and B were chosen in such a way that the analytical would fit with the ray tracing simulations. Since the scattering depends on the amount of interaction between the light and the particles, these factors should depend on the particle size. Namely, a larger particle diameter D results in less interaction, since the laser beam covers fewer particles and is also absorbed by fewer particles. Furthermore, a higher attenuation μ coefficient results in less interaction since the light rays are more quickly absorbed and therefore reach fewer particles within the bed. It was found that keeping the factor B equal to 1.4 and replacing the part $-A$ with $A + B(\mu D)^C$ showed a good fit. The portion $e^{-E(\mu z)^F \cdot (\varphi - 0.574)^G}$, which calculates the effect

42

of the volume fraction, will be kept in the equation. A, B and C will be chosen in such a way that a scaling factor of 1 will result in an unchanged analytical solution. It was found that the factors $A = -0.036$, $B = -0.45$ and $C = -0.48$ showed a good fit, making the final equation equal to $e^{\left(-0.036-0.45(\mu D)^{-0.48}\right)(\mu z)^{1.4}-3.8(\mu z)^{0.3}\cdot(\varphi-0.574)^{0.8}}$. For a scaling factor of 1, $\mu D = 27400 \cdot 0.00006 = 1.644$. This makes the part $-0.036 - 0.45(\mu D)^{-0.48}$ equal to -0.39, which is indeed the same as the original equation. Using this new equation, the analytical equation fits the ray tracing simulations for all scale factors. Fig. 42 shows the results of the new equation for layers 2, 3 and 4.
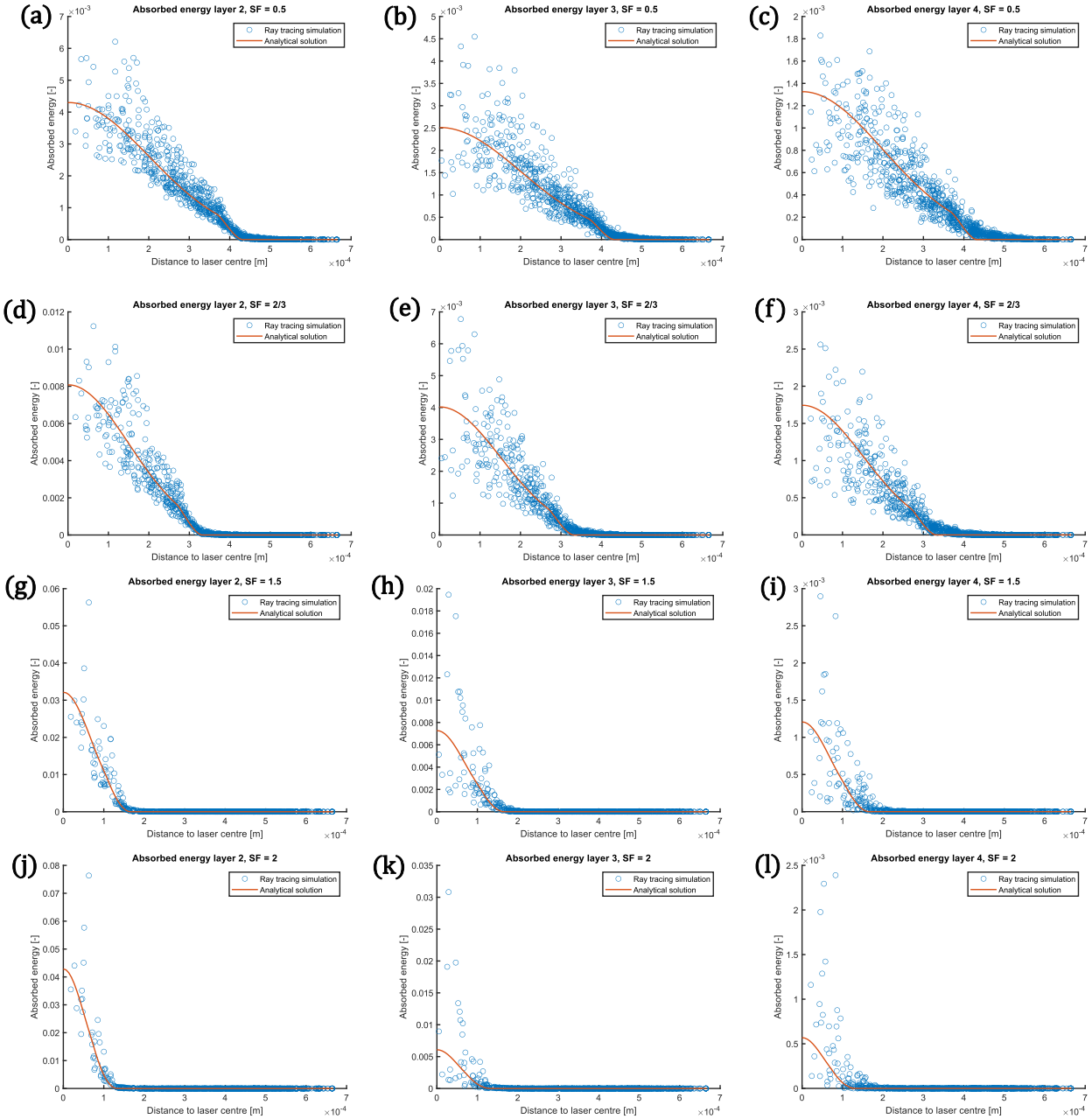

Fig. 42. New analytical solution with ray tracing simulations for layers 2, 3 and 4 using a scaling factor of 0.5, 2/3, 1.5 and 2. With (a) layer 2 & SF = 0.5, (b) layer 3 & SF = 0.5, (c) layer 4 & SF = 0.5, (d) layer 2 & SF = 2/3, (e) layer 3 & SF = 2/3, (f) layer 4 & SF = 2/3, (g) layer 2 & SF = 1.5, (h) layer 3 & SF = 1.5, (i) layer 4 & SF = 1.5, (j) layer 2 & SF = 2, (k) layer 3 & SF = 2 and (l) layer 4 & SF = 2.

Now, the equation correctly takes into account the ratio of μ and D, the ratio of r_{laser} and D, and the volume fraction φ. Next, the equation will be tested whether it corresponds to the simulation if a laser at an angle is used.

Effect of laser angle

In SLS 3D printers, the laser generally comes from a single source, using a set of mirrors to direct the laser to the specified locations on the particle bed. Here, the angle of the laser compared to the bed, θ, varies as the laser beam needs to travel a horizontal distance to the outermost particles. If a perpendicular light direction has a value of 0°, this angle generally reaches values up to 20°. Any angle larger than 10° already results in a significantly lower printing accuracy due to a deformed and out-of-focus laser at the bed level (Bibas, 2020).
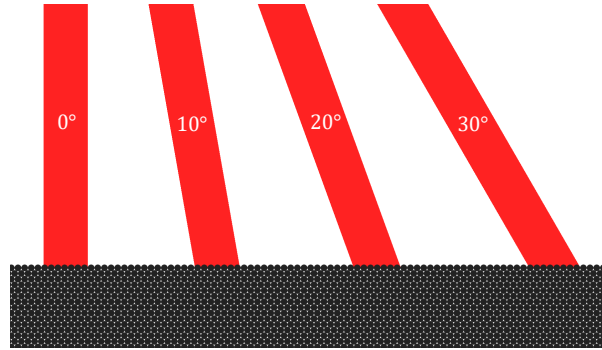

Fig. 43. Illustration of four different incoming laser angles θ of 0°, 10°, 20° and 30° used in the ray tracing simulations.

Here, aside from the already simulated angle of $\theta = 0°$, three different angles will be simulated: 10°, 20° and 30° as shown in Fig. 43. Even though in practice no angle larger than 30° is used, simulating a higher angle will ensure the equation works well within the typical angle region. Furthermore, $D = 60$ μm, $\mu = 27400$ m^{-1}, $\varphi = 0.6$ and $r_{laser} = 200$ μm.

For a laser angle of $\theta = 0°$, the absorption of all particles can be plotted in one graph due to the circular symmetry of the laser beam and therefore also the absorption of the particles. All particles with the same distance to the laser and depth within the bed receive approximately the same amount of energy for both cases, however, this is not symmetric for a laser at an angle. Fig. 44 shows the simulation results of a single slice of the bed for two incoming laser angles, parallel to the YZ plane. The centre of the laser lies on this centre plane, and only the particles which have their centre with a maximum horizontal distance of $D/2$ from this plane, are shown. Here, the colour scale is logarithmic and a combination of four simulations for both $\theta = 0°$ and $\theta = 30°$ is shown.
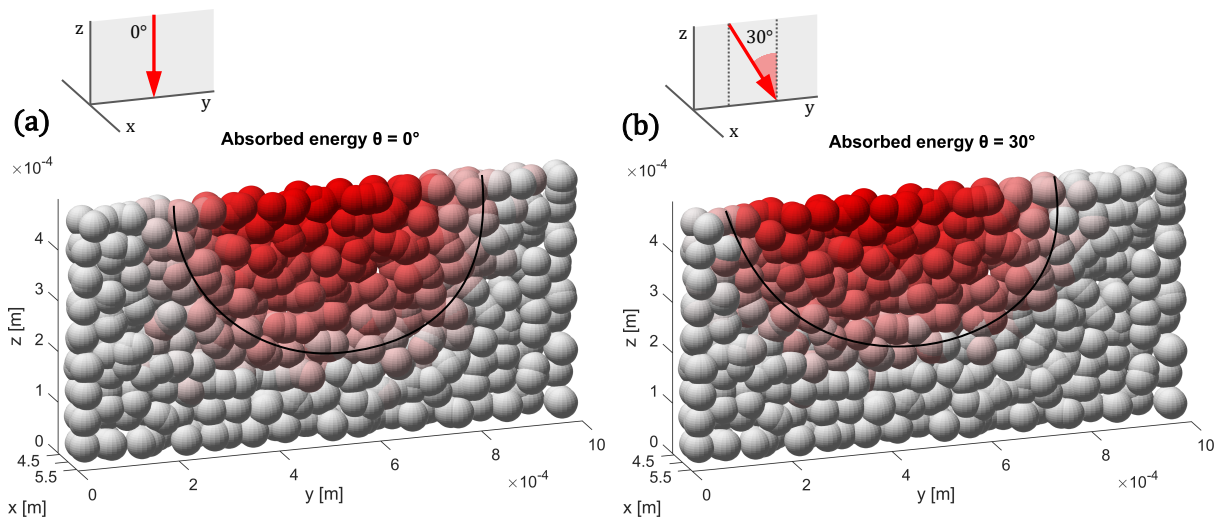

Fig. 44. Logarithmic absorption for particles at the centre of the bed for a laser angle of (a) $\theta = 0°$ and (b) $\theta = 30°$. The black line indicates the region of particles affected by the laser.

Aside from the slightly asymmetric region for $\theta = 30°$, both figures show a similar amount of absorption. When looking at the amount of energy escaping the bed, which is either at the bottom

or sides of the bed or reflecting away at the top, also here the values do not show a significant difference. Table 5 shows the amount of escaped energy in % for all incoming laser angles.

θ	0°	10°	20°	30°
Escaped energy	2.384	2.216	2.274	2.493

Table 5. Escaped energy in % for all incoming laser angles.

To see whether the current analytical equation is correct for a laser angle other than 0°, a different analysis can be used. Namely, all particles in one layer have the same propagation depth z, which is the original equation for z (Eq. (47)) divided by the cosine of the incoming angle:

$$z = \left((i-1) \cdot D \cdot \sqrt{6}/3\right) / \cos\theta \tag{48}$$

Each layer, which has a specific z, can be analysed individually by plotting the absorption based on the distance to the laser centre of each particle. This distance to the laser centre d is not the distance on the layer which is analysed, but the shortest distance to the entire laser. This can be calculated with the following equation:

$$d = \frac{\left|(\bar{c} - \overline{p_p}) \times \vec{k}_0\right|}{\left|\vec{k}_0\right|} \tag{49}$$

With $\bar{c}$ the coordinates of the centre of the laser beam at any point on the laser in m, $\overline{p_p}$ the coordinates of the centre of a particle in m, and $\vec{k}_0$ the initial direction of the laser [−]. Fig. 45 shows the amount of absorption for the first and second layer based on the position in the bed and the distance to the laser centre. On the right half, the analytical solution is used to create a colour graph. All figures use the same colour scale.
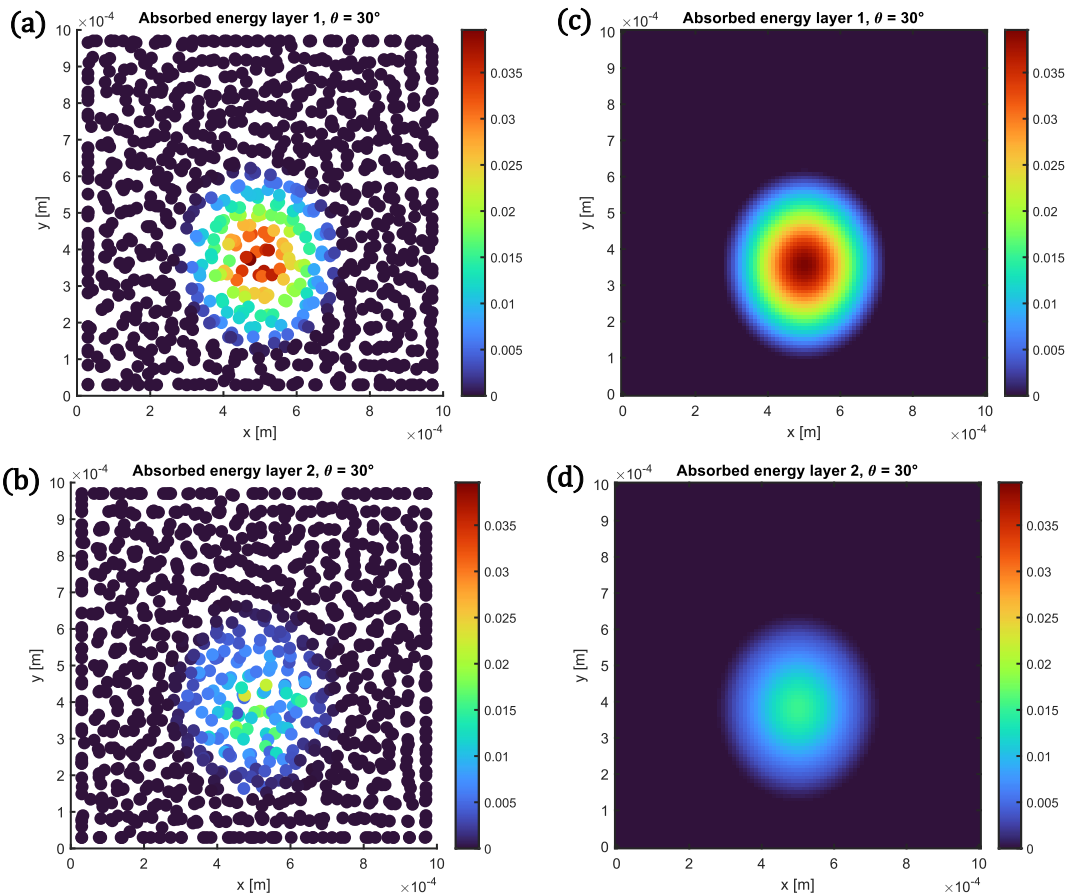

Fig. 45. Energy absorption for (a) the first layer and (b) the second layer based on the ray tracing simulations. Similarly, (c) and (d) show the energy absorption based on the analytical solution.

45

Here, the centre of the laser is not in the centre of the bed on the first layers. This is done because the laser is directed in the y direction, therefore the laser is centred at the middle of the bed height. For both the first and second layers, the figure shows that the analytical result agrees with the ray tracing simulations. To make a better comparison, again the method can be used of plotting the distance to the laser centre against the absorption for a single layer. Now, Eq. (48) is used for the propagation depth to calculate the decrease of the absorption within the bed. Fig. 46 shows the absorption for layers 1, 2 and 4 for both the ray tracing simulation and the analytical solution, for an incoming laser angle of 10°, 20° and 30°.
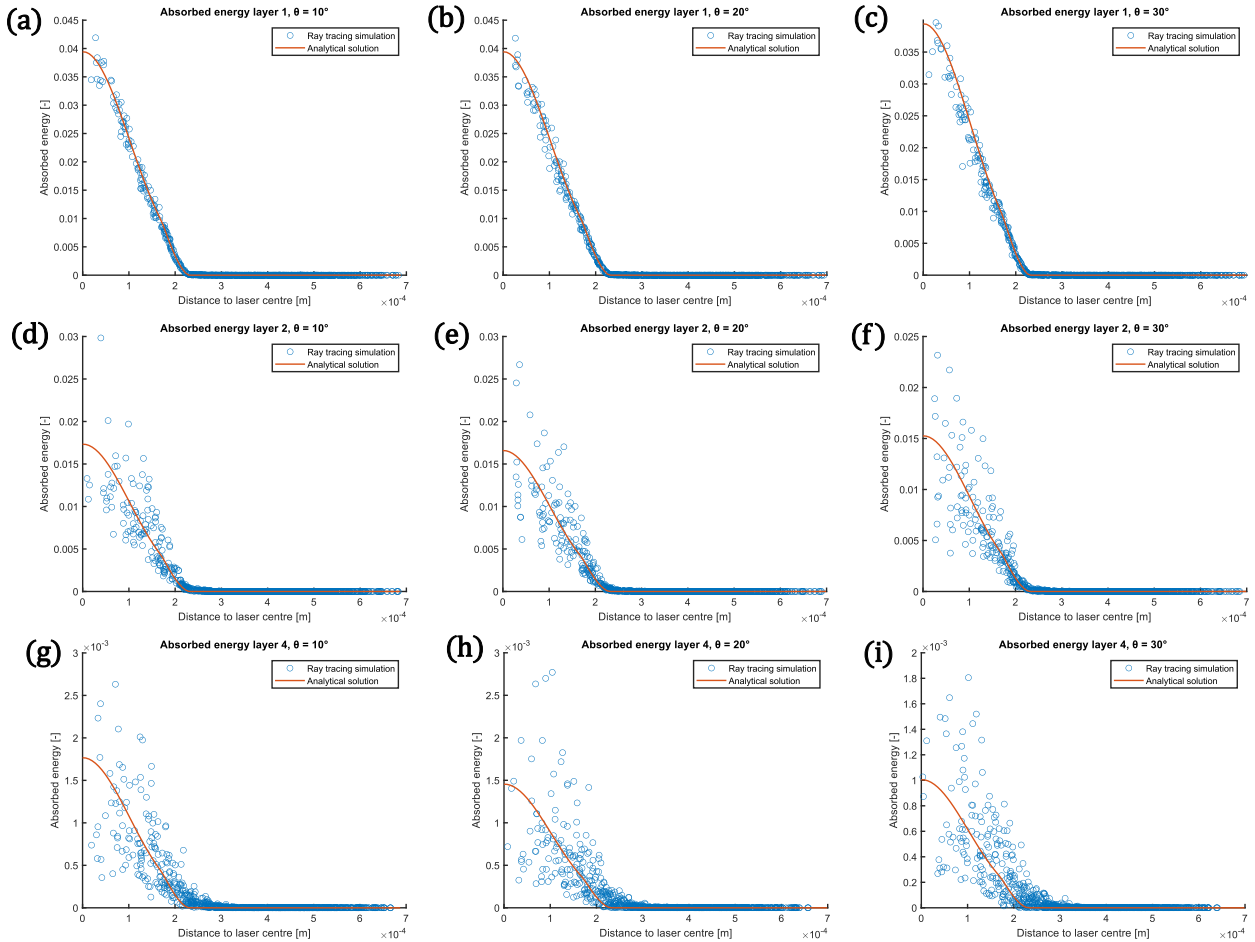

Fig. 46. Energy absorption for layers 1, 2 and 4 for an incoming laser angle of 10°, 20° and 30°. With (a) layer 1 & $\theta = 10°$, (b) layer 1 & $\theta = 20°$, (c) layer 1 & $\theta = 30°$, (d) layer 2 & $\theta = 10°$, (e) layer 2 & $\theta = 20°$, (f) layer 2 & $\theta = 30°$, (g) layer 4 & $\theta = 10°$, (h) layer 3 & $\theta = 20°$, and (i) layer 4 & $\theta = 30°$.

As can be seen, the analytical solution corresponds with the results of the ray tracing simulations for all incoming laser angles up to $\theta = 30°$. This shows that, other than including θ in the propagation distance z according to Eq. (48), the analytical solution does not need to be changed.

Effect of refraction index ratio

Lastly, the effect of the refraction index ratio x will be investigated. If a different material is simulated, the refraction index of the material n_B and therefore also the ratio of the refractive indices of the material and the surrounding air, $x = n_A/n_B$, can be different. For example, PA12, a different material commonly used in SLS, has a refraction index of $n_B = 1.525$ (Polymerdatabase, n.d.) compared to the higher refraction index of PS, $n_B = 1.5997$. While these values do not differ significantly, other materials used in SLS can have a refraction index ranging between 1.4 and 1.8. Fig. 47 shows the effect of the refractive index on the path of the light rays, which is generated with the tool Ray Optics Simulation (Yi-Ting & Johnson, 2016).
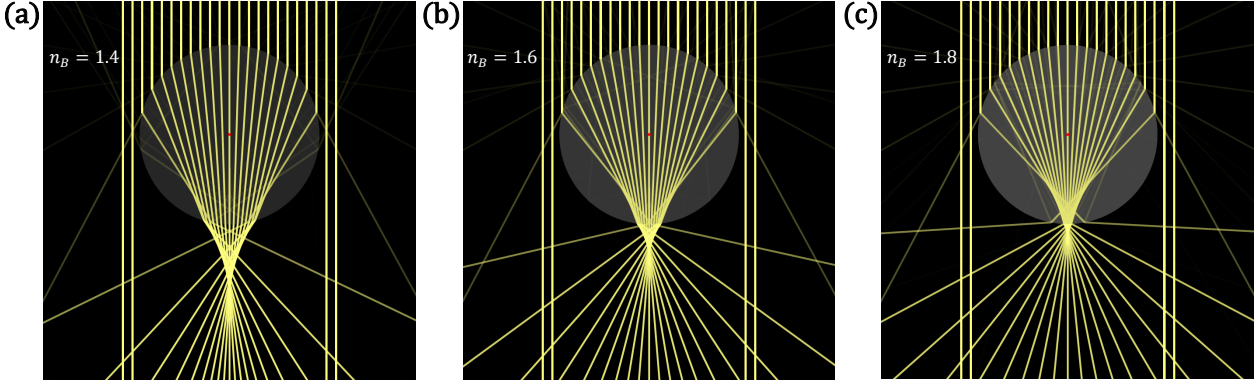
Fig. 47. Difference in light ray paths due to a different refraction index of (a) $n_B = 1.4$, (b) $n_B = 1.6$ and (c) $n_B = 1.8$.

The figure shows that the refraction index has an effect on the direction of the refracted light, but not on the direction of the reflected light. This can also be concluded from Eq. (1) and Eq. (2), which calculate the angle incidence α and the angle of refraction β. Furthermore, the refraction index has an effect on the reflected energy portion factor R according to Eq. (3). For most incoming angles ($0° < \alpha < \pm 80°$), R will increase for an increasing value of n_B. This means that for a higher n_B, more energy is reflected away from the particle. This might have an effect on the light absorption at the first layer, as more light being reflected away can result in a lower absorption by the particles.

To see how much of an effect the value of the refraction index has on the absorption, this value can simply be changed in the analytical solution. Fig. 48 shows the energy absorption of the first layer based on the ray tracing simulations and the analytical solution. Only the analytical solution uses three different values for the refraction index of the material: $n_B = 1.4, n_B = 1.5997$ and $n_B = 1.8$.
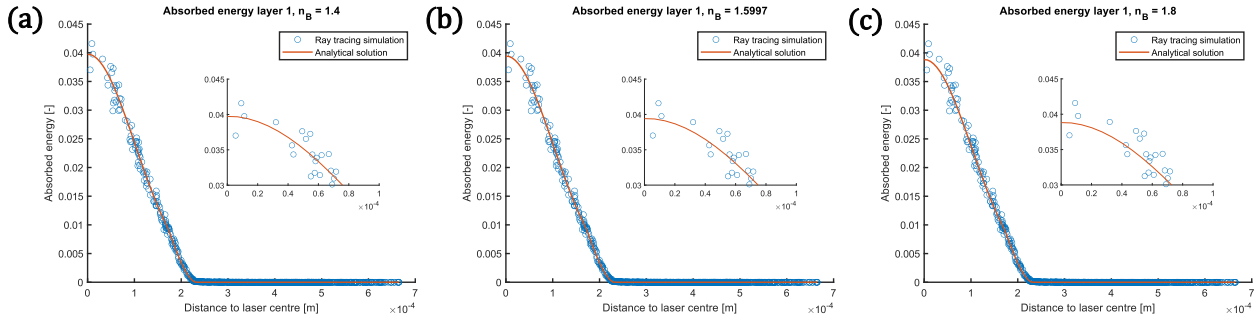

Fig. 48. First layer energy absorption from the ray tracing simulations, together with the analytical solution using three different refraction indices of (a) $n_B = 1.4$, (b) $n_B = 1.5997$ and (c) $n_B = 1.8$. For each graph, a zoomed-in version is shown.

The difference in absorbed energy is marginal, a zoomed-in version of the graph is necessary to show a small difference in the peak absorption. As expected, a higher refraction index results in a lower absorption for the first layer. The peak absorption values are $E_{peak} = 0.0397$ for $n_B = 1.4$, $E_{peak} = 0.0394$ for $n_B = 1.5997$ and $E_{peak} = 0.0388$ for $n_B = 1.8$. Compared to the original refraction index of $n_B = 1.5997$, the overall absorption in the top layer is increased by 0.8% for $n_B = 1.4$ and decreased by 1.5% for $n_B = 1.8$.

Since the result of the analytical solution is a single line that should be the best fit in the result of the ray tracing simulations, which has a small amount of randomness, rerunning the simulations with a different refraction index will result in an absorption with no visible difference. These simulations will therefore not be conducted and n_B will be used in the analytical equation as it currently is, namely for the calculation of β and R.

Now, all variables affecting the total energy absorption E are known, which can be used to calculate the temperature evolution according to Eq. (12). The final model is shown in Appendix H.

4.3 Random walk

So far, two simulation simplifications have been described: finding an equation for the light absorption for a particle doublet and for a bed of particles. The third simplification does not involve finding an equation, but shows a different way of simulating light rays propagating in a particle bed. For this, the implementation of a random walk will be investigated. A random walk is a type of simulation in which a certain object, in this case a light ray, follows a path in 2D or 3D using randomised steps. Here, the phenomenon of light rays propagating into a powder bed will be replaced by rays performing a random walk in a bed with virtual particles.

The reason this method is investigated is to find a simulation method which can be run much more quickly compared to the original ray tracing simulations, and is not replaced by an equation. If a simulation method can be found which can be run during the transient sintering simulations in MercuryDPM, it might have an advantage over the analytical equation since the random walk would feature the randomness in the energy absorption, compared to the single line of the analytical equation.

4.3.1 Proposed calculation method

The resulting simulation of the random walk will be compared with the ray tracing simulations. The random walk would need to have properties, similar to a normal particle bed, such as the volume fraction and the particle diameter. To be able to compare both simulation methods, the random walk cannot simply be a random walk with a random direction change of each ray, but needs to follow some rules. The proposed calculation method will therefore be called a semi-random walk.

Similar to the ray tracing method, the simulation will simulate lines propagating through a bed. This time, the simulation does not use a bed consisting of many particles, but instead uses a random chance of the light changing from medium A to B, or vice versa. This creates a virtual particle, which is only used to give a direction change for a single light ray. Subsequently, the amount of light being absorbed by that virtual particle is stored as a number (the amount of absorbed energy) and a location (the centre of the virtual particle. Once the simulation is finished, the final result is a list of absorbed energy portions in different locations in the bed. The amount of created virtual particles is of no importance.

Firstly, a list of light rays is created with a certain number of light rays N_{ray}. Then, the following steps will happen to each light ray once they enter the region specified as the area where virtual particles exist. The ray is propagating through the air with a direction $\vec{k}$. After length l_{air}, which is a random number, the ray enters a particle with a diameter D. It enters this particle with a distance r to the centre of the particle perpendicular to the z-axis, with $r = \frac{D}{2}\sqrt{\texttt{rand()}}$. Here, $\texttt{rand()}$ is a random number from a uniformly distributed interval between 0 and 1. The azimuth angle the ray has with the YZ plane is $\gamma = 2\pi \cdot \texttt{rand()}$. Based on this r and γ, the reflected direction $\vec{k}_R$, transmitted direction $\vec{k}_T$ and reflected energy portion factor R are calculated. This also determines the position where the ray leaves the particle. Fig. 49 shows a 3D visualisation of this ray and its directions and distances.

The position where the ray enters a particle is $\bar{p}$. The centre of this particle, $\overline{p_p}$, can be calculated using the following equation:

$$\overline{p_p} = \bar{p} + \vec{k}\sqrt{(D/2)^2 - r^2} - r\left(\vec{h}\cos\gamma + (\vec{k} \times \vec{h})\sin\gamma\right) \quad \text{with} \quad \vec{h} = \begin{pmatrix} 0 \\ -k_3 \\ k_2 \end{pmatrix} \qquad (50)$$

The direction of the surface normal becomes $\vec{n} = \bar{p} - \overline{p_p}$. The angle of incidence α, angle of reflection β and the reflected energy portion R are calculated according to Eq. (1), (2) and (3) respectively.
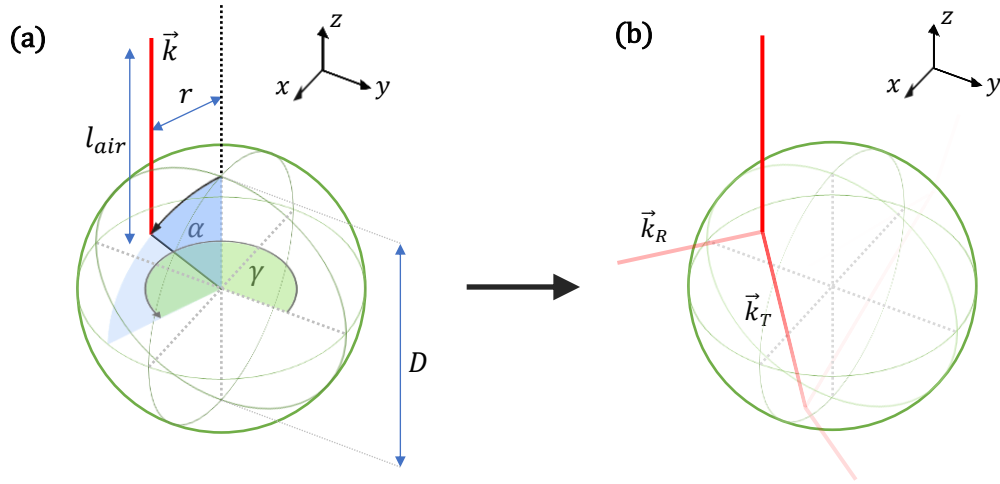
Fig. 49. (a) 3D visualisation of a spherical particle with diameter D and an incoming ray with direction $\vec{k}$. Here, r, l_{air} and γ are chosen randomly. (b) The ray splits up in a reflected ray with direction $\vec{k}_R$ and transmitted ray with direction $\vec{k}_T$.

When the ray changes from medium A to medium B, it splits up into a reflected ray and a transmitted ray. If the energy of the incoming ray is I_I, then the reflected ray will continue with an energy of $I_R = R I_I$ and the transmitted ray with an energy of $I_T = (1 - R) \cdot I_I$. The directions of these rays are calculated using the following equations:

$$\vec{k}_R = \vec{k} + 2\vec{n} \cos \alpha \tag{51}$$

$$\vec{k}_T = x\vec{k} + \vec{n}(x \cos \alpha - \cos \beta) \tag{52}$$

The transmitted ray will continue in the particle with a distance of $l_p = D \cos \beta$ until it encounters another medium change at point $\bar{p} = \bar{p}_{old} + l_p \vec{k}_T$, with $\bar{p}_{old}$ the previous intersection point. During this distance, the energy of the transmitted ray will decrease from $I_T = (1 - R) \cdot I_I$ to $I_T = (1 - R) \cdot I_I \cdot \exp(-\mu l_p)$. When the energy dissipation threshold is reached, the ray stops propagating.

Another advantage of this semi-random walk is that only the coordinates at which medium changes occur are saved, compared to the ray tracing simulation where every spatial step size Δl the position of the light ray is stored. This results in less data being stored and the calculation time being decreased. The ray tracing method uses a relatively small Δl, for example 10% of the particle diameter, to ensure that a ray does not completely miss a particle as it checks for a medium change after every distance Δl. Since the rays in a semi-random walk will only enter a single new particle after distance l_{air}, the phenomenon of total internal reflection (TIR) will also not occur, since TIR can only happen when a ray enters two particles simultaneously. A comparison between the semi-random walk and the ray tracing simulation will show if the absence of TIR causes a difference in absorption.

Equation for l_{air}

Another variable which will include randomness is the distance a ray is travelling between two particles, l_{air}. The value of l_{air} will depend on the volume fraction φ, since a ray has a higher chance to encounter a new particle if the particles are more closely packed. Whether the random distribution of l_{air} is uniform or not, will be determined by analysing the ray tracing simulations. For all simulated values of φ ranging from 0.575 to 0.7 and four simulations per volume fraction, the distance a light ray is travelling between two particles is registered. For every simulation, 1600 staring rays are used. To show the value of this distance l_{air} and its distribution, Fig. 50 (a) shows l_{air} on the vertical axis and a counter on the horizontal axis. Fig. 50 (b) shows a histogram of the frequency distribution of the values shown in (a).
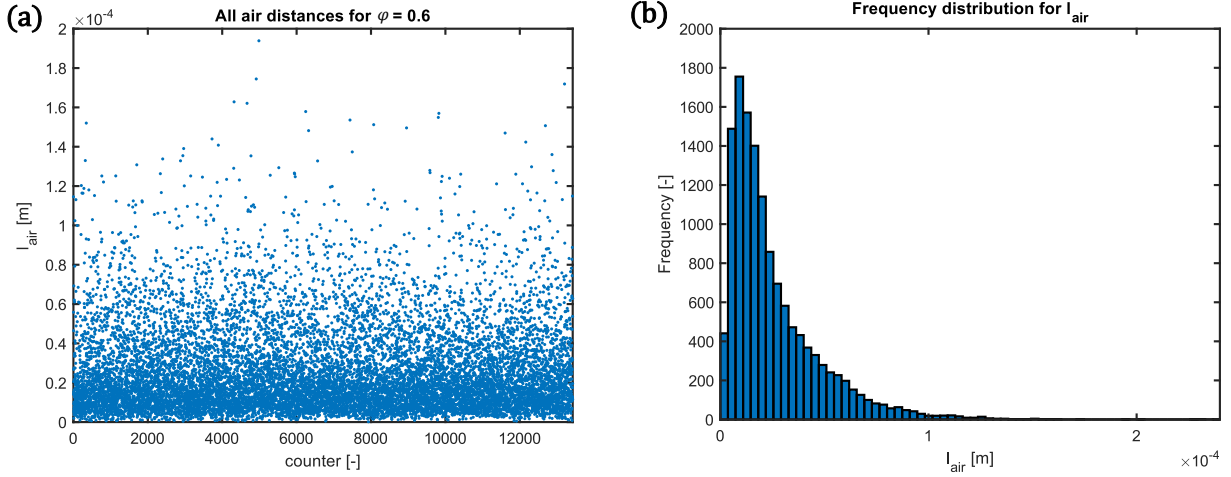
Fig. 50. (a) Air distance l_{air} for all rays in the ray tracing simulation for $\varphi = 0.6$, $D = 60$ μm and $N_{ray} = 1600$. (b) The frequency distribution of the values shown in (a).

From the 1600 starting rays, there are 13422 sections where a ray is between two particles as shown in Fig. 50 (a). The highest frequency is around 8.7 μm, which is 14.5% of the particle diameter. For the histogram in Fig. 50 (b), a probability distribution can be fit. Even though the height of the bars depends on the number of air distances and the number of bars used in the histogram, MATLAB® can find a best-fitting probability distribution that fits with the frequency distribution. The best-fitting distribution was found to be a lognormal distribution. With the function `histfit()`, a fitting probability distribution curve can be shown on the histogram. This is shown in Fig. 51, where l_{air} is divided by the particle diameter D on the horizontal axis.
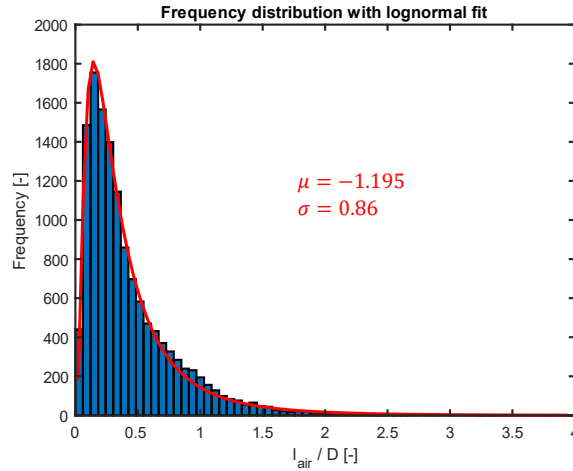

Fig. 51. Frequency distribution of l_{air} with fitting lognormal distribution for $\varphi = 0.6$ and $N_{ray} = 1600$. The best fitting distribution has $\mu_w = -1.195$ and $\sigma_w = 0.86$.

A lognormal distribution has two variables: μ_{air} and σ_{air}, which are the average and the standard deviation of the natural logarithm of the variable, l_{air}/D in this situation. For $\varphi = 0.6$, these values are $\mu_{air} = -1.195$ and $\sigma_{air} = 0.86$ as indicated in Fig. 51. Here, μ_w and σ_w are independent of N_{ray}, a higher number of rays simply gives a more consistent value for μ_{air} and σ_{air}. For all other simulated volume fractions, μ_{air} and σ_{air} are shown in Table 6.

φ	0.575	0.6	0.625	0.65	0.675	0.7
μ_{air}	-1.2098	-1.1954	-1.2561	-1.3055	-1.3673	-1.4112
σ_{air}	0.8784	0.8600	0.8465	0.8386	0.8291	0.8143

Table 6. Resulting values for μ_{air} and σ_{air} for all simulated volume fractions.

Since the air distance is divided by D, both μ_{air} and σ_{air} are dimensionless. It is assumed that the air distance l_{air} scales linearly with the particle diameter, since both variables scale linearly in space. If D is multiplied by a factor A, then μ_{air} is increased with $\ln(A)$ and σ_{air} remains constant.

For both μ_{air} and σ_{air}, a fitting curve can be found depending on the volume fraction. Fig. 52 shows the values according to Table 6.
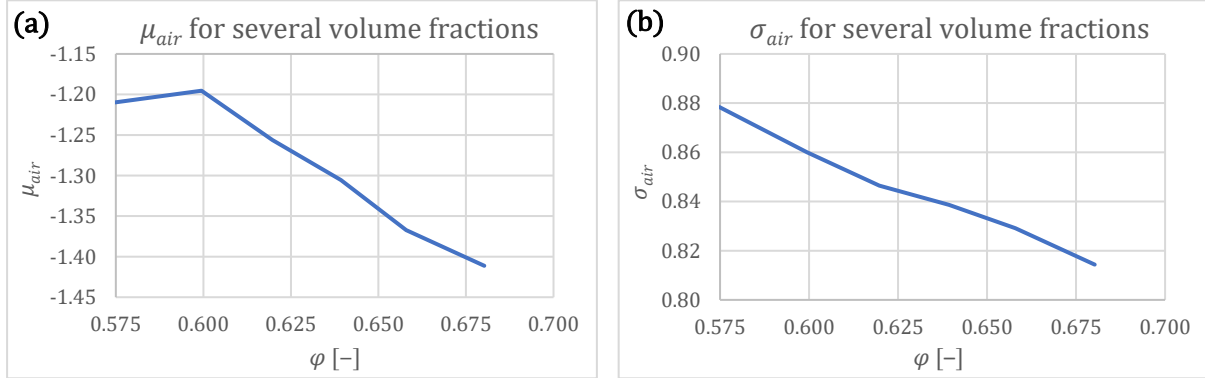

Fig. 52. (a) μ_{air} and (b) σ_{air} plotted for several volume fractions according to the values given in Table 6.

For the range of φ that is used, both the μ_{air} and σ_{air} seem to follow a linear trend. There is an exception for μ_{air} at $\varphi = 0.575$. However, since the particle bed at this volume fraction is not packed as φ is around the minimum possible value, the particles tend to follow a similar distance as $\varphi = 0.6$. Since $\varphi = 0.575$ is difficult to reach in practice, it will be excluded from the fitting curves. The resulting fitting curves have the following equation:

$$\mu_{air} = -2.7136\varphi + 0.4278 \tag{53}$$

$$\sigma_{air} = -0.5846\varphi + 1.212 \tag{54}$$

Here, μ_{air} is generalised for a particle size of 1. For a particle size of D, μ_{air} needs to be increased with $\ln(D)$, σ_{air} remains constant:

$$\mu_{air} = -2.7136\varphi + 0.4278 + \ln(D) \tag{55}$$

Eq. (54) and Eq. (55) will be used in the function `lognrnd()` in MATLAB® to generate a value for l_{air}:

$$l_{air} = \text{lognrnd}(\mu_{air}, \sigma_{air}) \tag{56}$$

Equation for l_{start}

Lastly, the air distance for the starting rays hitting a particle follows a different distribution. Namely, this is the distance of a ray starting from the region specified as the bed area, which is at the bed height Z, to the first particle that the ray intersects with, referred to as l_{start}. Similarly to l_{air}, the values for l_{start} can be plotted and made into a histogram from the ray tracing simulations. This is shown in Fig. 53.

This time, the frequency distribution is different. A clear second wave is visible. This can be explained by the fact that some particles happen to completely miss the first layer of particles, and only enter a particle inside the second layer. Therefore, the peak of the second wave is at a distance of ± 50 μm in the bed, which corresponds to the layer height of 60 μm $\cdot \sqrt{6}/3 \approx 49$ μm. A combination of multiple probability distributions could be used as a fitting curve, however, this would also require the probability of which of these distributions should be used for the calculation of l_{start}. Since the first air distance l_{start} is expected to have a low effect on the absorption results for the random walk, a lognormal fitting distribution will be used as a fitting curve, similarly to l_{air}.
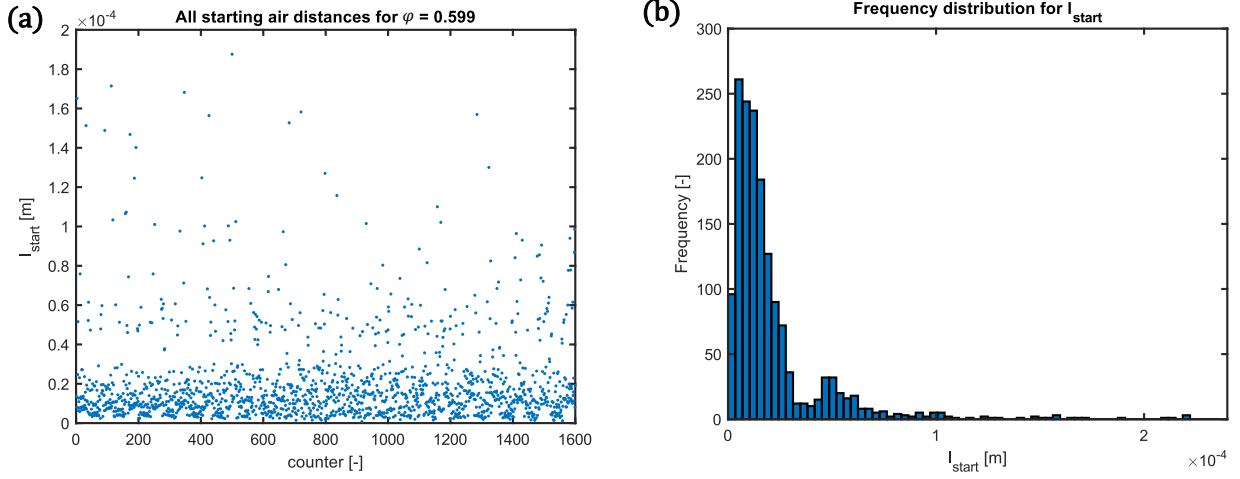
Fig. 53. (a) Starting air distance l_{start} for all rays in the ray tracing simulation for $\varphi = 0.6$, $D = 60$ μm and $N_{ray} = 1600$. (b) The frequency distribution of the values shown in (a).

Since the starting air distance only applies to the first layer, which has its particles at the highest possible z coordinate, it is assumed that the volume fraction has no effect on l_{start}. Fig. 54 shows the resulting fitting curve:
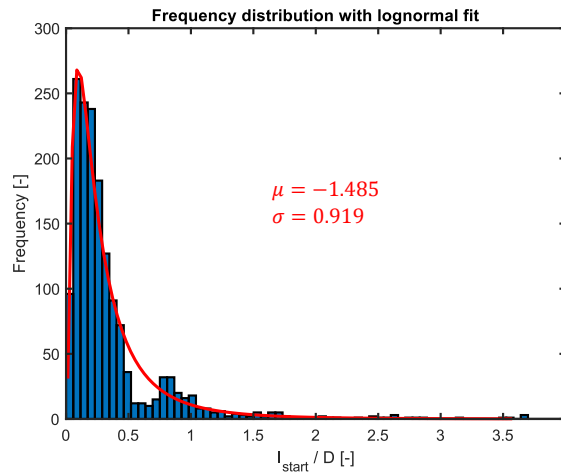

Fig. 54. Frequency distribution of l_{start} with fitting lognormal distribution for $\varphi = 0.6$ and $N_{ray} = 1600$. The best fitting distribution has $\mu_{start} = -1.485$ and $\sigma_w = 0.919$.

Similarly to l_{air}, the average of the natural logarithm μ_{start} and the standard deviation of the natural logarithm σ_{start}, both of l_{start}, can be found. Here, μ_{start} can be dependent on the particle diameter by adding $\ln(D)$ in the equation:

$$\mu_{start} = -1.48462 + \ln(D) \tag{57}$$

$$\sigma_{start} = 0.919366 \tag{58}$$

Making the equation for l_{start}:

$$l_{start} = \texttt{lognrnd}(\mu_{start}, \sigma_{start}) \tag{59}$$

Now, all values are known to simulate the semi-random walk.

4.3.2 Simulation results

In Fig. 55, the resulting ray paths of a semi-random walk simulation are shown. 625 rays start in a square of 1 x 1 mm and propagate in a virtual particle bed. Since the simulation assumes there are virtual particles everywhere below the bed height Z, the rays can propagate outside the 1 x 1 mm boundary. Similarly to the ray-tracing simulations, the rays can also reflect away at the top.
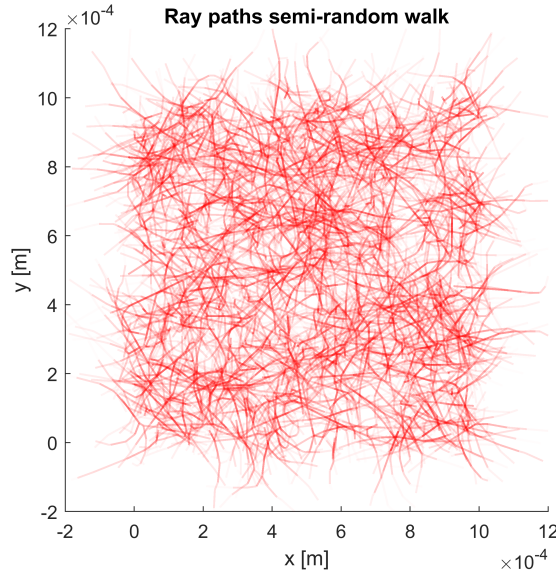
52

Fig. 55. Top view of the semi-random walk with 625 starting rays with a logarithmic colour scale. The bed has virtual particles with a constant size of $D = 60$ μm, $\varphi = 0.6$, $\mu = 27400$ m^{-1} and $x = 1/1.5997$.

Fig. 56 shows the side view of the random walk with a linear and a logarithmic colour scale. Since the random walk uses virtual particles, a new particle is generated for every instant a line refracts and reflects. This creates a list of particles which have only one ray absorbed. To find an indication of the amount of absorbed energy in the bed, the bed needs to be divided into layers. Subsequently, for each layer, the amount of energy for all virtual particles in that layer will be added. This creates the amount of absorbed energy per layer. Similarly to a bed with physical particles, layers will be used, as a bed with a height of 500 μm with particles of $D = 60$ μm results in 10 layers. Fig. 56 (b) shows these layers. To have a good comparison with the ray tracing simulations, only the virtual particles that are within the particle bed boundaries will be used for this summation.
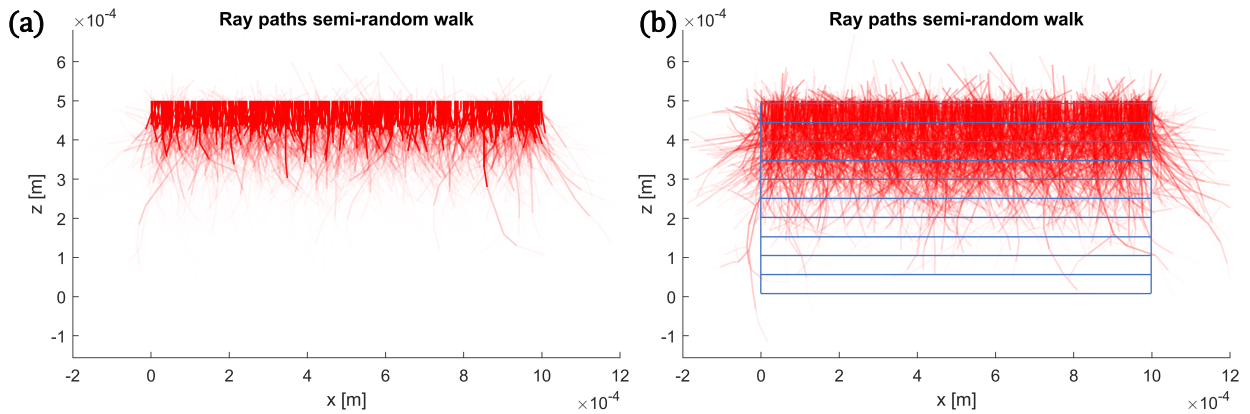

Fig. 56. Ray paths of a semi-random walk with 625 starting rays showing the energy with (a) a linear colour scale and (b) a logarithmic colour scale. The blue lines indicate the boundaries of the 10 layers.

The results of this summation are shown in Fig. 57, showing a linear and logarithmic scale. Here, $N_{ray} = 10000$. In the logarithmic scale, a straight line for the absorption per layer is visible. This is to be expected, as the light energy and therefore the absorption decreases exponentially according to Eq. (4). As a comparison, Fig. 58 shows the results of a ray tracing simulation with equal variables: 10000 rays are cast on a particle bed of 1 x 1 x 0.5 mm, with $D = 60$ μm, $\varphi = 0.6$, $\mu = 27400$ m^{-1} and $x = 1/1.5997$.
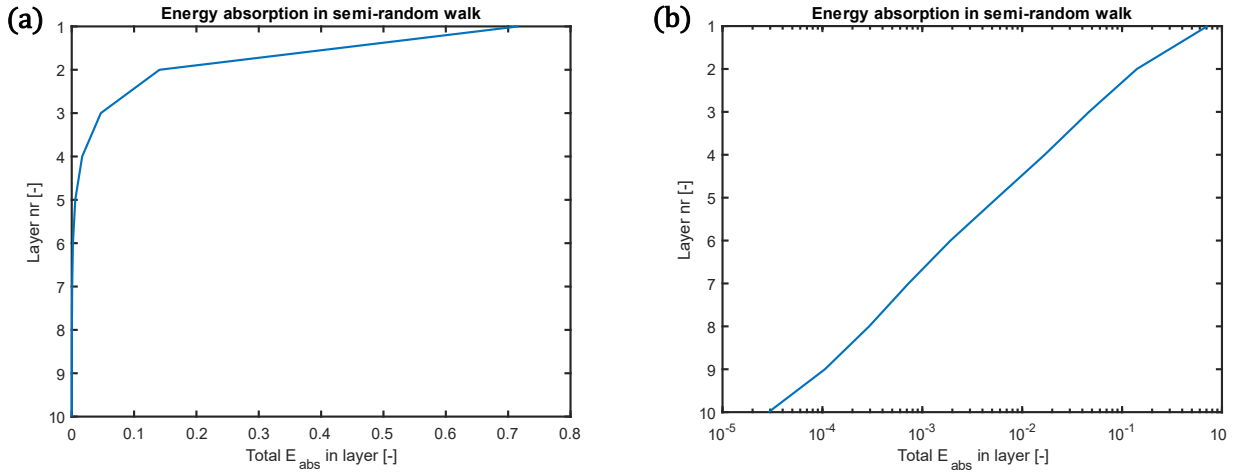
Fig. 57. Total energy absorption E_{abs} per layer for a semi-random walk simulation with (a) a linear scale and (b) a logarithmic scale.
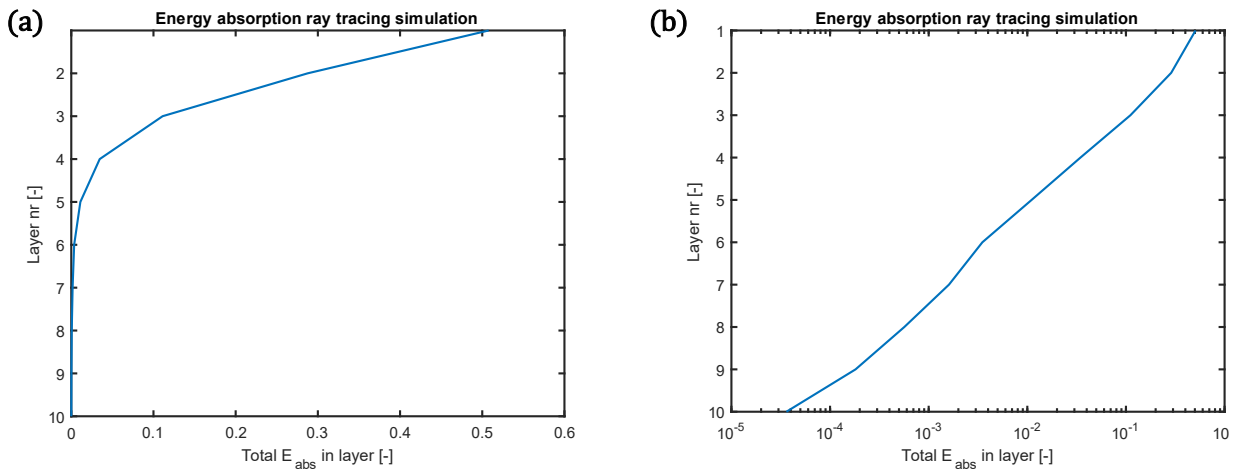

Fig. 58. Total energy absorption E_{abs} per layer from a ray tracing simulation with (a) a linear scale and (b) a logarithmic scale.

While both types of simulations show a straight line for the absorption in the logarithmic scale, the absorption for the random walk is significantly lower in the top layers. The energy absorption in the first layer for the ray tracing simulations is $E_{abs} = 0.508$, while the random walk results in $E_{abs} = 0.716$. The total amount of absorbed energy for both methods is more similar, $E_{abs} = 0.958$ for the ray tracing method and $E_{abs} = 0.929$ for the random walk. Fig. 59 compares the path of the rays for both simulation types. For a good comparison, the random walk shown in Fig. 59 (a) uses rays that are divided in a grid instead of using randomised positions, similar to (b). Both simulations use $N_{ray} = 625$.
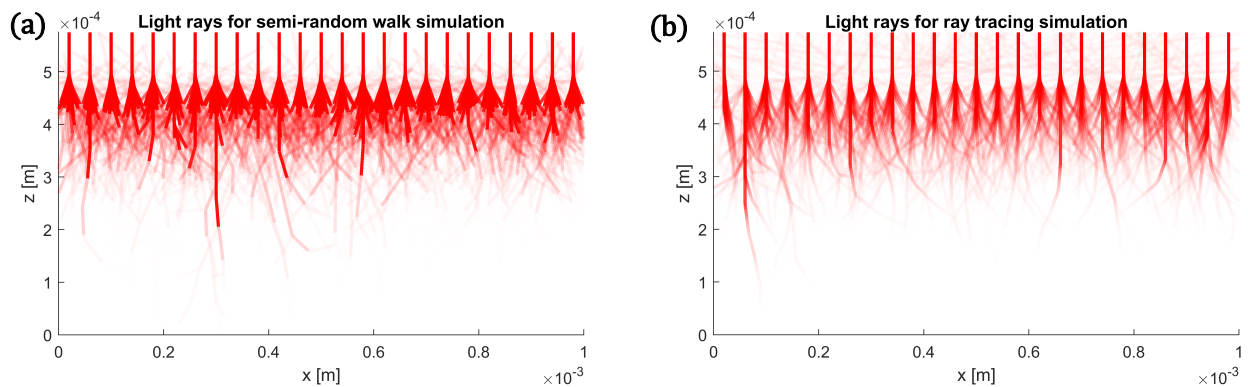

Fig. 59. Path of light rays for (a) a semi-random walk simulation with virtual particles and (b) a ray tracing simulation with physical particles, both with $N_{rays} = 625$.

Since the random walk only generates a new ray section when reflection and refraction occur, and each ray can only have a single colour, there is no smooth transition between the colours. The ray tracing simulation has spatial steps of $\Delta l = 10\%$ of the particle diameter and can therefore show a finer transition. Aside from the smoothness of the colour transition, both simulations show similar light paths.

A difference which could explain the difference in absorption as shown in Fig. 58, is the fact that the vertical walls of the ray tracing simulations always have particles adjacent to the wall, whereas the random walk uses virtual particles spread out through the bed. This can be seen in Fig. 59 (b) at the left and right walls at the top layer, where all rays refract inwards and therefore do not leave the bed. In Fig. 59 (a), the rays at the boundary of the bed at the top layer do leave the bed, which results in a lower absorption at this layer. If the usage of the random walk is investigated in further research, a better comparison might lead to a similar absorption for both methods. For example, the starting rays can be divided into a square of 0.9 x 0.9 mm, which resolves the problem of the outer rays refracting inwards.

However, there is a problem so far undiscussed about the usage of a random walk. Namely, only the total absorbed energy per layer can be calculated, as the bed consists of many virtual particles that only absorb a single ray. When a laser beam is used, it is therefore not possible to calculate the absorbed energy at a certain distance from the laser. The bed could be divided into a 3D grid, and the amount of absorbed energy for all virtual particles within each region could be added to achieve the absorbed energy per region. This absorbed energy per region is necessary to link the absorption at a certain position relative to the laser, to the absorption of physical particles with a certain position. However, this would require many starting rays as each region would have a low number of virtual particles.

Lastly, the calculation time is discussed. A random walk has shown to be very calculation-friendly compared to the ray tracing simulations. Table 7 below shows the calculation times for the energy absorption for a 1 x 1 x 0.5 mm bed with 2653 particles with $D = 60$ µm, $\varphi = 0.6$, $\mu = 27400$ m^{-1} and $x = 1/1.5997$ using the three calculation methods discussed in this paper. These methods are the ray tracing simulations shown in chapter 3, the replacement equations shown in paragraph 4.2, and the random walk shown in paragraph 4.3. The random walk uses rays starting in a square grid, the ray tracing simulation and the replacement equations use a beam with $r_{laser} = 200$ µm. Both the ray tracing simulations and the random walk use $N_{ray} = 10000$.

Calculation method	Ray tracing simulation	Replacement equations	Semi-random walk
Calculation time	±85 minutes	±0.07 seconds	±5 seconds

Table 7. Comparison between calculation times of the ray tracing simulation, replacement equations and the random walk.

For the sintering simulations in MercuryDPM, a short calculation time is highly prioritised. Although the semi-random walk shows an improvement by a factor of 1000, the replacement equations are again a factor 70 faster than the semi-random walk. Even if the semi-random walk would be improved to work well with a specific distance from the laser, a calculation time of 5 seconds per time step in the sintering simulations in MercuryDPM is too time-consuming. Although an advantage of a random walk is the fact that some variance in the absorption is present, which also occurs in the ray tracing simulations, a random walk is not suitable to use as a single step within the sintering simulations.

5 Conclusions

In this chapter, the results of this research are summarised and the research questions will be answered. The research question of this research is:

How can the laser beam absorption in powder-based sintering processes be modelled?

This research shows the proposal of a laser beam absorption model in powder-based beds. The model is based on a ray tracing model, where the laser beam is discretised into a finite number of rays. These rays interact with the spherical particles by reflecting and refracting, depending on the material's refraction index x, and are absorbed inside the particle depending on the material's attenuation coefficient μ.

2D simulations have been performed to determine the maximum energy dissipation threshold, the maximum spatial step size Δl and the minimum number of rays N_{ray}. The found maximum energy dissipation threshold was around 1% of the average starting energy of each ray, $I_{min} = 0.01/N_{ray}$. A maximum spatial step size of 10% of the particle diameter was shown to give consistent results. The number of light rays was found to be case specific and had to be determined for each simulation individually. Furthermore, a curvature approximation and total internal reflection have been taken into account during the simulations. For the 3D simulations, an equation is formulated to calculate the starting energy of each ray. Lastly, an equation is given to calculate the temperature increment per time step for each particle, based on its energy absorption.

Based on the presented model, the first sub-question of this research can be answered:

How can the absorption model be simplified for computational-friendly calculations?

Given the fact that the ray tracing simulations are too calculation intensive to be used in the sintering simulations in MercuryDPM, a simplification in the form of a set of equations has been proposed. This simplification consists of three parts.

Firstly, particle doublets have been simulated. These simulations mimicked an experiment by Hejmady, and the results were used to calibrate several variables necessary for the sintering simulations in MercuryDPM. Based on the distance between the particles, their energy absorption can be plotted for several particle diameters. A fitting polynomial function was found which is able to quickly calculate the absorption for any distance between the particles. A neck radius approximation, which is used in the sintering simulations in MercuryDPM, is also explained.

Secondly, equations for a powder bed have been constructed. This was done analytically for the particles in the top layer. A list of variables which affect the absorption has been proposed, after which a step-by-step explanation is given of the derivation of the equations which calculate the absorption. Next, the equations for the absorption in the rest of the bed were explained. After this, several variables were focused on to assure the equations are correct when these variables are changed. These were the volume fraction φ, the particle diameter D and the laser angle θ. The final set of equations was shown to correspond with the ray tracing simulations. A summary of the equations is given in Appendix H.

Lastly, the usage of a semi-random walk was investigated. Here, the rays propagating into a powder bed are replaced by rays performing a random walk in a bed with virtual particles. This method was shown to be much faster compared to the ray tracing simulations, but came with the disadvantage that the virtual particles only absorb one ray and therefore need to be added together per region to achieve a usable result. Furthermore, it is a factor 70 slower compared to the replacement equations.

If the laser absorption by the particles needs to be known during particle sintering simulations, the usage of a set of replacement equations has shown to be a computationally friendly method. The resulting amount of absorption has similar values compared to the ray tracing simulations, and has the advantage that calculations using different inputs can quickly be executed. However, if the absorption needs to be known for only a single time step and the duration of the simulation is unimportant, the ray tracing method results in a more accurate absorption as it takes into account the position of all particles relative to each other.

With the given model, the second sub-question of this research can be answered:

Which variables affect the laser beam absorption in powder-based sintering processes?

The final replacement equation has several variables as an input to determine the absorption for each particle. These are the propagated distance of the particle z, the particle distance to the laser centre d, the particle diameter D, the material's refraction index ratio x, the material's attenuation coefficient μ, the radius of the laser r_{laser}, and the angle of the laser θ.

An advantage of this model is that different materials can easily be used, since the inputs for the equations are shown to work if different values are used. Furthermore, if values of the sintering simulation change during the simulation itself, such as the laser power or the laser angle, the set of equations can still be used using these different inputs. It will simply give a different absorption or temperature change for the time steps after these input changes.

6 Recommendations

In this chapter, several recommendations are given for future research. In the introduction of this paper, several assumptions and limitations of this project were given. Each of these will be focused on, as future research which includes the effects which are excluded in this project, will provide more comprehensive knowledge and therefore a better understanding of the absorption of a laser beam by a polymer powder bed.

Firstly, this research focuses on the light absorption for a monodisperse particle bed. Although several particle sizes were simulated and their effects were measured, simulating a polydisperse bed might bring new insights into the effects of the particle size distribution on the energy absorption. One phenomenon observed in this research is the separation of visible layers of particles in monodisperse beds. A natural layer height of $\sqrt{6}/3$ of the particle diameter D was formed, which was subsequently used to determine the propagation depth z for each particle, depending on the layer it is in. The first layer experiences a propagation depth of $z = 0$, the second layer $z = D\sqrt{6}/3$, the third layer $z = 2D\sqrt{6}/3$, etc. For a polydisperse bed, the formation of distinct separate layers does not apply. Smaller particles will fill up the empty spaces created by bigger particles and the particle centres will not align on one layer. A new method of calculating the propagation depth z needs to be investigated.

At some point during this research, a particle bed with two different particle diameters was generated using the insertion and compression code in MercuryDPM. During this insertion and compression, the particles were able to move and rearrange themselves in the bed. A phenomenon which was observed during this is the segregation between the two sizes in the particle bed. Fig. 60 shows the top and bottom view of a particle bed with 2373 particles, from which 1183 have a diameter of $D = 72$ μm and 1190 a diameter of $D = 48$ μm, thus approximately an even amount for each size.
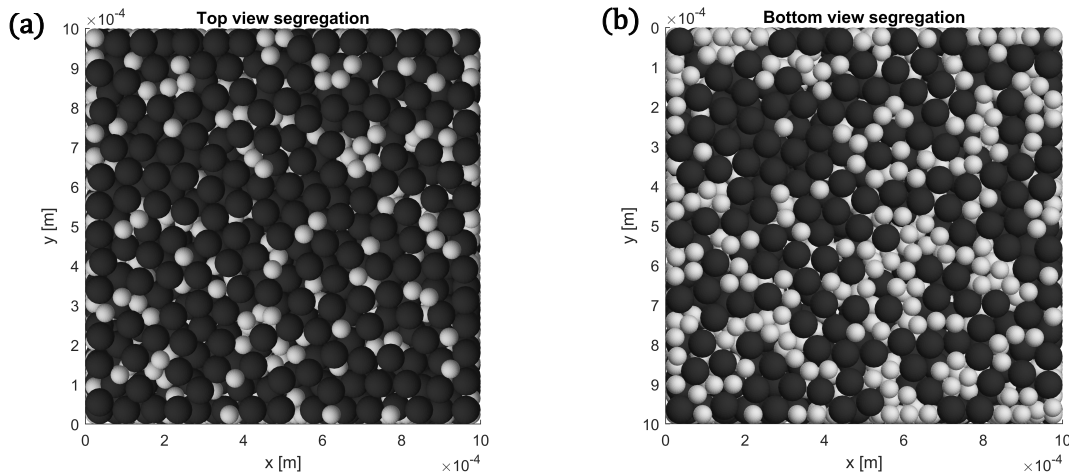

Fig. 60. A segregation of particle sizes can be observed from (a) the top of the bed with mainly big particles and (b) the bottom of the bed with mainly small particles.

This phenomenon can be explained by the fact that smaller particles can more easily fall between empty spaces which are created during the insertion and compaction movement. The big particles end up mainly occupying the top half of the particle bed. This could have an effect on the absorption at lower levels, as bigger particles might block more of the light hitting the top layer. The effect of this segregation on the light absorption needs to be investigated, as well as the comparison with the compaction of particles in real life. Meaning, whether this segregation phenomenon also occurs in actual 3D printing processes. This segregation might happen due to the fact that perfectly spherical particles are used.

The usage of spherical particles has been mentioned in the introduction. The reason only spherical particles are used is because of their predictable shape and easy calculation of light reflection and refraction. In real 3D printing processes, the sphericity of polymer particles depends on the used manufacturing process, which in general does not result in perfect spheres. Furthermore, a good distribution of the particles before sintering is affected by their shape, which is important for the final properties of the 3D printed part (Hejmady, 2021). How much the sphericity of the particles has an effect on the light propagation inside the bed, needs to be investigated.

Another assumption in this research is the energy distribution of the laser, which is assumed to be Gaussian. For this, the edges of the laser are cut off, which causes there to be no rays outside of the laser area. This is also visible from the absorption based on the ray tracing simulations. However, at lower layers, this cut-off at the edge of the laser is faded out. Fig. 61 shows how the analytical solution follows the ray tracing simulation correctly for layer 1, but less well for layer 2. A purple line in figure (b) shows a better approximation.
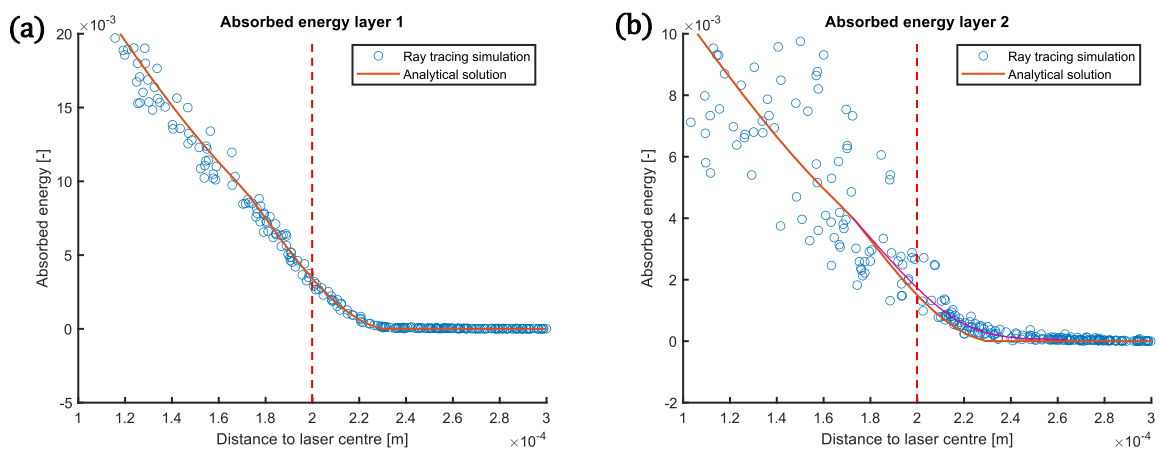

Fig. 61. Analytical solution showing a change in absorbed energy around the edge of the laser in (a) layer 1, where the line follows the ray tracing results well, and (b) layer 2, where this effect is less. The red dashed line indicates the edge of the laser, the purple line shows a better approximation of the absorption.

Since the absorption in a lower layer is based on the absorption in the top layer, which correctly uses this change in absorption at the edge of the laser, all lower layers have this same shape. A reformulation of the equation calculating the absorption in the lower layers would need to be done to correct this problem.

Furthermore, many simulations have been conducted to test the validity of the equations when changing variables such as the particle size, attenuation coefficient, laser radius, volume fraction, etc. The final equation shows to be correct while changing all variables. However, more combinations of different variables could be tested. For example, changing both the volume fraction and the incoming laser angle might have an unexpected outcome on the path of the light rays. Further simulations are necessary to determine these effects.

Lastly, the equations are formulated in such a way that they correspond to the ray tracing simulations. However, more physical experiments are necessary to further validate the equations. While the experiments conducted by Hejmady are compared to the sintering simulations in MercuryDPM, experiments specifically meant to measure the light path and absorption in polymer powder beds will help with the validity of the equations presented in this paper.

References

Alvarez, J. E., Snijder, H., Vaneker, T., Cheng, H., Luding, S., & Weinhart, T. (2021). *Neck growth kinetics during polymer sintering for powder-based processes*. *05001*, 0–3.

Bibas, C. (2020). *Traditional SLS/SLM 3D printing errors*. https://tecnica.com/traditional-sls-slm-3d-printing-errors/

Bierwisch, C., Mohseni-Mofidi, S., Dietemann, B., Kraft, T., Rudloff, J., & Lang, M. (2020). Particle-based simulation, dimensional analysis and experimental validation of laser absorption and thermo-viscous flow during sintering of polymers. *Procedia CIRP*, *94*, 74–79. https://doi.org/10.1016/j.procir.2020.09.015

Brighenti, R., Cosma, M. P., Marsavina, L., Spagnoli, A., & Terzano, M. (2021). Laser-based additively manufactured polymers: a review on processes and mechanical models. *Journal of Materials Science*, *56*(2), 961–998. https://doi.org/10.1007/s10853-020-05254-6

Hejmady, P. (2021). *Selective laser sintering of polymer particles studied by in-situ visualization*. https://research.tue.nl/en/publications/selective-laser-sintering-of-polymer-particles-studied-by-in-situ

Hejmady, P., Van Breemen, L. C. A., Anderson, P. D., & Cardinaels, R. (2019). Laser sintering of polymer particle pairs studied by in situ visualization. *Soft Matter*, *15*(6), 1373–1387. https://doi.org/10.1039/c8sm02081g

Hejmady, P., van Breemen, L. C. A., Hermida-Merino, D., Anderson, P. D., & Cardinaels, R. (2022). Laser sintering of PA12 particles studied by in-situ optical, thermal and X-ray characterization. *Additive Manufacturing*, *52*, 102624. https://doi.org/10.1016/j.addma.2022.102624

Kokhanovsky, A. A. (2015). Light Scattering Reviews 10: Light Scattering and Radiative Transfer. In *Light Scattering Reviews 10: Light Scattering and Radiative Transfer*. https://doi.org/10.1007/978-3-662-46762-6

Liu, X. (2017). *Numerical modeling and simulation of selective laser sintering in polymer powder bed*. 1–138. https://tel.archives-ouvertes.fr/tel-01920677

Osmanlic, F., Wudy, K., Laumer, T., Schmidt, M., Drummer, D., & Körner, C. (2018). Modeling of laser beam absorption in a polymer powder bed. *Polymers*, *10*(7), 784. https://doi.org/10.3390/polym10070784

Polymerdatabase. (n.d.). *Nylon 12*. Retrieved May 12, 2022, from http://polymerdatabase.com/polymers/nylon12.html

Sagar, M. B., & Elangovan, K. (2017). Consolidation & factors influencing sintering process in polymer powder based additive manufacturing. *IOP Conference Series: Materials Science and Engineering*, *225*(1), 012075. https://doi.org/10.1088/1757-899X/225/1/012075

Sultanova, N., Kasarova, S., & Nikolov, I. (2009). Dispersion properties of optical polymers. *Acta Physica Polonica A*, *116*(4), 585–587. https://doi.org/10.12693/APhysPolA.116.585

Weinhart, Orefice, Post, van Schrojenstein Lantman, Denissen, Tunuguntla, Tsang, Cheng, Shaheen, Shi, Rapino, Grannonio, Losacco, Barbosa, Jing, Alvarez Naranjo, Roy, den Otter, & Thornton. (2019). *Fast, flexible particle simulations — An introduction to MercuryDPM* (No. 107129). Computer Physics Communications.

Yaagoubi, H., Abouchadi, H., & Taha Janan, M. (2021). Simulation of the Heat Laser of the Selective Laser Sintering Process of the Polyamide12. *E3S Web of Conferences*, *297*, 01050. https://doi.org/10.1051/e3sconf/202129701050

Yi-Ting, T., & Johnson, S. (2016). *Ray Optics*. https://doi.org/10.1007/978-3-662-21561-6_1
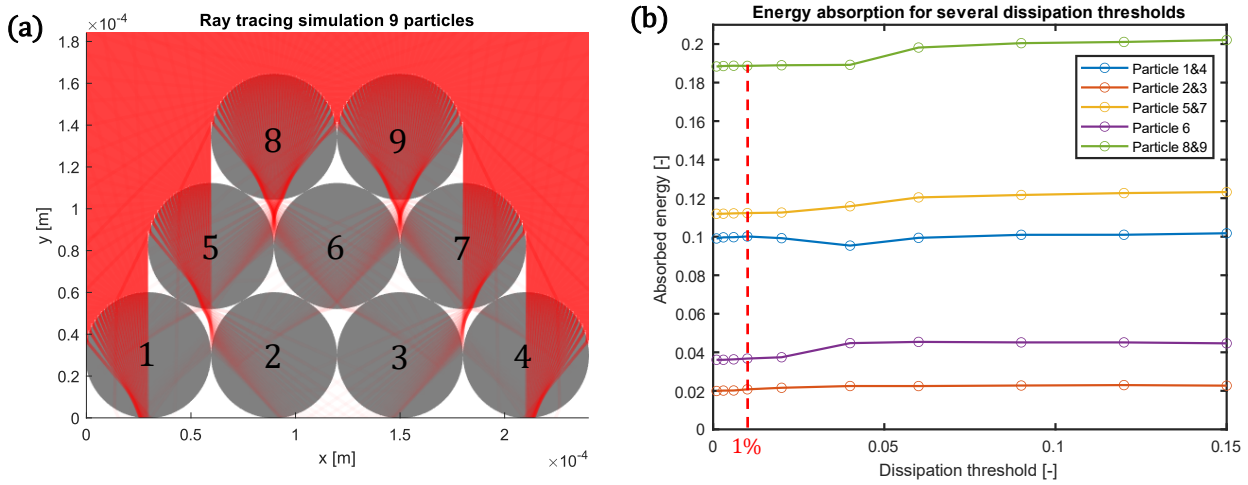
Appendices

Appendix A

Fig. 62. (a) 2D simulation results of light rays propagating into nine particles numbered 1 till 9. (b) Resulting absorbed energy per particle group out of the total incoming energy, plotted for several different dissipation thresholds.
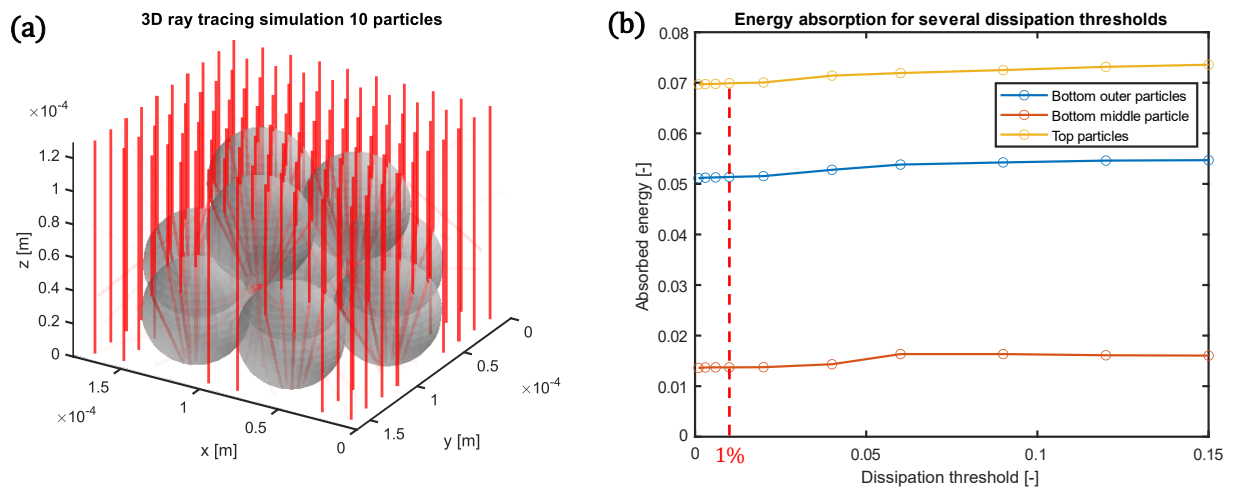
Appendix B

Fig. 63. (a) 3D simulation results of light rays propagating into 10 particles. Due to symmetry, these are grouped as the six outer bottom particles, the one bottom middle particle, and the three top particles. (b) Resulting absorbed energy per particle group out of the total incoming energy, plotted for several different dissipation thresholds.
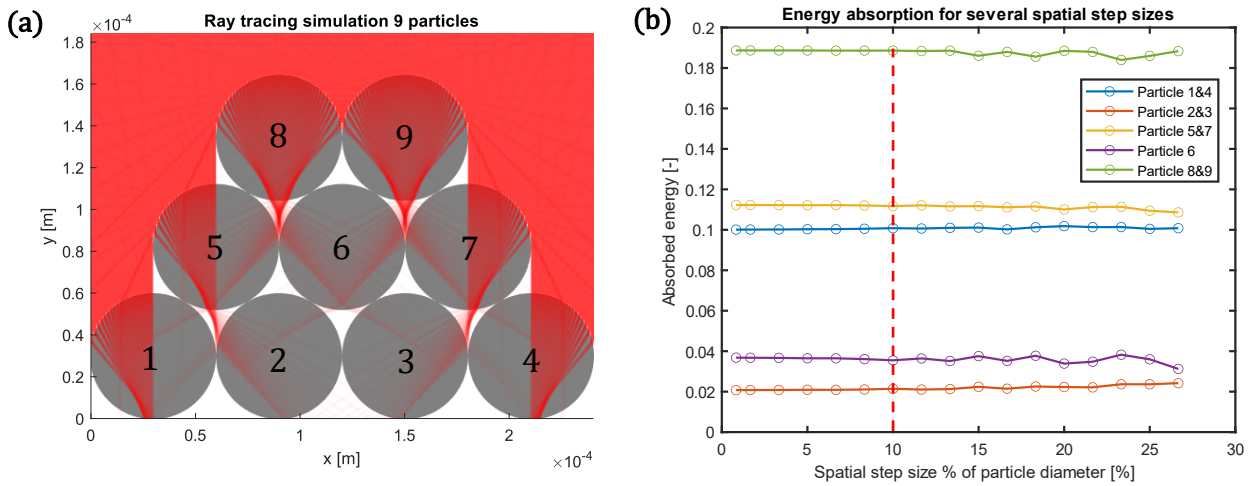
Appendix C

Fig. 64. (a) 2D simulation results of light rays propagating into nine particles numbered 1 till 9. (b) Resulting absorbed energy per particle group out of total incoming energy, plotted for several different spatial step sizes.
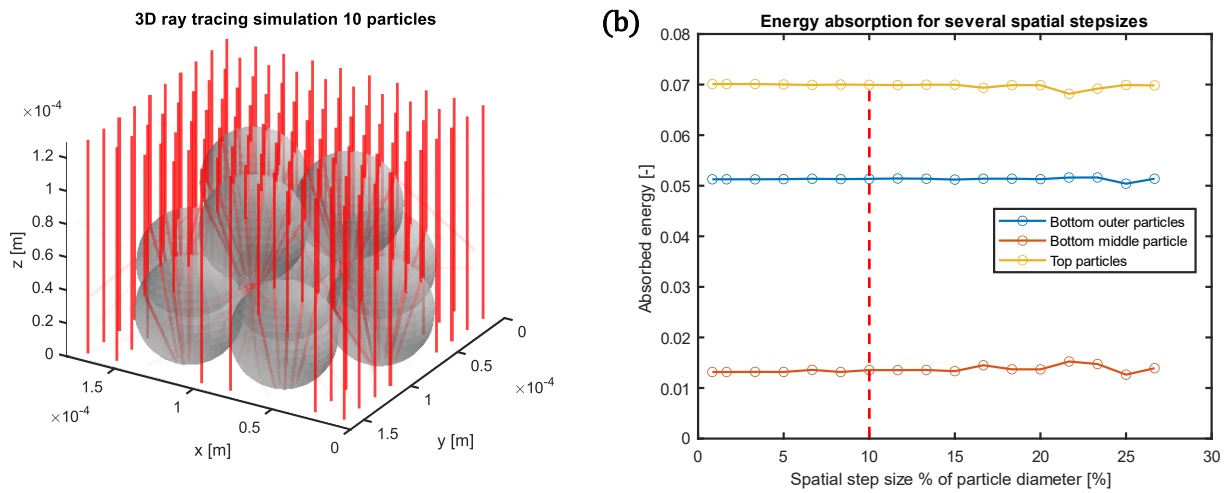
Appendix D

Fig. 65. (a) 3D simulation results of light rays propagating into 10 particles. Due to symmetry, these are grouped as the six outer bottom particles, the one bottom middle particle, and the three top particles. (b) Resulting absorbed energy per particle group out of total incoming energy, plotted for several different spatial step sizes.
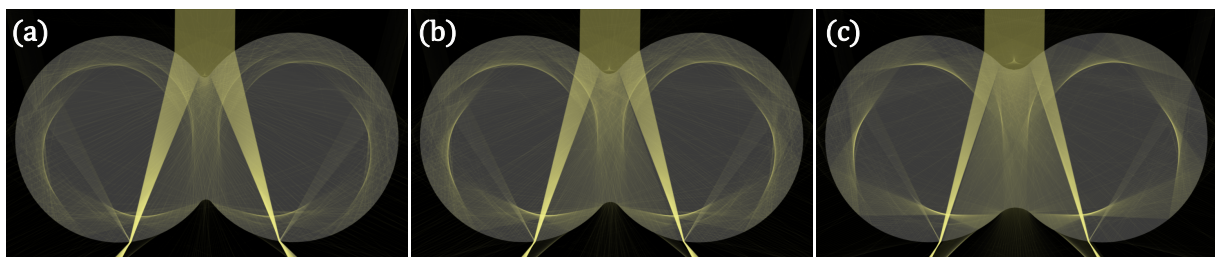
Appendix E

Fig. 66. Ray Optics Simulation of two particles with (a) a small, (b) a medium-sized and (c) a large curvature, showing no significant difference in the path of the rays.

Appendix F

Here, the equation for the diameter increase caused by overlapping spheres is derived.

Consider two circles with equal diameter D and a distance between their centres d. One particle has its centre at $(D/2 - d, 0)$ and the other at $(D/2, 0)$:
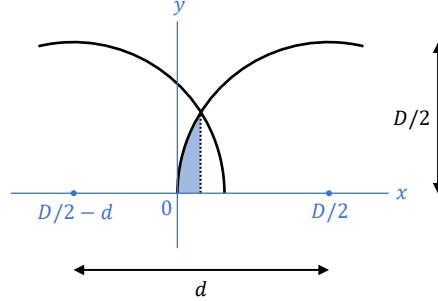

Fig. 67. Two overlapping circles with an equal diameter D with a distance d between their centres, located at $(D/2 - d, 0)$ and $(D/2, 0)$.

The overlap between the circles has a distance of $D - d$. Consider the shaded region from 0 to $\frac{D-d}{2}$ between the x axis and the right circle. The equation of the top half of the right circle is:

$$y = \sqrt{\left(\frac{D}{2}\right)^2 - \left(x - \frac{D}{2}\right)^2}$$

A spherical cap can be created by revolving the shaded region around the x axis. The spherical cap has the following volume V:

$$V = \pi \int_0^{\frac{D-d}{2}} y^2 \, dx = \pi \int_0^{\frac{D-d}{2}} \left(\left(\frac{D}{2}\right)^2 - \left(x - \frac{D}{2}\right)^2\right) dx = \pi \int_0^{\frac{D-d}{2}} \left(\frac{D^2}{4} - x^2 + Dx - \frac{D^2}{4}\right) dx$$

$$= \pi \int_0^{\frac{D-d}{2}} (Dx - x^2) \, dx = \pi \left[\frac{1}{2}Dx^2 - \frac{1}{3}x^2\right]_0^{\frac{D-d}{2}} = \pi \left(\frac{1}{2}D\left(\frac{D-d}{2}\right)^2 - \frac{1}{3}\left(\frac{D-d}{2}\right)^3\right)$$

$$= \pi \left(\frac{1}{8}D(D^2 - 2dD + d^2) - \frac{1}{24}(D^3 - 3dD^2 + 3d^2D - d^3)\right)$$

$$= \pi \left(\frac{1}{8}D^3 - \frac{1}{4}dD^2 + \frac{1}{8}d^2D - \frac{1}{24}D^3 + \frac{1}{8}dD^2 - \frac{1}{8}d^2D + \frac{1}{24}d^3\right)$$

$$= \pi \left(\frac{1}{12}D^3 - \frac{1}{8}dD^2 + \frac{1}{24}d^3\right)$$

The volume of the overlap of the two spheres is twice this volume:

$$V_{overlap} = \pi \left(\frac{1}{6}D^3 - \frac{1}{4}dD^2 + \frac{1}{12}d^3\right)$$

To preserve the volume of the spheres when they are overlapping, their diameter needs to increase. This new diameter is called D_2. Therefore, the volume of the two spheres before overlap needs to be equal to the volume of two spheres with the increased diameter D_2 minus their overlapping volume.

$$2 \cdot \frac{\pi}{6}D^3 = 2 \cdot \frac{\pi}{6}D_2^3 - \pi\left(\frac{1}{6}D_2^3 - \frac{1}{4}dD_2^2 + \frac{1}{12}d^3\right) = \pi\left(\frac{1}{6}D_2^3 + \frac{1}{4}dD_2^2 - \frac{1}{12}d^3\right)$$

$$\frac{1}{3}D^3 - \frac{1}{6}D_2^3 - \frac{1}{4}dD_2^2 + \frac{1}{12}d^3 = 0$$

$$2D_2^3 + 3dD_2^2 - d^3 - 4D^3 = 0$$

Divide both sides by D^3 and let $A = \frac{d}{D}$ and $B = \frac{D_2}{D}$:

$$2\left(\frac{D_2}{D}\right)^3 + 3\frac{dD_2^2}{D^3} - \left(\frac{d}{D}\right)^3 - 4 = 2\left(\frac{D_2}{D}\right)^3 + 3\frac{d}{D}\left(\frac{D_2}{D}\right)^2 - \left(\frac{d}{D}\right)^3 - 4 = 0$$

$$2B^3 + 3AB^2 - A^3 - 4 = 0$$

This equation needs to be solved for B, which is the factor by which the diameter of the spheres will increase during overlap. If $d = 0$ (full coalescence) then $A = 0$ and $2B^3 = 4$, making $B = \sqrt[3]{2}$. If $d = D$ (touching spheres) then $A = 1$ then $2B^3 + 3B^3 = 5$, making $B = 1$. For any value of $0 < d < D$, an equation for B needs to be known.

Let $p = B + \frac{A}{2}$ and substitute for B:

$$2\left(p - \frac{A}{2}\right)^3 + 3A\left(p - \frac{A}{2}\right)^2 - A^3 - 4 = 0$$

$$2\left(p^3 - 3p^2\frac{A}{2} + 3p\frac{A^2}{4} - \frac{A^3}{8}\right) + 3A\left(p^2 - pA + \frac{A^2}{4}\right) - A^3 - 4 = 0$$

$$2p^3 - 3p^2\!\!\!\diagup\!\!\!A + \frac{3}{2}pA^2 - \frac{A^3}{4} + 3p^2\!\!\!\diagup\!\!\!A - 3pA^2 + \frac{3}{4}A^3 - A^3 - 4 = 0$$

$$2p^3 - \frac{3}{2}pA^2 - \frac{1}{2}A^3 - 4 = 0$$

$$p^3 - \frac{3}{4}pA^2 - \frac{1}{4}A^3 - 2 = 0$$

Let $p = q + \frac{r}{q}$ where r will be determined later:

$$\left(q + \frac{r}{q}\right)^3 - \frac{3}{4}A^2\left(q + \frac{r}{q}\right) - \frac{1}{4}A^3 - 2 = 0$$

$$q^3 + 3qr + 3\frac{r^2}{q} + \frac{r^3}{q^3} - \frac{3}{4}A^2q - \frac{3}{4}A^2\frac{r}{q} - \frac{1}{4}A^3 - 2 = 0$$

Multiply both sides by q^3 and collect the terms with q:

$$q^6 + 3q^4r + 3q^2r^2 + r^3 - \frac{3}{4}A^2q^4 - \frac{3}{4}A^2q^2r - \frac{1}{4}A^3q^3 - 2q^3 = 0$$

$$q^6 + q^4\left(3r - \frac{3}{4}A^3\right) + q^3\left(-\frac{1}{4}A^3 - 2\right) + q^2\left(3r^2 - \frac{3}{4}A^2r\right) + r^3 = 0$$

Now a value for r will be chosen, in such a way that the second and fourth term will become zero. This can be done if $r = \frac{A^2}{4}$:

$$q^6 + q^4\left(3\frac{\diagup\!\!\!A^2}{4} - \frac{3}{4}\diagup\!\!\!A^3\right) + q^3\left(-\frac{1}{4}A^3 - 2\right) + q^2\left(3\frac{\diagup\!\!\!A^4}{16} - \frac{3}{4}\diagup\!\!\!A^2\frac{\diagup\!\!\!A^2}{4}\right) + \frac{A^6}{64} = 0$$

$$q^6 + q^3\left(-\frac{1}{4}A^3 - 2\right) + r^3 = 0$$

Let $s = q^3$ and substitute for q:

$$s^2 + s\left(-\frac{1}{4}A^3 - 2\right) + \frac{A^6}{64} = 0$$

Solve using the quadratic formula. Since all used variables are distances, consider only the positive solution:

$$s = \frac{\frac{1}{4}A^3 + 2 + \sqrt{\frac{1}{16}A^6 + A^3 + 4 - \frac{A^6}{16}}}{2} = \frac{A^3 + 8 + 4\sqrt{A^2 + 4}}{8}$$

Substitute back for $s = q^3$ and solve for q, again consider only the positive solution:

$$q = \sqrt[3]{\frac{A^3 + 8 + 4\sqrt{A^2 + 4}}{8}} = \frac{1}{2}\sqrt[3]{A^3 + 8 + 4\sqrt{A^2 + 4}}$$

Let $C = \sqrt[3]{A^3 + 8 + 4\sqrt{A^2 + 4}}$, which gives $q = \frac{1}{2}C$. Substitute back for $p = q + \frac{r}{q}$ and with $r = \frac{A^2}{4}$:

$$p = \frac{1}{2}C + \frac{A^2/4}{C/2} = \frac{1}{2}C + \frac{A^2}{2C}$$

Substitute back for $p = B + \frac{A}{2}$ and solve for B:

$$B + \frac{A}{2} = \frac{1}{2}C + \frac{A^2}{2C}$$

$$B = \frac{1}{2}\left(C + \frac{A^2}{C} - A\right)$$

The equation is now solved. The new diameter D_2 can be calculated by multiplying the original diameter D by the factor B:

$$D_2 = \frac{D}{2}\left(C + \frac{A^2}{C} - A\right)$$

with

$$C = \sqrt[3]{A^3 + 8 + 4\sqrt{A^2 + 4}}$$

and

$$A = \frac{d}{D}$$

Or, fully written out:

$$D_2(d, D) = \frac{D}{2}\left(\sqrt[3]{\frac{d^3}{D^3} + 8 + 4\sqrt{\frac{d^2}{D^2} + 4}} + \frac{\frac{d^2}{D^2}}{\sqrt[3]{\frac{d^3}{D^3} + 8 + 4\sqrt{\frac{d^2}{D^2} + 4}}} - \frac{d}{D}\right)$$

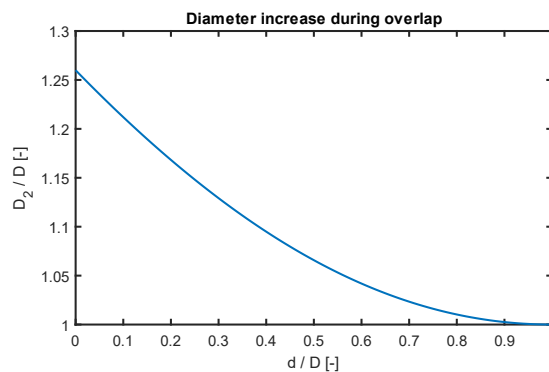This equation has the following curve, which shows that $B = \sqrt[3]{2}$ for $d = 0$ and $B = 1$ for $d = 1$:

Fig. 68. Diameter increase during overlap, showing the growth factor D_2/D as a function of d/D.
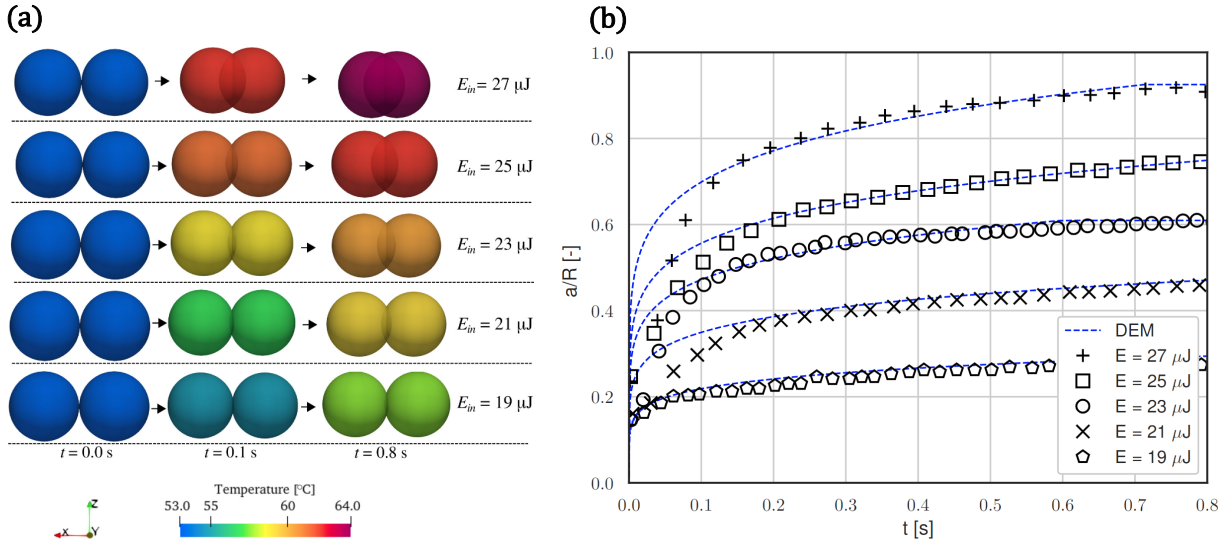
Appendix G

Fig. 69. (a) Sintering PS doublets showing the temperature evolution for several laser pulse energies from the first contact at $t = 0$ s to $t = 0.8$ s, visualised by the colour change, simulated in MercuryDPM. (b) Neck-growth kinetics showing the dimensionless neck radius a/R of PS doublets for several laser pulse energies from the sintering simulation, compared to the experimental data by Hejmady (blue dashed line).

Appendix H

Here, a summary is given of the final analytical model.

The relative amount of energy a particle in the top layer receives out of the total laser energy (E_{in}):

$$E_{in}(d, D, r_{laser}) \approx \frac{b-a}{n} \sum_{i=1}^{n-1} E_{in}' \left(a \cdot \left(1 - \frac{i}{n}\right) + b \cdot \frac{i}{n} \right)$$

with

$$E_{in}'(d_s) = \frac{4d_s}{\pi r_{laser}^2 (1 - e^{-2})} e^{\frac{-2d_s^2}{r_{laser}^2}} \cdot \text{real}\left(\cos^{-1}\left(\frac{d_s^2 + d^2 - (D/2)^2}{2 \cdot d_s \cdot d} \right) \right)$$

$$a = \max\left(d - \frac{D}{2}, \ 0 \right)$$

$$b = \min(d + D/2, r_{laser})$$

$$n = 1000$$

$$d = \frac{|(\bar{c} - \overline{p_p}) \times \vec{k}_0|}{|\vec{k}_0|}$$

The relative amount of energy a particle in the top layer absorbs out of the total energy hitting that particle (E_p):

$$E_p(x, \mu, D) \approx \frac{1}{n} \sum_{i=1}^{n-1} E_p' \left(\frac{i}{n} \right)$$

66

with

$$E_p{'}(r) = \frac{2r}{\dfrac{1}{1-R(r)} - \dfrac{1}{1-e^{\mu D\sqrt{1-x^2r^2}}}}$$

$$R(r) = \frac{1}{2}\left(\left(\frac{x\sqrt{1-r^2}-\sqrt{1-x^2r^2}}{x\sqrt{1-r^2}+\sqrt{1-x^2r^2}}\right)^2 + \left(\frac{\sqrt{1-r^2}-x\sqrt{1-x^2r^2}}{\sqrt{1-r^2}+x\sqrt{1-x^2r^2}}\right)^2\right)$$

$$n = 500$$

The relative amount of energy a particle in the top layer absorbs out of the total laser energy (E_{abs}):

$$E_{abs}(d, D, r_{laser}, x, \mu) = K_{cor} \cdot E_{in}(d, D, r_{laser}) \cdot E_p(x, \mu, D)$$

with

$$K_{cor} = 1.09937$$

The propagation depth of a particle in the bed (z):

$$z = \left((i-1) \cdot D \cdot \sqrt{6}/3\right)/\cos\theta$$

with i the layer number a particle is in:

$$i = \texttt{ceil}\left(\left(Z - (\overline{p_p})_3 - \frac{Z - N_{layer} \cdot D \cdot \sqrt{6}/3}{2}\right)/(D \cdot \sqrt{6}/3)\right)$$

$$Z = \left(N_{layer} - 1\right) \cdot D \cdot \sqrt{6}/3 + D$$

The relative amount of energy a particle absorbs out of the total laser energy:

$$E(d, D, r_{laser}, x, \mu, \theta, N_{layer}) = E_{abs} \cdot e^{(-0.036-0.45(\mu D)^{-0.48})(\mu z)^{1.4}-3.8(\mu z)^{0.3}\cdot(\varphi-0.574)^{0.8}}$$

The temperature evolution of the particles as an effect of the laser absorption:

$$\Delta T = \frac{P_{in} \cdot E \cdot \Delta t}{m \cdot c_p}$$